UNIVERSITEIT GENT

FACULTY OF SCIENCES

Study of the Microelectrochemical Corrosion of 304L and 316L Stainless Steels and Unalloyed Copper in the Presence of Chloride ions: Comparison with Conventional Large Scale Electrochemical Techniques

Thesis submitted in fulfillment of the requirements for the degree of

Doctor of Science: Chemistry

by

FARZIN ARJMAND

Promoter: Prof. Dr. Annemie Adriaens

27th June, 2013

Ghent – Belgium

esa Electrochemistry and Surface Analysis

Acknowledgements

Since 2009 I have had the pleasure to work in a friendly atmosphere with a group of nice colleagues in the lovely city Gent.

From the academic point of view, doing a PhD thesis is not something you manage on your own. Therefore, here I need to acknowledge some people who were effective on successful ending of this work.

In the first place, I would like to thank my promoter Professor Annemie Adriaens for giving me the opportunity to work as a PhD student in her group and for all her helps during my PhD work.

I also would like to thank people of the Department of Analytical Chemistry especially the present members of ESA group: Pieter–Jan Sabbe, Sara Zandi, Alice Elia, Michel De Keersmaecker, Elbeshary Ahmed, Victoria Flexer and Rosie Grayburn.

Moreover, UGent (BOF) is especially acknowledged for funding this PhD research.

In addition, especial words of thanks go to Professor Herman Terryn (VUB) for all his highly useful advices.

Also would like to thank:

Sylvia Lycke (UGent) and Philip Brondeel (UGent).

Jan Garrevoet (UGent) for the time–laps video.

Professor Kim Verbeken (UGent) for Figure 4.14 and especially for providing the steel samples and also for the SEM–EDS measurements.

Journal of Electrochimica Acta for providing the permission of Figure 1.2.

Finally, gratitude goes to Dr. Nico De Roo (UGent) for the XPS analyses, Professor Christophe Detavernier (UGent), Dr. Sandra Van Vlierberghe (UGent) and Wouter Devulder (UGent) for the AFM measurements.

And last but not least, I would like to thank my parents, my brothers and all my friends in Iran who supported and encouraged me during my stay in Belgium.

List of contents

2.3.2. Pit nucleation……………………………………………………..37

2.3.3. Aqueous corrosion of stainless steel………………….….….……40

2.3.4. Aqueous corrosion of copper……………………….….……..47

2.3.4.1. General corrosion…………………………………..……48

2.3.4.2. Electrodissolution………………………….….…..…………49

Bibliography…………………………………………………………….52

3. Comparative investigation of 304L stainless steel using a microcapillary cell and a conventional setup..……………………………………...57

3.1. Introduction…………………………………………………………...57

3.2. Experimental……………………………………………………………58

3.2.1. Specimens and surface preparation……………………………58

3.2.2. Electrochemical setups……………………………………….....58

3.3. Results and discussion……………………………………………..…59

3.3.1. Comparison of localized and conventional electrochemical measurements……………………………………………………59

3.4. Conclusions……………………………………………………………...65

Bibliography…………………………………………………………….67

4. Cathodic polarization of 304L and 316L stainless steels in NaCl solution………………...…………………………………………….…..68

4.1. Cathodic polarization of 316L stainless steel large scale disc electrode under static and dynamic conditions…………………………………68

4.1.1. Introduction…………………………………………………………68

4.1.2. Experimental………………………………………………………...72

4.1.2.1. Specimens and surface preparation………………………..72

4.1.2.2. Cell design and electrochemical measurements………72

4.1.2.3. Scanning electron and atomic force microscopy………73

4.1.3. Results and discussion…………………………………………74

4.1.3.1.Flow motion and produced flow regime..………….……74

4.1.3.2.Potentiodynamic polarization under static and flow conditions ……..……………………….…………..............74

4.1.3.3. Effect of flow velocity on the pit nucleation……………77

4.1.3.4.Effect of flow velocity on the cathodically polarized steel…………...……………….……………...…….……...77

Chapter 1

Introduction

Microcapillary electrochemical droplet cell: applications in solid state electrochemical surface analysis

1.1. The history of microcapillaries

In principle, every metallic, glass, or plastic tube with a diameter of less than 1000 μm can be called a capillary. Metallic capillaries, followed shortly after by glass capillaries, were first commercially made for use in chromatography. Before 1958, only homemade capillaries existed, and they were used for only a limited range of special work in science. The first generations of commercial capillary columns were made from copper, cupro–nickel, and (first in 1957) from Nylon. In the same year, Desty [1] invented a technique that could produce long lengths of small–diameter soft glass tubing in the form of a coil. He also invented a device that very slowly fed a section of wide, relatively thick–walled soft glass into a furnace using appropriate rollers. The glass was fed through a bent stainless steel tube, and the capillary tube formed in this way was rigid when cold. At the time, these tubes were considered as an ideal tool for gas chromatography. Later, well–prepared glass capillaries with extremely small diameters were used in different fields of science such as biochemistry/biology [2], neuroscience [3], analytical chemistry [4–8], and recently, electrochemistry [9, 10].

In the case of electrochemistry and electrochemical surface analysis of solids, there has always been a desire to create miniaturized working electrodes for use in the electrochemical microanalysis, micro–preparation, and localized control of surface reactions.

The mask technique, using photoresist, was one of the first techniques reported for miniaturization of the exposed area [11, 12]. In this technique, the photoresist covers the electro–active surface. After a small bare area is made by removing the protecting photoresist layer, the bare point is filled by the electrolyte. Finally, the counter and reference microelectrodes are attached to the electrolyte droplet. Some researchers have prepared microelectrodes immersed in the electrolyte by reducing the size of the solid surface. This process creates microsurfaces either by covering the majority of the

electro–active surface, or using thin wires as microelectrodes. Such thin metal wires are typically embedded using a glass or plastic cover [13, 14]. However, well–defined microelectrodes cannot be prepared easily from all electro–active materials; for example, powders that are used in batteries or other single crystals cannot be used to prepare microelectrodes.

As an alternative, in the mid–1990s, Suter (and in parallel, Lohrengel) proposed the use of a new design of microcell called a microcapillary cell, in which various sizes of solids can be measured without need to reduce the size of the surface before measurement. This setup is based on the use of glass microcapillaries, and uses a typical three–electrode electrochemical system with some changes in the form and position of the cell and the electrodes [9, 15–17].

Reading recently published research articles in solid–state electrochemistry, it is apparent that the use of the microcapillary technique in microanalysis of solids, and especially in corrosion studies, has increased since the first use of this technique in 1990s. In fact, almost 30% of the total number of studies on electrochemical surface analysis using microcapillary cells was published during 2011–2012.

1.2. The microcapillary cell setup

The microcell setups used by different research groups typically follow the setup reported by Böhni and Suter in 1995 [9]. This three–electrode setup consists of a microcapillary with a maximum tip diameter of 1000 μm, which is filled with electrolyte that touches a small area of the solid surface and forms the working electrode. The counter electrode is a stable metal wire (usually platinum or gold) that is typically located close to the tip of the microcapillary. Different types of reference electrodes with different sizes, and in different positions depending on the shape of the microcell and its holder, are used. The microcapillary cell is typically mounted on an optical microscope. Due to the small size of the microcapillaries used in some cases, an ocular or camera is also attached close to the measurement area to follow the positioning of the microcapillary tip relative to the surface of the specimen, and to monitor the measurement procedure (Figure 1.1). This setup has been used by several researchers, be it with some modifications [18–38].

Microcell setups that are mounted on a microscope typically have reference electrodes that are located outside the cell. One of the technical disadvantages of this design is possible blockage of the tube between the cell body and the reference electrode with air bubbles. The setup used by Lohrengel et al. [15, 16, 28, 31, 35, 38] solved this problem by using a mini reference electrode inside the acryl glass carrier, as shown in

Figure 1.1. This setup also makes it possible to locate the counter electrode wire (Pt/Au) inside the microcapillary next to the tip, resulting in reduced cell resistance due to the small distance between the working and counter electrodes [28, 29].

Some attempts also have been performed to improve the positioning of the microcapillary on the measured solid sample. The microcapillary setups used by Lohrengel [28, 35] and Schneider [21], for example, are equipped with a force sensor machine that monitors the contact between the microcapillary tip and the solid surface. This machine enables computer controlled surface mapping. Suter and Böhni [39], on the other hand, have assembled a non–contact scanning capillary microscope, which is a combination of scanning probe technology with an electrochemical system equipped with a piezoelectric sensor to monitor the positioning of the microcapillary tip.

In some cases, the microcapillary cell is coupled with spectrophotometric analytical techniques. Suter and Böhni [30] reported the use of a nanocapillary electrochemical scanning probe microscope, which is a combination of a nanocapillary cell and a 650 nm laser beam that lies parallel to the solid surface and passes through the glass nanocapillary. The glass nanocapillaries used in this microscope have the smallest tip diameter reported in the literature (inner diameter: 150 nm). This setup has been used to deposit copper spots on various substrates, including gold and n–type Si semi–conductor surfaces at low acidic pHs.

.

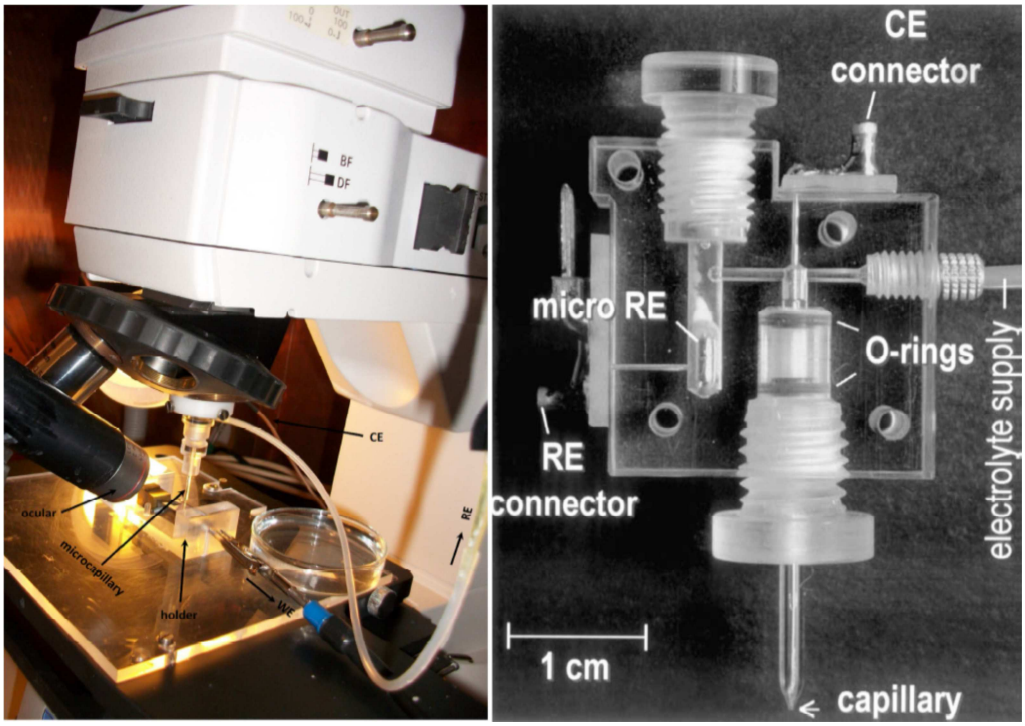

Figure 1.1. *Photographs of microcapillary cell setups: (left) mounted on an optical microscope used by Buytaert et al. taken at the Netherlands Institute for Metals Research (NIMR), Delft University of Technology, Delft, The Netherlands, with kind permission from Prof. H. Terryn. (right) without microscope, with inlet and outlet tubes [35] (with permission from Elsevier).*

1.3. Procedure for the fabrication of microcapillaries

There are two procedures that are most frequently used for the fabrication of glass microcapillaries. The first technique uses a puller machine to produce well–defined microcapillaries with various tip diameters. The use of the puller machine to make glass microcapillaries makes the procedure very fast and easy. Moreover, one can control the exact inner tip diameter of the produced microcapillaries. This technique can be used to make capillaries with nanometer–scale inner tip diameters. However, as handling of the thinnest specimens is extremely difficult, diameters from 10 to 500 μm are typically used [31]. The disadvantage of this method is its high cost. There are several companies worldwide that produce different types of glass, plastic, and metal capillary tubes.

We have reported the use of homemade glass microcapillaries, providing a cheap alternative method [29]. Here, the microcapillaries are obtained by heating thin glass tubes until the glass melting point is reached, followed by pulling them in a specific manner. The tip surface of the prepared microcapillaries is polished, using first 600 and then 1200 grit silicon carbide (SiC) paper. In this way, minimum inner tip

diameters of approximately 70–100 µm can be obtained. Smaller diameters cannot be achieved using this method.

It is generally necessary to prevent leakage of the electrolyte from the tip of the microcapillary where it touches the surface of the specimen. Typically, a flexible silicone glue gasket is attached to the mouth of the microcapillary by dipping its tip in a liquid silicone glue. By repeating this procedure two or three times, thin layers of silicone can be applied onto the tip of the capillaries. The mouth of the microcapillary then needs to be opened without destroying the gasket. This is performed either by pressing a stream of ethanol through the microcapillary using a micro syringe after applying the silicone glue, or by flushing a continuous stream of an inert gas through the tip during attachment of the gasket. The latter method results in gaskets of higher quality. Figure 1.2 shows a homemade microcapillary with a silicone glue gasket made using a nitrogen stream [29]. Depending on the type of the surface analysis to be performed, the sealed microcapillary can be attached to the solid surface before drying for a single measurement, or can be used for multiple measurements (such as surface scanning) after drying [29–31]. Suter and Böhni [34] investigated the quality of the silicone gaskets used in microcapillary techniques, revealing that the hydrophobic properties and deformability of the silicone are critical factors. The hydrophobic properties of the glue prevent the electrolyte from penetrating under the glue gasket, thereby avoiding crevice corrosion under the gasket. Moreover, the high deformability of the silicone gasket makes it possible to perform measurements even on rough surfaces.

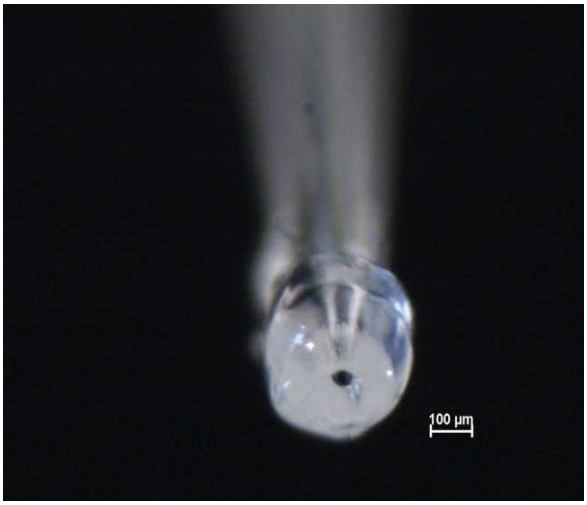

Figure 1.2. *Optical image of a microcapillary with a silicone glue gasket.*

In addition to standard silicone glue gasket microcapillaries (Figure 1.2), there are other designs for capillary–based working electrodes. One of the more advanced techniques is to make the working microelectrode using a free droplet held under the microcapillary tip by its surface tension. In this technique, which is called also scanning droplet technique, the microcapillary is made from glass or plastic, or a stable metal such as platinum or gold; in the latter case, the capillary itself forms the counter electrode [15, 31, 35]. Figure 1.3 shows a schematic drawing of a metal microcapillary without a silicone glue gasket, which is attached to a solid surface by a free droplet. In this figure, the capillary body forms the counter electrode. This design requires small volumes of electrolyte, because the pressure of the bulk electrolyte above the droplet can cause leakage of the electrolyte under the microcapillary. Modified microcapillary designs that allow the evaluation of additional factors during measurement have been suggested by some authors. Metal–metallized, coaxial, double channel flow, light–containing microcapillaries, and microcapillaries with stress or friction, or combined with a pH meter and temperature controller, are all examples of these modifications [28, 34]. Among these modified designs, the double channel flow microcapillary [40] is one of the most highly developed and useful designs, because of its hydrodynamic properties. This newly developed microcell will be discussed in the following section.

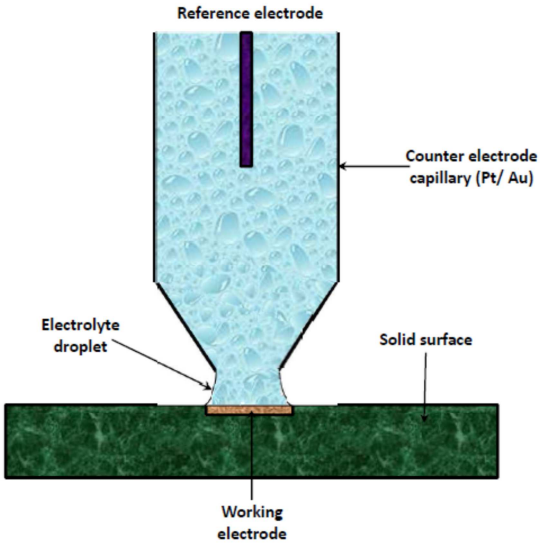

Figure 1.3. *Schematic design of a metal microcapillary with free droplet. Based on information obtained from [15, 31, 35].*

1.4. Applications in solid state electrochemistry

Previous studies have suggested applications of the microcapillary technique using different microcapillary designs [28, 34]. Here, we seek to classify these works into two major groups: corrosion studies and surface characterization.

1.4.1. Applications in corrosion studies

The majority of the microcapillary studies in the literature have focused on corrosion investigations of two groups of materials: stainless steel and aluminum alloys. There are, however, a few works that also consider the microelectrochemical corrosion of other metals and compounds, including iron.

Different types of stainless steel have been investigated on the micro scale using the microcapillary technique. As mentioned above, high–resolution microelectrochemical data obtained at low measured currents (in some cases even down to pA and fA [41]) using this technique give more detailed corrosion information. The extremely small exposed surface area allows users to localize the surface analysis and to investigate micro areas on different phases/areas of the measured surface. Therefore, even a single grain, inclusion, or micro crack on a solid surface can be measured.

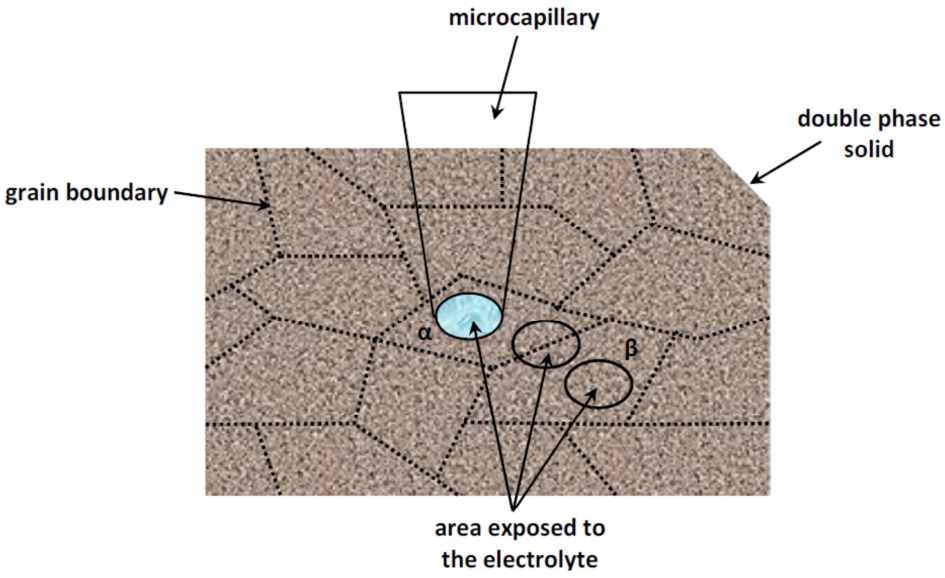

Figure 1.4. *Schematic drawing of a localized measurement by a microcapillary on a double phase metal–alloy. Based on information obtained from [29].*

Figure 1.4 shows a schematic sketch of a metal/alloy with two phases (α and β). This figure shows how a microcapillary can be positioned on a single grain, or even on a grain boundary. This procedure must be performed under a microscope, and, if necessary, after etching the surface.

Localized electrochemical impedance spectroscopy, electrochemical behavior of metallic and non–metallic inclusions and their effect on pit nucleation of steel and et. have been investigated by several researchers using microcapillary cell [9, 17, 18, 20, 21 ,23 ,25 ,29 ,34 ,41–56].

1.4.2. Applications in surface characterization

The second group of microcapillary studies can be classified as surface characterization studies of metals and alloys, in some cases coupled with other techniques. These studies are typically based on potential or impedance surface mapping, and mostly use electrochemical techniques such as cyclic voltammetry, amperometry, and potentiometry [57–63].

1.5. Some advantages and disadvantages

1.5.1. Advantages

As recently developed micro systems, capillary–based droplet cells have some important advantages that have made them popular in solid–state electrochemical surface analysis:

- The sample shape can be random, and no preparation is needed before measurements.
- The measured surface area can be controlled by the user, because of the small wetted area under the microcapillary.
- The mechanical stress on the surface is small [38].
- Various electrochemical techniques can be applied using this technique.
- Due to its high limiting current and high current resolution, it provides more detailed information compared with conventional large scale electrochemical systems.
- It can be coupled with other analytical devices such as UV–visible spectrometers [40] or laser beam microscopes [30].
- Only small volumes of electrolyte are required.
- A wide range of capillary sizes can be used, from nanometer–sized [30] up to 1 mm.

– Surface scanning and mapping are possible using this technique, in contrast to conventional electrochemical techniques [28, 29, 35].
– Several measurements can be performed on a small sample.

1.5.2. Disadvantages

Despite the several key advantages of the microcapillary cell technique, it is necessary to consider some technical limitations in order to improve the obtained electrochemical results.

Some of the main limitations of this technique are listed as follows.

1.5.2.1. A high–resolution potentiostat is required

Due to the fact that high current densities and extremely high impedance values (yields of up to 10^{13} to 10^{14} Ω [34]) are measured using a few–μm^2 working electrode, a high input resistance and low input current potentiostat is required. According to Birbilis, the resolution of the potentiostat used limits the minimum useful size of the microcapillary [27].

1.5.2.2. Ohmic drop (resistance)

In electrochemistry, the Ohmic resistance (R_Ω) is the resistance between the working and counter electrodes. It has been shown [27] that the value of R_Ω is dependent on the geometry of the microcapillary used, which means that as the size of the tip decreases, R_Ω increases. This phenomenon typically has a greater influence on the measured data in micro systems than in conventional large scale systems, especially when the electrolyte used is not highly conductive. Birbilis et al. [27] therefore suggested that a quantitative evaluation should be made of the Ohmic drop in micro systems, using either the current interruption technique, or impedance spectroscopy at frequencies higher than 1000 Hz when the electrolyte is not conductive enough. Positioning the counter electrode close to the mouth of the microcapillary [15, 16, 28, 31, 35, 38] and using metallic–body microcapillaries (gold or platinum) that also act as a counter electrode [15, 31, 35] are some technical modifications that have been considered as measures to decrease the cell resistance.

1.5.2.3. Leakage and blockage of the microcapillary tip

A high–quality silicone gasket is necessary if the microcapillary is required to touch the surface; this will ensure a seal and prevent leakage of the electrolyte, and will also avoid crevice corrosion under the gasket. However, in many cases the products of the

anodic and the cathodic electrochemical reactions (e.g., oxygen and hydrogen bubbles, or corrosion product particles) can accumulate at the measured area and block the tip of the microcapillary, and therefore interrupt the electrical response during the measurement. Such undesirable drops in the electrochemical response are normally observed with greater intensity at the beginning of the measurement, especially with extremely small tip diameters. However, some researchers have suggested that the rate of the electrochemical measurements should be increased to avoid blockage of the microcapillary tip; for example, by using high potential sweep rates [27, 29, 57, 59].

1.5.2.4. Changing the composition of the static electrolyte during the measurement in single channel tips

There is no guarantee that the chemical composition of a μm^2 surface and the small volume of the immobile electrolyte above it will remain intact during an electrochemical measurement. In most cases, gas bubbles and corrosion products form a heterogeneous suspension above the wetted surface. Consequently, after the initiation of the electrochemical measurement, the solid–liquid environment under the tip of the microcapillary changes. This must be considered, especially if the measurement is run at low rates, if large current densities are produced, or if small tip diameters are used.

1.5.2.5. Undesirable effects of the surrounding area around the tip

During the anodic dissolution of metals/alloys, oxygen reduction occurs simultaneously at the surface–electrolyte interface. The rate of this cathodic process has a direct effect on the corrosion potential of the solid specimen. Recently, it has been proven [67] that the silicone gasket which is normally used to prevent leakage from the microcapillary does not act as an airproof wall against gases. It has been shown that the presence of gases around the trapped area under the microcapillary increases the rate of oxygen reduction, and this directly affects the measured current density and the corrosion potential. Therefore, it has been recommended [64] that the effects of the area surrounding the microcapillary should be considered, and that measurements should be performed under controlled (aerated) conditions.

1.6. Flow microcapillary setup

There is no doubt that the double–channel flow microcapillary setup is the most advanced microcapillary cell design for solid–state electrochemistry. However, few studies to date have considered the use of flow microcapillaries. The first attempts to

produce modified double channel flow glass microcapillaries were carried out by Lohrengel et al. [38] in 2004. In fact, this modification solves the problem of the accumulation of gas bubbles and corrosion products in the microcapillary tip, which can change the chemical composition of the measurement environment by mobilizing the electrolyte through the surface of the specimen. Moreover, the risk of blockage of the microcapillary tip is reduced by the fluid flow.

Figure 1.5 shows a schematic view of a flow microcapillary attached to a solid surface. The main reason for this modification is to split the channel of the microcapillary into two separate parts: one for the electrolyte inlet and one for the outlet. A small part of the glass wall partition, close to the mouth of the microcapillary, is then removed by etching. Microliters of the electrolyte are pumped through the micro path above the tip, with various velocities. A thin gold or platinum wire is positioned inside one of the channels. Using this technique, fresh electrolyte is continuously injected into the inlet channel, and the corrosion products and gas bubbles are removed by the outlet stream. This technique is suitable for measuring current densities above 100 $A.cm^{-2}$ [38].

The micro flow cell idea was further developed by coupling it to an ICP–MS [65–70] and UV–visible [40, 71] spectrometry, allowing online in situ investigations of corrosion processes.

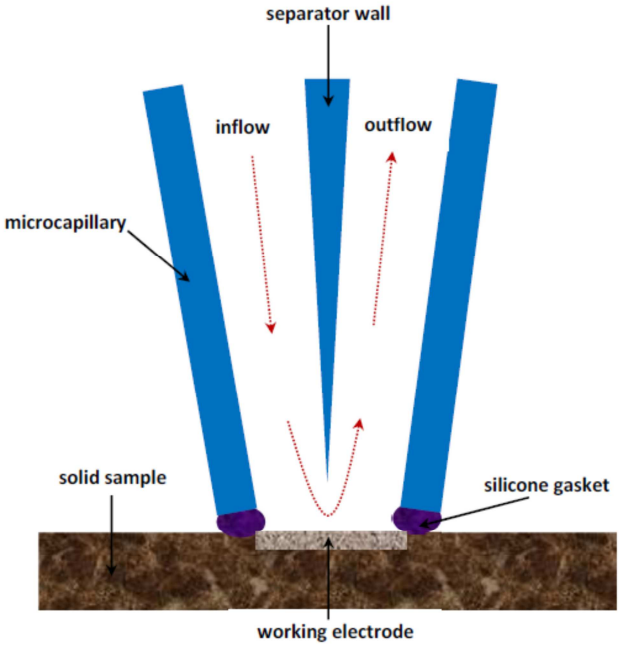

Figure 1.5. *Schematic view of a double channel flow microcapillary attached to a solid surface. Based on information obtained from [22, 38, 40, 65–71].*

1.7. Conclusions

Microcapillary electrochemical droplet cells have proven their capabilities in solid-state electrochemical surface analysis. Several microcapillary designs have been suggested by researchers to improve the performance and to overcome limitations and technical problems. A wide range of current densities can be measured using this technique. Its high–resolution electrochemical results make it possible to obtain more detailed information about corrosion processes and surface characterization. Recently developed flow microcapillaries have been coupled to various spectrometric techniques (e.g., UV–visible and ICP–MS), making this technique more powerful for solid–state surface analysis.

1.8. Outline of this work

Electrochemical corrosion studies are typically performed by conventional large scale techniques. However, there has always been a desire in electrochemistry to reach smaller diameters of the electrodes in order to use in electrochemical microanalyses, micro preparation and localized control of surface reactions. Large scale techniques are not able to obtain detailed information about localized processes. Despite recent developments in the field of microelectrochemistry, still majority of corrosion works are performed in macro scale. Therefore, the investigation of the corrosion processes on a micro scale needs more attention.

In this thesis, which is divided into 5 chapters, we have focused on the electrochemical corrosion processes of 304L and 316L stainless steels and pure copper in sodium chloride solution. Since these two groups of materials have different corrosion mechanism and different composition, it is useful to study their corrosion procedure on micro and macro scale under different conditions such as prior cathodic polarization.

Chapter 1 gives a general introduction about the microcapillary electrochemical droplet cell and its applications in solid state electrochemical surface analysis is described.

In Chapter 2 the history of stainless steels and copper, their applications and also their corrosion mechanisms in the presence of chloride ions is described.

In Chapter 3, 304L stainless steel is investigated in a sodium chloride solution on micro and macro scales by a microcapillary droplet cell and a conventional large scale setup and a comparison is made between the potentiodynamic polarization results obtained through these techniques.

Chapter 4 studies the effect of cathodic polarization processes on the corrosion behavior of 316L stainless steel on a large scale level under static and dynamic conditions with two different flow regimes and the results are compared with the microelectrochemical data of 304L stainless steel after cathodic polarization.

In Chapter 5, the influence of the pH and the chloride concentration on the electrochemical corrosion behavior of pure unalloyed copper is investigated and the results obtained by the microcapillary and conventional large scale techniques are compared. This chapter also models some corrosion parameters of copper such as the pitting potential, the corrosion potential and the stabilized passive current under various pH and chloride concentrations using an experimental design strategy.

Finally, a general conclusion and summary of all the performed works is provided in English and Dutch respectively.

Chapters 3 and 5 and also Section 4.2 of this dissertation have previously been published in Web of Science listed journals (see list of the publications at the end of this document).

Moreover, Chapter 1 will be submitted for publication as a review paper and Section 4.1 has been submitted for publication to Corrosion Science.

Bibliography

[1] www.library4science.com, chromatography book series, R. P. W. Scott, (last visit on 10.03.2013).

[2] T. Y. Liu, R. A. Boykins, Anal. Biochem. 182 (1989) 383–387.

[3] Z. I. Kovács, M. Palkovits, J. Neurosci. Meth. 190 (2010) 229–234.

[4] P. T. Charles, J. G. Rangasammy, G. P. Anderson, T. C. Romanoski, A. W. Kusterbeck, Anal. Chim. Acta 525 (2004) 199–204.

[5] Á. Végvári, Compreh. Anal. Chem. 46 (2005) 149–252.

[6] J.O. Park, C.H. Paik, R.C. Alkire, J. Electrochem. Soc. 143(8) (1996) L174–L176.

[7] R. Wen, B. Oakley II, J. Neurosci. Meth. 31 (1990) 207–213.

[8] K. Ogle, V. Baudu, L. Garrigues, X. Philippe, J. Electrochem. Soc. 147(10) (2000) 3654–3660.

[9] H. Böhni, T. Suter, A. Schreyer, Electrochim. Acta 40 (1995) 1361–1368.

[10] H. Krawiec, V. Vignal, J. Banas, Electrochim. Acta 54 (2009) 6070–6074.

[11] W. Brandl, Electrochim. Acta 37 (1992) 2263–2268.

[12] R. C. Alkire, K. P. Wong, Corros. Sci. 28 (1988) 411–421.

[13] A. M. Riley, D. B. Wells, D. E. Williams, Corros. Sci. 32 (1991) 1307–1313.

[14] P. C. Pistorius, G. T. Burstein, Electrochemical methods in corrosion research, Proc. 4th Int. Symposium, (edited by P. M. Natishan) Espoo (Finland), 429 (1991).

[15] M. M. Lohrengel, Electrochim. Acta 42 (1997) 3265–3271.

[16] A. W. Hassel, M. M. Lohrengel, Electrochim. Acta 42 (1997) 3227–3333.

[17] T. Suter, H. Böhni, Electrochim. Acta 42 (1997) 3275–3280.

[18] L. C. Abodi, J. A. D. Rose, S. Van Damme, A. Demeter, T. Suter, J. Deconinck, Electrochim. Acta 63 (2012) 169–178.

[19] M. Sanchez, N. Aouina, D. Rose, P. Rousseau, H. Takenouti, V. Vivier, Electrochim. Acta 62 (2012) 276–281.

[20] L. Paussa, F. Andreatta, N. C. R. Navarro, A. Duran, L. Fedrizzi, Electrochim. Acta 70 (2012) 25–33.

[21] M. Schneider, U. Langklotz, A. Michaelis, B. Arnold, Surf. Interf. Anal. 42 (2010) 281–286.

[22] H. Krawiec, V. Vignal, R. Akid, Surf. Interf. Anal. 40 (2008) 315–319.

[23] H. Y. Ha, C. J. Park, H. S. Kwon, Corros. Sci. 49 (2007) 1266–1275.

[24] G. Buytaert, Premendra, J. H. W. de Wit, L. Katgerman, B. Kering, H. J. Brinkman, H. Terryn, Surf. Coat. Tech. 201 (2007) 4553–4560.

[25] R. Oltra, V. Vignal, Corros. Sci. 49 (2007) 158–165.

[26] C. Stromberg, P. Thissen, I. Klueppel, N. Fink, G. Grundmeier, Electrochim. Acta 52 (2006) 804–815.

[27] N. Birbilis, B. N. Padgett, R. G. Buchheit, Electrochim. Acta 50 (2005) 3536–3544.

[28] M. M. Lohrengel, A. Moehring, M. Pilaski, Fresenius J. Anal. Chem. 367 (2000) 334–339.

[29] F. Arjmand, A. Adriaens, Electrochim. Acta 59 (2012) 222–227.

[30] L. Staemmler, T. Suter, H. Böhni, J. Electrochem. Soci. 151 (2004) G734–G739.

[31] M. M. Lohrengel, S. Heiroth, K. Kluger, M. Pilaski, B. Walther, Electrochim. Acta 51 (2006) 1431–1436.

[32] F. Arjmand, A. Adriaens, Int. J. Electrochem. Sci. 7 (2012) 8007–8019.

[33] F. Arjmand, A. Adriaens, Materials 5 (2012) 2439–2464.

[34] T. Suter, H. Böhni, Electrochim. Acta 47 (2001) 191–199.

[35] M. M. Lohrengel. A. Moehring, M. Pilaski, Electrochim. Acta 47 (2001) 137–141.

[36] J. W. Schultze, A. Bressel, Electrochim. Acta 47 (2001) 3–21.

[37] J. C. Eklund, A. M. Bond, J. A. Alden, R. G. Compton, Adv. Phys. Org. Chem. 32 (1999) 1–120.

[38] M. M. Lohrengel, C. Rosenkranz, I. Kluppel, A. Moehring, H. Bettermann, B. Van den Bossche, J. Deconinck, Electrochim. Acta 49 (2004) 2863–2870.

[39] L. Eng, E. Wirth, T. Suter, H. Böhni, Electrochim. Acta 43(12-20) (1998) 3029–3033.

[40] S. O. Klemm, J. C. Schauer, B. Schuhmacher, A. W. Hassel, Electrochim. Acta 56 (2011) 4315–4321.

[41] T. Suter, H. Böhni, Electrochim. Acta 43 (1998) 2843–2849.

[42] K. Osozawa, N. Okato, Proc. First Soviet–Japanese seminar on corrosion and protection of metals, (edited by Y. M. Kolotyrkin) Nauka Moskau, 229 (1979).

[43] R. A. Perren, T. A. Suter, P. J. Uggowitzer, L. Weber, R. Magdowski, H. Böhni, M. O. Speidel, Corros. Sci. 43 (2001) 707–726.

[44] E. Dubuisson, P. Lavie, F. Dalard, J. P. Caire, S. Szunerits, Electrochem. Comm. 8 (2006) 911–915.

[45] V. Vignal, H. Krawiec, O. Heintz, R. Oltra, Electrochim. Acta 52 (2007) 4994–5001.

[46] H. Y. Ha, H. Kwon, Electrochim. Acta 52 (2007) 2175–2180.

[47] V. Vignal, D. Ba, H. Zhang, F. Herbst, S. Le Manchet, Corros. Sci. 68 (2013) 275–278.

[48] M. Breimesse, S. Ritter, H. O. Seifert, S. Virtanen, T. Suter, Corros. Sci. 55 (2012) 126–132.

[49] S. U. Kim, H. Kwon, H. Kim, Solid State Phen. 124-126 (2007) 1533–1536.

[50] H. Böhni, T. Suter, F. Assi, Surf. Coa. Tech. 130 (2000) 80–86.

[51] A. Schreiber, C. Rosenkranz, M. M. Lohrengel, Electrochim. Acta 52 (2006) 7738–7745.

[52] H. Krawiec, S. Stanek, V. Vignal, J. Lelito, J. S. Suchy, Corros. Sci. 53 (2011) 3108–3113.

[53] J. A. De Rose, T. Suter, A. Balkowiec, J. Michalski, K. J. Kurzydlowski, P. Schmutz, Corros. Sci. 55 (2012) 313–325.

[54] O. Guseva, J. A. DeRose, P. Schmutz, Electrochim. Acta, 88 (2013) 821–831.

[55] H. Krawiec, Z. Szklarz, V. Vignal, Corros. Sci. 65 (2012) 387–396.

[56] C. Sorriano, R. Oltra, A. Zimmer, B. Vuillemin, C. Borkowski, Surf. Interf. Anal. (2013) DOI: 10.1002/sia.5223.

[57] F. Andreatta, M. M. Lohrengel, H. Terryn, J.H.W. de Wit, Electrochim. Acta 48 (2003) 3239–3247.

[58] K. A. Lill, A. W. Hassel, G. Frommeyer, M. Stratmann, Electrochim. Acta 51 (2005) 978–983.

[59] T. Hamelmann, M. M. Lohrengel, Electrochim. Acta 47 (2001) 117–120.

[60] M. M. Lohrengel, C. Rosenkranz, D. Rohrbeck, Microchim. Acta 156 (2007) 163–166.

[61] M. Pilaski, T. Hamelmann, A. Moehring, M. M. Lohrengel, Electrochim. Acta 47 (2002) 2127–2134.

[62] G. Hildebrand, A. Schreiber, M. Lohrengel, R. Strietzel, K. Liefeith, Corros. Sci. 48 (2006) 3629–3645.

[63] V. Vignal, H. Krawiec, O. Heintz, D. Mainy, Corros. Sci. 67 (2013) 109–117.

[64] R. Oltra, B. Vuillemin, F. Thebault, F. Rechou, Electrochem. Comm. 10 (2008) 848–850.

[65] N. Homazava, A. Ulrich, M. Trottmann, U. Krahenbuhl, J. Anal. At. Spectrom. 22 (2007) 1122–1130.

[66] N. Homazava, A. Ulrich, U. Krahenbuhl, Spectrochim. Acta B 63 (2008) 777–783.

[67] N. Homazava, T. Suter, P. Schmutz, S. Toggweiler, A. Grimberg, U. Krahenbuhl, A. Ulrich, J. Anal. At. Spectrom. 24 (2009) 1161–1169.

[68] N. Homazava, A. Shkabko, D. Logvinovich, U. Krahenbuhl, A. Ulrich, Intermetallics 16 (2008) 1066–1072.

[69] A. Ulrich, N. Ott, A. Tournier-Fillon, N. Homazava, P. Schmutz, Spectrochim. Acta B 66 (2011) 536–545.

[70] S. O. Klemm, A. A. Topalov, C. A. Laska, K. J. J. Mayrhofer, Electrochem. Comm. 13 (2011) 1533–1535.

[71] M. M. Lohrengel, I. Kluppel, C. Rosenkranz, H. Bettermann, J.W. Schultze, Electrochim. Acta 48 (2003) 3203–3211.

Chapter 2

Stainless steel and copper; history, applications and corrosion

2.1. Stainless steel

2.1.1. History

In metallurgy, the terms “stainless steel“, “inox steel“, and “inox“ describe a large group of iron alloys known for their high corrosion resistance and heat resistance. These properties are directly related to the chemical composition of stainless steel. The alloys consist of an iron base with added chromium; a minimum of 10.5% to 11% chromium is present, with a maximum of 30% [1, 2]. Other alloying elements such as molybdenum, nickel, copper, cobalt, vanadium, and aluminum may be observed in the composition of stainless steel. Nickel can be added to improve the microstructure and mechanical properties of steel, and molybdenum is added to enhance resistance against pitting [2]. In open air, an adherent chromium oxide (mainly Cr_2O_3) layer is immediately formed on the steel surface, providing a protective layer against corrosion phenomena. The name “steel“ implies that iron is the main element in this group of alloys. The term “stainless“ indicates the high resistance of these alloys against staining, pitting, and rusting in the atmosphere [1, 3, 4]. However, when the amount of iron falls to less than 50 %, the term “stainless“ can no longer be used [1].

The development of stainless steel started with investigation into the properties of ferrochromium. The first demonstration occurred when Berthier invented an iron alloy with about 1% chromium content. Further attempts were performed to alloy iron with either very high or very low chromium content, whilst maintaining high carbon content, but none achieved the desired chromium range. The closest result was the steel alloy which Hadfield demonstrated in 1892. Hadfield tested steel with almost 17% chromium content and greater than 1% carbon content in a 50% sulfuric acid solution, and reported that chromium decreased the corrosion resistance of the steel [1, 3, 4].

At the beginning of the 20^{th} century (1900–1915), the industrial significance of stainless steel was recognized. Simultaneously, the impact of carbon on the properties of iron was revealed. Developments in analytical devices and techniques, such as microscopy and X–ray diffraction, broadened the capabilities of the stainless steel

specialists. Finally, the puzzle of stainless steel was solved. In 1904, French scientist Leon Guillet investigated stainless steel and its composition, but didn't consider the high corrosion resistance of this alloy. During 1911–1912, German scientists performed the first detailed work regarding the corrosion resistance of stainless steel, and patented the first austenitic stainless steel with a combination of 21% chromium and 7% nickel. Harry Brearley introduced the first martensitic stainless in 1912 in Sheffield, England, which was discovered when seeking a corrosion–resistant alloy for use in gun barrels [1, 3, 4].

Initially, Brearly referred to the newly discovered alloy as "rustless steel". The term "stainless steel" was suggested by the British manufacturer Ernest Stuart. In 1914, stainless steel was used by George Ibberson & Co. to produce knives. This was the first commercial product made using stainless steel [4, 5]. Soon after, other types of stainless steel such as 18–8 SS (18% Cr, 8% Ni), 321 SS, 304 SS, and 316 SS were introduced.

Table 2.1 shows "austenitic", "duplex", and "ferritic" stainless steels and their respective compositions. These stainless steels are used today worldwide [1, 3, 6]. Each of the highlighted terms describes a metallurgical phase associated with the alloy.

Austenitic stainless steels contain both chromium and nickel. Ferritic stainless steels contain more than 10% –12% chromium without nickel, and duplex stainless steels have controlled amounts of ferrite and austenite, in addition to a percentage of molybdenum, in their structure.

Table 2.1. *Composition of austenitic, duplex, and ferritic grades of stainless steel. Based on information obtained from [1, 3, 6].*

Group of stainless steel	**Grade**		**Composition**		
	EN	AISI/ASTM	Cr (%)	Ni (%)	Mo (%)
Austenitic	1.4301 1.4401	304 316	17.5–19.5 16.5–18.5	8.0–10.5 10.0–13.0	– 2.0–2.5
Duplex	1.4162 1.4362 1.4462	S32101 S32304 S32205/S31803	21.0 22.0–24.0 21.0–23.0	1.5 3.5–5.5 4.5–6.5	0.3 0.1–0.5 2.5–3.5
Ferritic	1.4510 1.4509 1.4521	439 441 444	16.0-18.0 17.5–18.5 17.0–20.0	– – –	– – 1.8–2.5

The stainless steel grades shown in Table 2.1 have been listed based on the standards provided by three different organizations. The American Iron and Steel Institute (AISI) is one of the oldest associations of steel producers in USA, having been founded in 1855 [7]. The American Society for Testing and Materials (ASTM), formed in 1898, has more than 36,000 members and 132 standards committees, and is globally recognized as an international standards organization [8]. The European Standards (EN) are documents that have been ratified by one of the three European standards organizations (ESOs): the European Committee for Standardization (CEN), the European Committee for Electrochemical Standardization (CENELEC), or the European Telecommunications Standards Institute (ETSI) [9].

2.1.2. Applications

Since the 1920s, stainless steel has been used for facades and roofing. This alloy has some prominent properties which make it the preferred material for specific applications, with the possibility of various shapes and colors [6].

In recent decades, there has been a rapid increase in the annual consumption of stainless steel, particularly in construction. For example, in 2006, almost four million tons of stainless steel was used in construction alone. This is more than 14% of the total used worldwide. Today, various types of stainless steel are used in vast quantities in industry, construction, and as architectural elements [6].

Although one can easily prepare an extensive list of applications of various types of stainless steel, the main applications can be classified into one of three major fields [1, 2].

- Applications for resistance against atmospheric corrosion.
  In this field, various types of stainless steel are used in buildings, art, rolling stocks, the automobile industry, furniture, power generators and etc.
- Applications for resistance against aggressive mediums.
  These applications involve food preparation and serving equipment, agriculture, textiles, hospital equipment, chemical laboratory equipment, and petrochemical industries.
- Applications for resistance against high temperatures.
  Some of the applications mentioned above, such as petroleum chemistry equipment, can also be considered in this group. In addition, stainless steel is very desirable for specific applications such as in aircraft industries and space vehicles.

Figure 2.1 depicts three examples of the use of stainless steel in outdoor architecture [6, 10].

Figure 2.1. *The upper image shows the stainless steel floor in the Luxembourg Chamber of Commerce. The center image shows the Celtic Gateway Bridge in Holyhead, United Kingdom [6] (with permission from Elsevier). The lower image shows a 304 stainless steel sphere at the National Research Council, Ottawa, Canada [10] (with permission from Canadian Conservation Institute).*

More information about stainless steel, and its corrosion mechanisms, applications, and structure, is presented in the literature [11, 12].

2.2. Copper

2.2.1. History and applications

When considering the existence of human civilization on this planet, one cannot ignore the role of copper as one of the most important metals in ancient civilizations. There is evidence of the use of copper dating back more than 10,000 years [10]. Even today, copper is one of the most frequently used metals, with a wide variety of applications in modern society.

The word “copper” and its Latin name “cuprum” come from the word “cyprium”, meaning metal from Cyprus. During the Roman era, this island was significant as a source of smelted copper. Some believe that copper was first discovered in Cyprus, and Roman mythology supports this idea. In the modern period, a combination of the words copper and Cyprus is used to denote copper, “Cu”, in the periodic table [13].

Figure 2.2 shows a dendritic copper mass found in eastern North America. This copper sample is from the collection of David Scott, and the image was first published in 2002 [13].

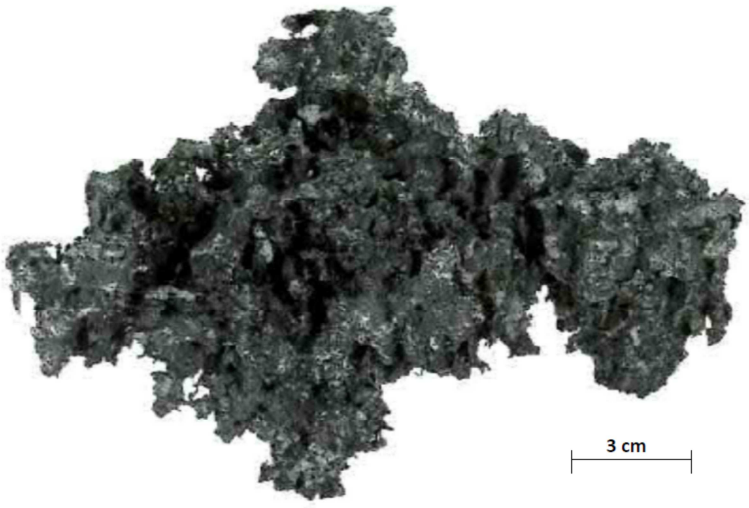

Figure 2.2. *A dendritic mass of native copper [13] (with permission from The Getty Conservation Institute).*

Copper is a readily available, cheap, non–ferrous, non–magnetic metal with excellent thermal and electrical conductivity and good mechanical workability. It can be easily

soldered and brazed, and is normally alloyed with other elements such as zinc, nickel, and tin to make its structure harder. Copper artifacts are normally in the form of copper alloys, mostly bronze [10, 13]; however, there are many examples of historical objects made from unalloyed copper.

Due to its excellent material properties, copper can be used as a conductor in electrical power lines, in the electronics industry, in communications, heat exchangers and heat conductors and in various atmospheric and marine environments, as well as in the production of various alloys [14, 15]. Copper sheets can also be used, after hammering, in works of art, roofing, coins, mirrors, and also in nuclear waste disposal [15]. Further examples of copper and copper–based products which surround us in our daily lives are copper cookware, decorative fittings, copper compounds in pigments and glass colorants, and new materials such as copper barium yttrium oxide which is used as a superconductor [13]. Figure 2.3 shows a historical artifact of unalloyed copper found in Peru, and also the use of copper in modern day roofing.

Figure 2.3. *The upper image shows a copper face mask from the Moche culture, Peru, dating from the second century C. E. The corrosion products are a mixture of malachite and cuprite. Image from the Santa Barbara Museum of Art. The height of the piece is 22.86 cm, and the width 16.51 cm [13] (with permission from The Getty Conservation Institute). The lower image shows copper roofing on the Chateau Laurier hotel in Ottawa, Canada. The green–colored copper is old (circa. 1912) and the red colored parts were replaced in 1990–91. The photograph was taken in 1993 [10] (with permission from Canadian Conservation Institute).*

More information about copper, its applications, and corrosion mechanisms can be found in the literature [16–19].

2.3. Corrosion and its mechanisms in aqueous environments

Despite the common idea regarding corrosion, which considers the formation of rust on iron and steel under the effect of water, corrosion can occur in different environments for various materials, such as metals, semiconductors, polymers, insulators, and ceramics.

Corrosion is important to consider, as the results are highly costly for the world economy. In particular, modern industries have to consider spending a large amount of their budget every year to protect themselves against different types of corrosion and to renovate equipment damaged by corrosion. According to recent estimates, every year an important part of the gross national product of the industrial countries is lost to managing corrosion phenomena. Therefore, additional funding and detailed research should be implemented to help solve the current corrosion problems, and to predict and overcome this growing economic issue [20].

Most corrosion phenomena have an electrochemical nature [21]. However, mechanical corrosion, such as erosion corrosion under the effect of mechanical forces such as fluid flow or mobile solid particles, can also be described as a corrosive phenomenon.

In principle there are two major categories of corrosion. “general corrosion” describes the loss of mass of metals and alloys through processes such as breakdown. Copper and all types of stainless steel have enough resistance against this type of corrosion to be considered for use in atmospheric or marine environments.

The second category is known as “localized corrosion”, and consists of phenomena such as pitting, crevice corrosion, and stress corrosion cracking. Different metals and alloys show different resistances toward each type of corrosion, depending on the composition of the metal and the corrosive environment [22].

The term “localized corrosion” is usually applied when a specific type of corrosion attack, in the presence of chloride ions, occurs. In most corrosion studies, a general corrosion rate is calculated. However, problems with this method occur when the corrosion becomes localized. In many cases, localized corrosion attack is only detected after serious damage has occurred.

2.3.1. Electrochemical methods in corrosion studies

There are multiple methods available to corrosion research, many of which are electrochemical. Due to the simplicity, low cost, and unique properties of recently developed electrochemical methods, which enable better understanding of the mechanisms and kinetics of electrochemical phenomena, these methods are well established in solid state analysis and corrosion studies. The description of the

polarization methods and electrochemical impedance spectroscopy used in the following chapters is given here.

When corrosion occurs in aqueous environments, the process takes place at the metal–electrolyte interface. It is well known that, from an aqueous electrochemical point of view, corrosion of a metal or an alloy mainly involves two reactions: oxidation (dissolution) of the metal and reduction of an oxidizing agent such as oxygen. During localized corrosion, the anodic dissolution reaction is physically well–separated from the cathodic reduction reaction. Therefore, in situ study of the anodic and cathodic reactions is easier than in the case of general corrosion [23].

At this point, it is necessary to note that although the term “electrochemical corrosion” is typically used for anodic dissolution of metallic elements, cathodic corrosion of metals is also known as a corrosion process, particularly in media with high hydrogen content. This type of corrosion, and its effect on the typical anodic corrosion, is discussed in detail in Chapter 4 of this dissertation. At this point, the theory of anodic corrosion is described.

When electrochemical corrosion occurs, during the anodic partial reaction the metal loses electron and simultaneously cations such as proton or molecules such as oxygen and water get reduced by receiving the electrons. The corrosion rate depends on the kinetics of both anodic and cathodic partial reactions which occur in the metal–electrolyte interface.

Figure 2.4 shows the mechanism of corrosion in a metal–electrolyte interface with the interrelated anodic and cathodic reactions. In this figure three processes can be observed: (1) an oxidation process which passes the metallic cations into the solution and releases the electrons over the metal surface, (2) a flow of the released electrons from the anode with low electric potential to the cathode with high electric potential and finally (3) a reduction process which receives the released electrons. Elimination of any of these steps or generation of any obstacle against them will decrease the corrosion of the metal. The second process mentioned above occurs faster than the other two processes. Therefore, we consider the electrochemical corrosion process in two stages: anodic dissolution of the metal and cathodic reduction of some ions or molecules [24].

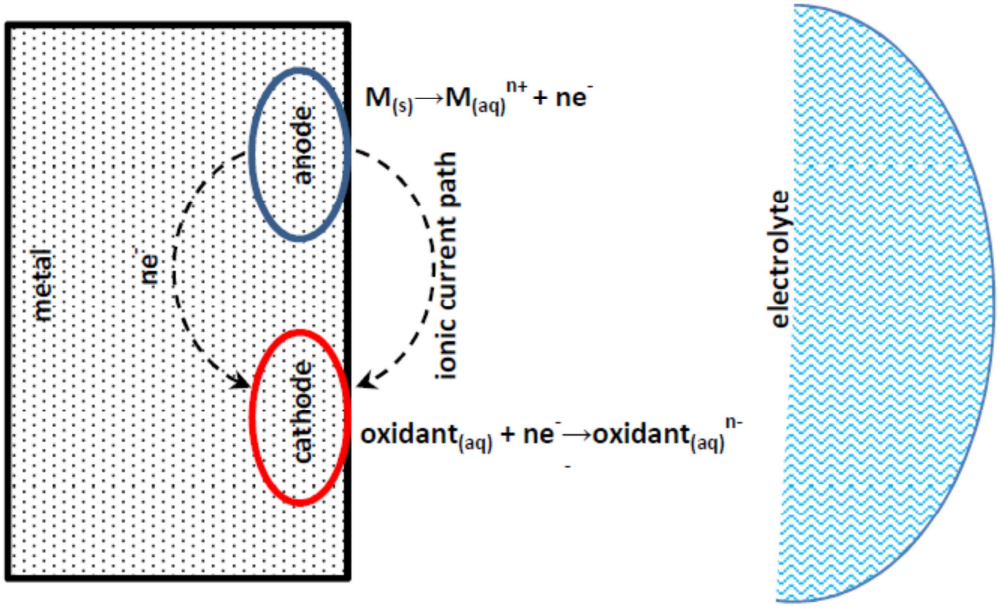

Figure 2.4. *Electrochemical corrosion mechanism occurring in a metal–electrolyte interface (M: metal, ne⁻: n mol of electrons). Based on information obtained from [24].*

In the 1830s, the English scientist Michael Faraday showed that there is a linear relationship between the metal dissolution rate (D_M) and the anodic current density obtained during the metal dissolution, as follows:

$$D_M = \frac{i_{a.M}}{nF} \qquad (2.1)$$

where n is the charge number, equivalent to the number of electrons exchanged during the metal dissolution process; F is the Faraday constant (96,485 C.mol^{-1}); and $i_{a.M}$ is the anodic current density of the metal [21, 24].

If we know the electrode potential of a metal in an electrolyte, we can predict whether that metal would corrode or not.

The standard electrode potential (E_0), for example the potential of a Fe/Fe^{2+} electrode, is usually measured by combining it with a standard electrode such as the hydrogen electrode (SHE) in an electrochemical cell. Furthermore, the standard electrode potential can be calculated through the standard Gibbs free energy (G^{o}_{298}) as follows [20]:

$$\Delta G^{0}_{298} = -nFE_0 \qquad (2.2)$$

ΔG^{o}_{298} is the change of the Gibbs energy of the equilibrium reaction between Fe and Fe^{2+}, n is the number of electrons and F is the Faraday constant. The equilibrium electrode potential (E_{eq}) however, is calculated through the Nernst equation [20]:

$$E_{eq} = E_0 + \frac{RT}{nF} \ln \frac{a_{ox}}{a_{red}} \qquad (2.3)$$

In this equation R is the gas constant (8.315 J/K.mol), T is the absolute temperature (298 K) and a is the activity of the oxidant (Ox) or the reductant (Red). At 25 ^{o}C Equation 2.3 is written as [20]:

$$E_{eq} = E_0 + \frac{0.0591}{n} \log \frac{a_{ox}}{a_{red}} \qquad (2.4)$$

During a corrosion process, oxidation occurs when the potential reaches the values higher than the E_{eq} and the reduction reaction occurs at potentials less positive than the E_{eq}.

Some examples of the oxidation and the reduction reactions are shown in Table 2.2 with their related equilibrium potentials versus SHE.

Table 2.2. *Some oxidation/reduction reactions required for corrosion in aqueous solutions. Based on information obtained from [20].*

Type	Reaction	E_{eq} vs. (SHE) at 25 ^{o}C
Oxygen reduction (acidic conditions)	$O_2 + 4H^+ + 4e^- \rightarrow 2H_2O$	$E_{eq} = 1.228 - 0.0591pH + 0.0148\log P_{O2}$
Oxygen reduction (neutral/alkaline conditions)	$O_2 + 2H_2O + 4e^- \rightarrow 4OH^-$	$E_{eq} = 0.401 - 0.0148pH - 0.0591\log[OH^-]$
Hydrogen evolution	$2H^+ + 2e^- \rightarrow H_2$	$E_{eq} = 0.000 - 0.0591pH$
Water reduction (neutral/alkaline conditions)	$2H_2O + 2e^- \rightarrow H_2 + 2OH^-$	$E_{eq} = -0.828 - 0.0591\log[OH^-] - 0.0295\log P_{H2}$
Iron oxidation	$Fe \rightarrow Fe^{2+} + 2e^-$	$E_{eq} = -0.440 + 0.0295\log[Fe^{2+}]$
Fe^{2+} oxidation	$2Fe^{2+} + 3H_2O \leftrightarrow Fe_2O_3 + 6H^+ + 2e^-$	$E_{eq} = 0.728 - 0.177pH - 0.0591\log[Fe^{2+}]$
Copper oxidation	$Cu \rightarrow Cu^{2+} + 2e^-$	$E_{eq} = 0.339 + 0.0295\log[Cu^{2+}]$

2.3.1.1. Potentiodynamic polarization

When a metal is in contact with an oxidizing electrolyte an electric potential value is formed on its surface when the two anodic and cathodic reactions take place simultaneously. This potential is called the corrosion potential (E_{corr}). At this potential the rates of anodic and cathodic partial reactions and therefore, the oxidation and the reduction current densities are equal. E_{corr} is measured by two ways. The first way is based on measuring the E_{corr} vs. a reference electrode when there is no current flow over the metal surface. This is called E_{corr} at open circuit potential. The second method is measuring the E_{corr} by scanning the potential window and measuring the produced oxidation and the reduction current. This method called potentiodynamic polarization will be discussed in more details in the next sections.

Figure 2.5 shows the current density–potential curve for a metal dissolution and a cathodic reduction of a redox system. In this figure the E_{eq} values are calculated according to the Eq. 2.3 and 2.4 . i_0 of the metal and the redox system is the exchange current density which represents the equal anodic and cathodic current density which pass the metal–electrolyte interface when the electrode potential is at the equilibrium value (E_{eq}) [20].

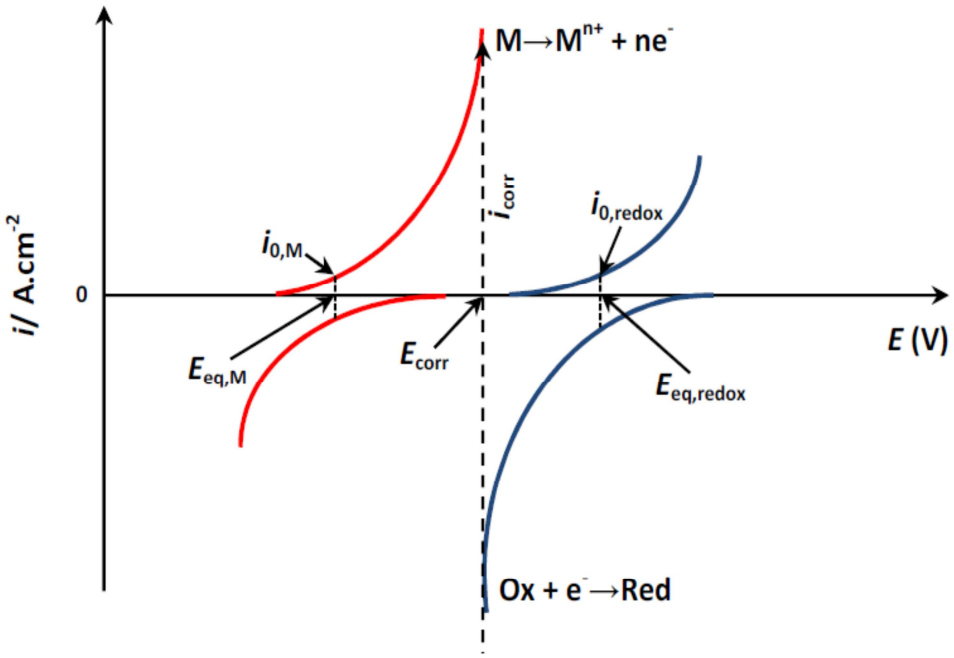

Figure 2.5. *Current density–potential curves of a metal and a redox electrode. $E_{eq,M}$ and $E_{eq,redox}$ are the equilibrium potentials of the metal and the redox electrode respectively, $i_{0,M}$ and $i_{0,redox}$ are the exchange current densities of the metal and the redox electrode respectively, i_{corr} is the corrosion current density and E_{corr} is the corrosion potential. Based on information obtained from [20].*

Based on the Butler–Volmer equation the sum of the anodic and the cathodic partial current densities can be calculated as follows [20].

$$i_t = i_0[\exp\frac{\alpha zFE_a}{RT} - \exp\frac{-(1-\alpha)zFE_c}{RT}] = i_a + i_c \qquad (2.5)$$

In this equation i_t is the sum of both anodic and cathodic current densities, i_0 is the exchange current density, α is the charge transfer coefficient, z is the number of charges that are transferred during a charge transfer reaction, F is the Faraday constant, E_a is the anodic electrode potential, E_c is the cathodic electrode potential, T is the temperature (298 K), R is the gas constant (8.315 J/K.mol) and i_a and i_c are the anodic and the cathodic current densities respectively.

In the Butler–Volmer equation there are some points which need to be considered. Usually it is recommended to replace n, the number of exchanged electrons, by z which represents the number of charges transferred because the numbers may be different. The charge transfer coefficient (α) has a value between 0 and 1. However, usually values between 0.2 and 0.8 are found for α. Furthermore, at the Nernst equilibrium potential (E_{eq}) described above the total current density is zero. However, in practice, when the electrochemical reaction is not fast enough, there is normally a potential deviation called anodic or cathodic overpotential ($\eta = E_{eq} - E_0$). This overpotential value can be positive (for anodic processes) or negative (for cathodic processes) and has three main reasons. (1) diffusion overpotential, (2) reaction overpotential and (3) charge transfer overpotential. In a slow electrochemical reaction at least one of these overpotentials is dominant [20].

Introducing the anodic and the cathodic overpotentials (η_a, η_c) in the Butler–Volmer equation (Eq. 2.5) yields the new format of the Butler–Volmer equation expressed as [20]:

$$i_t = i_0[\exp\frac{\alpha zF\eta_a}{RT} - \exp\frac{-(1-\alpha)zF\eta_c}{RT}] = i_a + i_c \qquad (2.6)$$

When the Butler–Volmer equation is used for investigating the corrosion of a metal, the anodic and the cathodic partial reactions will refer to two different redox electrodes, one for the metal (for example Fe/Fe^{2+}) and one for the oxidant (for example H_2/H^+). The combination of the oxidation reaction of the metal and the reduction reaction of the oxidant will form a new electrode called mixed redox

electrode. The development of the mixed electrode method, was published by Wagner and Traud in 1938 [25].

The corrosion format of the Butler–Volmer equation can be expressed as [20]:

$$i_t = i_{corr}[\exp\frac{\alpha zF(E_a - E_{corr})}{RT} - \exp\frac{-(1-\alpha)zF(E_c - E_{corr})}{RT}] \qquad (2.7)$$

In this equation the overpotential represents any deviation of the electrode potential from E_{corr}. This deviation is called polarization and results in an exponential increase in the anodic or the cathodic current density.

A semi–logarithmic *i–E* plot (log *i* vs. *E*) called Tafel plot (or Evans plot) yields the lines of the anodic and the cathodic current densities as presented in Figure 2.6 for a mixed electrode of a metal and an oxidant.

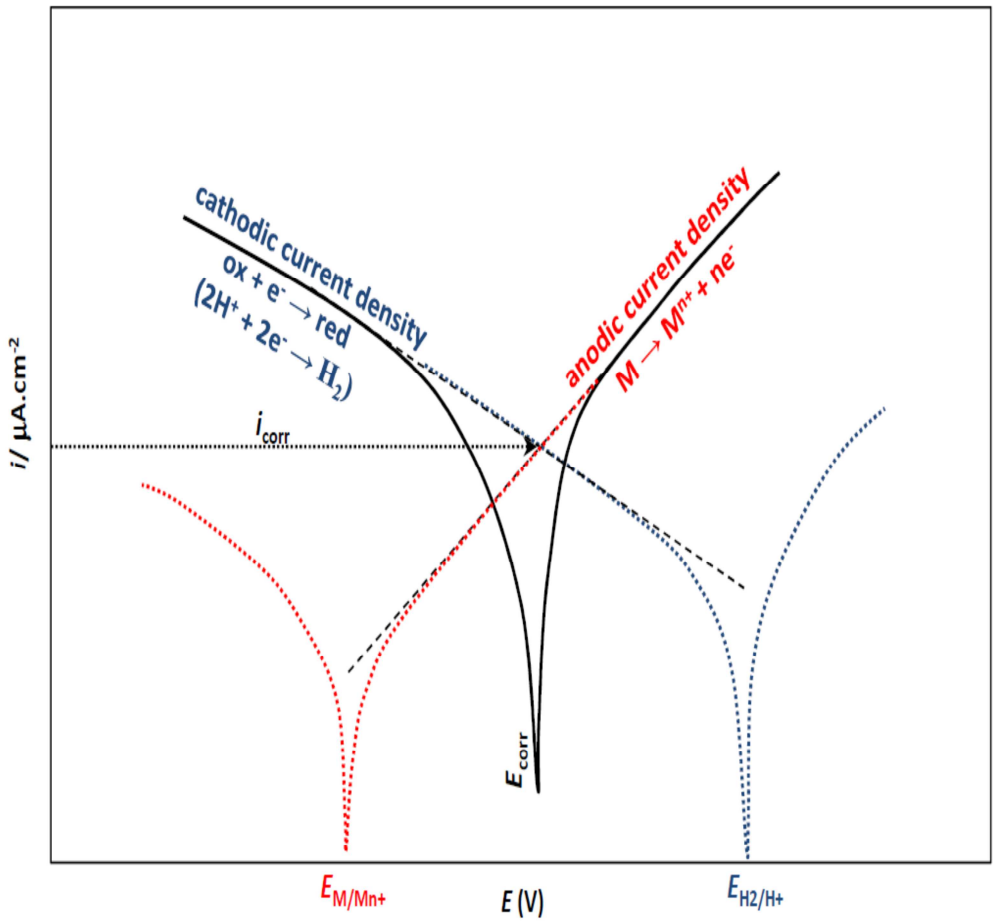

Figure 2.6. *Tafel plot (log i vs. E) of a metal dissolution representing the anodic and the cathodic current densities of the single and the mixed redox electrodes. Based on information obtained from [20, 24].*

Finally, according to the Butler–Volmer equation for anodic and cathodic reactions the total current density is expresses respectively as follows [20]:

$$\log i_t = \log i_{corr} + \frac{\alpha z F (\mathrm{E}_a - \mathrm{E}_{corr})}{2.3RT} \qquad (2.8)$$

$$\log i_t = \log i_{corr} - \frac{(1-\alpha) z F (\mathrm{E}_c - \mathrm{E}_{corr})}{2.3RT} \qquad (2.9)$$

2.3.1.2. Electrochemical impedance spectroscopy

Electrochemical Impedance Spectroscopy (EIS) has been popular in electrochemistry during recent years. Initially it was applied to the determination of the double–layer capacitance [26–29] and in ac polarography [30–32]. It is now applied to the characterization of electrode processes and complex interfaces. EIS studies the system response to the application of a periodic small amplitude ac signal. These measurements are carried out at different ac frequencies and, thus, the name impedance spectroscopy was later adopted. Analysis of the system response contains information about the interface, its structure and reactions taking place there. EIS is now described in the general books on electrochemistry [33–35], specific books on EIS [36] and there are also numerous articles and reviews [31, 37, 38].

Recent advances in the measurement and analysis of EIS data has ensured the popularity of the method in corrosion research. Impedance spectroscopy is usually used to study the interface conditions: measuring the dielectric and transport behavior of materials, investigating the corrosion resistance and rate, and examining the microstructure of passive surfaces [39, 40]. Some major properties are considered to be powerful aspects of this technique [37].

- The linearity of EIS makes it possible to describe the obtained results according to the linear systems theory.
- Measurements over wide frequency ranges enable the accumulation of large amounts of data in a single measurement. Linear electrical response techniques require several measurements to achieve the same volume of data.
- High volumes of the useful information can be obtained through the investigation of relatively few experiments.

Here, the theoretical description of electrochemical impedance spectroscopy is provided.

Impedance spectroscopy involves applying a sinusoidal ac signal to an electrode and measuring the response versus time. Normally a small voltage is applied and the

resulting current is measured. The current–time and voltage–time measurements are processed and the impedance at different frequencies is provided.

Impedance is the term used to describe the ac equivalent of dc resistance. For dc the relationship between current and voltage is given according to Ohm's law:

$$V = iR \qquad (2.10)$$

Where V (in volts) is the voltage, R (in ohms) is the resistor and i is the current (in amps).

If the system is linear the current response to the applied sinusoidal potential will be sinusoidal, at the same frequency but with a phase shift [41, 42]. Figure 2.7 shows a current response to a sinusoidal potential with a phase shift.

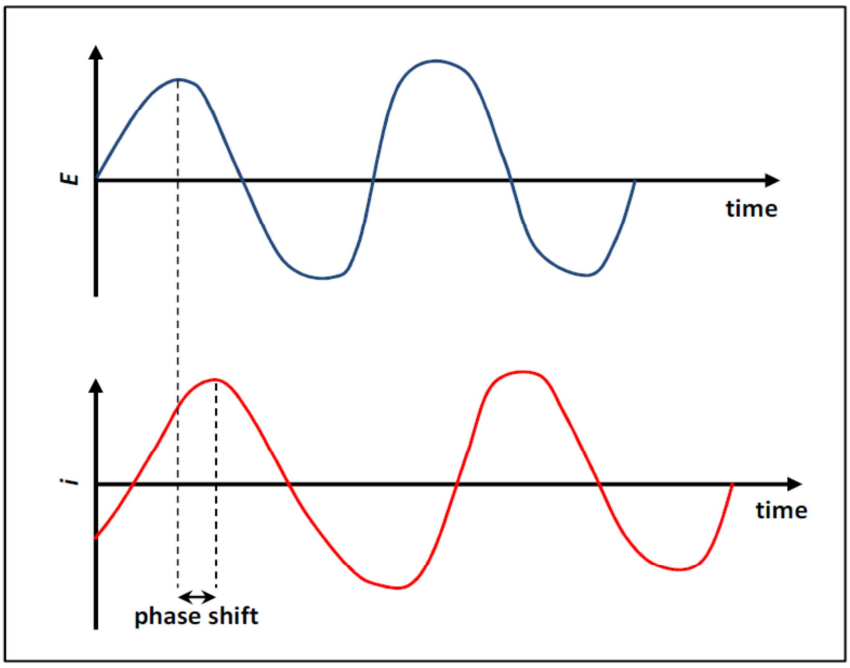

Figure 2.7. *Sinusoidal current response in a linear system. Based on information obtained from [41, 42].*

For ac signals Equation 2.10 is written as [41, 42]:

$$V = iZ \qquad (2.11)$$

Where Z is the impedance of the circuit. Unlike resistance, here the impedance value is depended to the frequency of the applied signal. For an ac signal, the frequency (f) in hertz, is the number of cycles per second.

The applied signal versus time is expressed as [41, 42]:

$$E_t = E_0 \sin(\omega t) \qquad (2.12)$$

E_t is the potential at time, E_0 is the amplitude of the applied signal and ω is the radial frequency.

In a linear system the current signal at time (i_t) is shifted in phase (Φ) with different amplitude (i_0) [41, 42]:

$$i_t = i_0 \sin(\omega t + \phi) \qquad (2.13)$$

And the impedance (Z) is calculated as [41, 42]:

$$Z = \frac{E_t}{i_t} = \frac{E_0 \sin(\omega t)}{i_0 \sin(\omega t + \phi)} = Z_0 \frac{\sin(\omega t)}{\sin(\omega t + \phi)} \qquad (2.14)$$

The total impedance of a system at a given frequency is defined by two terms, real impedance (Z') and imaginary impedance (Z''). These terms relate the output current to the input voltage of the system and the collection of their values for different frequencies is the impedance spectrum [41, 42]:

$$Z = Z' + Z'' \qquad (2.15)$$

The spectrum of the real impedance against the imaginary impedance is known as a Nyquist plot. The shapes of the spectra are important in qualitative investigation of the results. The following equations represent the relationship between the total impedance value, the real part, the imaginary part, and the phase shift value Ø [41, 42]:

$$|Z|^2 = Z'^2 + Z''^2 \qquad (2.16)$$

$$Z' = |Z| \cos\phi \qquad (2.17)$$

$$Z'' = |Z| \sin\phi \qquad (2.18)$$

Figure 2.8 represents a typical Nyquist plot provided by plotting the real impedance on the X–axis and the imaginary part on the Y–axis. In this plot the Y–axis (*Z"*) has negative values and the X–axis (*Z'*) has positive values. Each point on the Nyquist plot is the impedance at one frequency. Moreover, high frequency values in Nyquist plots start from the left side of the plot and low frequency values are observed on the right.

On the Nyquist plot the impedance can be represented as a vector. The angle between this vector and the Z' axis will be the phase shift (Φ).

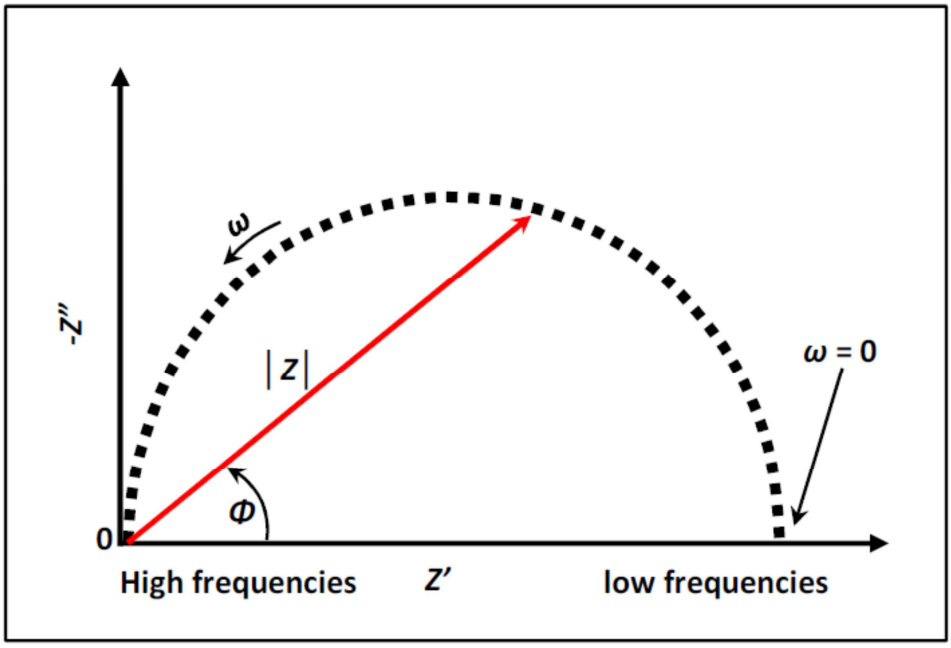

Figure 2.8. *A semi–circle Nyquist plot with impedance vector. Based on information obtained from [41].*

Another popular method for the presentation of impedance data is Bode plot. In a Bode plot $\log|Z|$ and phase shift (Φ) are plotted versus log of the frequency (f). Figure 2.9 is an example of a Bode plot with the frequency values.

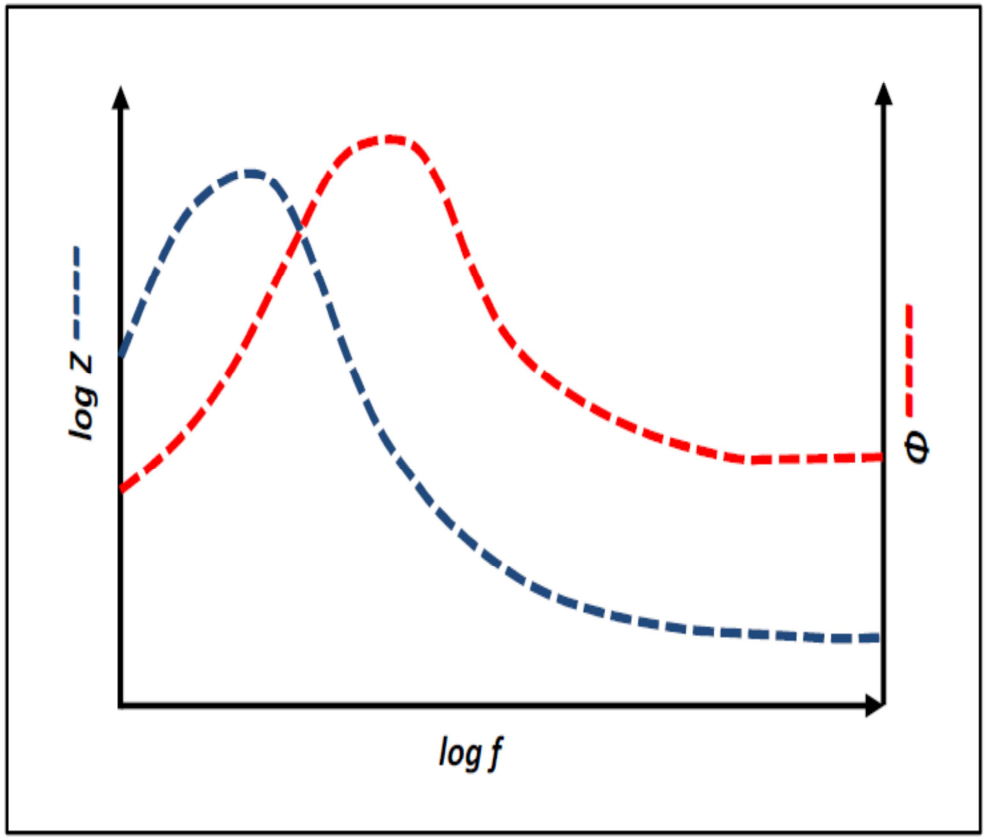

Figure 2.9. *Bode plot representing the variation of the impedance and the phase shift for different frequency values. Based on information obtained from [41, 42].*

EIS data is usually analyzed by fitting it to an equivalent circuit model. The elements used in circuit models are electrical elements such as resistors and capacitors. These elements can be combined in series or parallel and the constructed circuit models can be used to model various phenomena on an interface.

By applying an ac signal to a system, in addition to the polarization resistance of the surface (R_p), there will be a double layer capacitance (C_{dl}) produced by charge separation at the surface and also the resistance of the solution known as R_s. combination of these elements provides the equivalent circuit of the system.

The first attempts to use electrical analogs in electrochemical data analysis were performed by Ershler [43] and Randles [44] in the 1940s, and the simulation method has subsequently been used by many investigators. Various electrical circuit models suggested for different types of EIS plots can be found in [41, 42].

2.3.2. Pit nucleation

Metallic passivity was discovered in 1790 by Keir [45]. However, strangely until 1960s there was no evidence about the existence of the passive films over metals [46].

Nowadays it is well known that the corrosion resistance of the metal surface depends directly on the existence of a thin passive oxide or hydroxide layer in the range of some nano meters and its mechanical properties.

The pitting or the penetration mechanism requires the transfer of aggressive ions such as SO_4^{2-} and ClO_4^- or halides like Cl^-, F^- and Br^- through the passive layer into the metal surface. This process occurs locally and results in dissolution of the non–protected metal. The adsorption mechanism assumes the formation of complexes of metallic cations with the aggressive ions at the surface of the oxide layer. This metal dissolution which occurs on the still passivated surface reduces the thickness of the passive oxide film and finally leads to a local breakdown of the oxide layer and therefore, a free dissolution of the non–protected metal. The formation of these local breaks occurs due to the potential changes or due to the presence of aggressive ions or both together. Although normally the mobility of large anions like Cl^- through the oxide layer is slower than small metallic cations, under appropriate conditions the pitting takes place on the metal surface in less than 1 s. However, during the pitting, at the same time oxygen tries to repair the formed damage and closes the pit. The generated salts/corrosion products can help this deactivation process. Depending on the physical and the chemical conditions in the metal–electrolyte interface this pitting/repassivation (deactivation) competition ends with defeat of either the passive layer or the aggressive media. If the competition ends with the formation of an active pit, it can be easily detected by a rapid increase in the dissolution current density at the anodic part of the Tafel plot, usually at relatively high potentials. Moreover, for pit initiation, defects within the metal surface also have to be considered. Inclusions like MnS may prevent the formation of a well protecting oxide layer and act as preferential sites for a breakdown of the passivity [20]. Figure 2.10 shows the formation of a single pit by attacking aggressive ions and the simultaneous repassivation of the local break by a newly formed oxide layer.

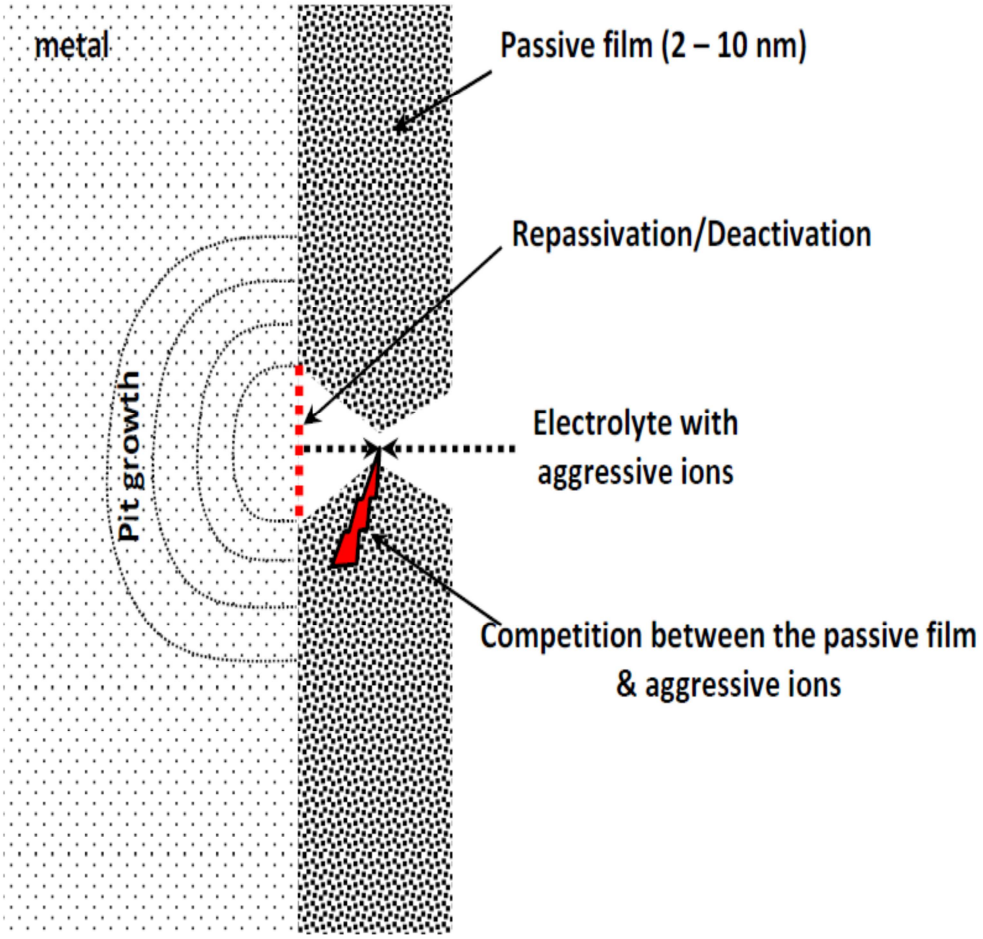

Figure 2.10. *Schematic view of the formation of a pit. Based on information obtained from [20].*

On a Tafel plot, the passivity and the dissolution regions of the oxide film can be detected at the anodic part of the graph. Figure 2.11 is a typical Tafel plot of a passive metal. In this *i*–*E* curve, at the anodic part, as the potential of the system increases, immediately after the E_{corr} the potential reaches the active region which the breakdown of the passivity and the metal dissolution occurs. At higher potentials, however, due to the repassivation of the surface, the current density generated by the metal dissolution decreases and the potential reaches the passive region. In this region the oxidation current density drops and no pitting is observed. Finally at relatively high potentials around the oxidation potential of water, a rapid increase of the oxidation current density is observed where the potential is in the transpassive region. The pit growth in this region is fast and the generated pits are active and deep enough. Therefore, these breaks cannot be easily repassivated or deactivated by the oxide layer.

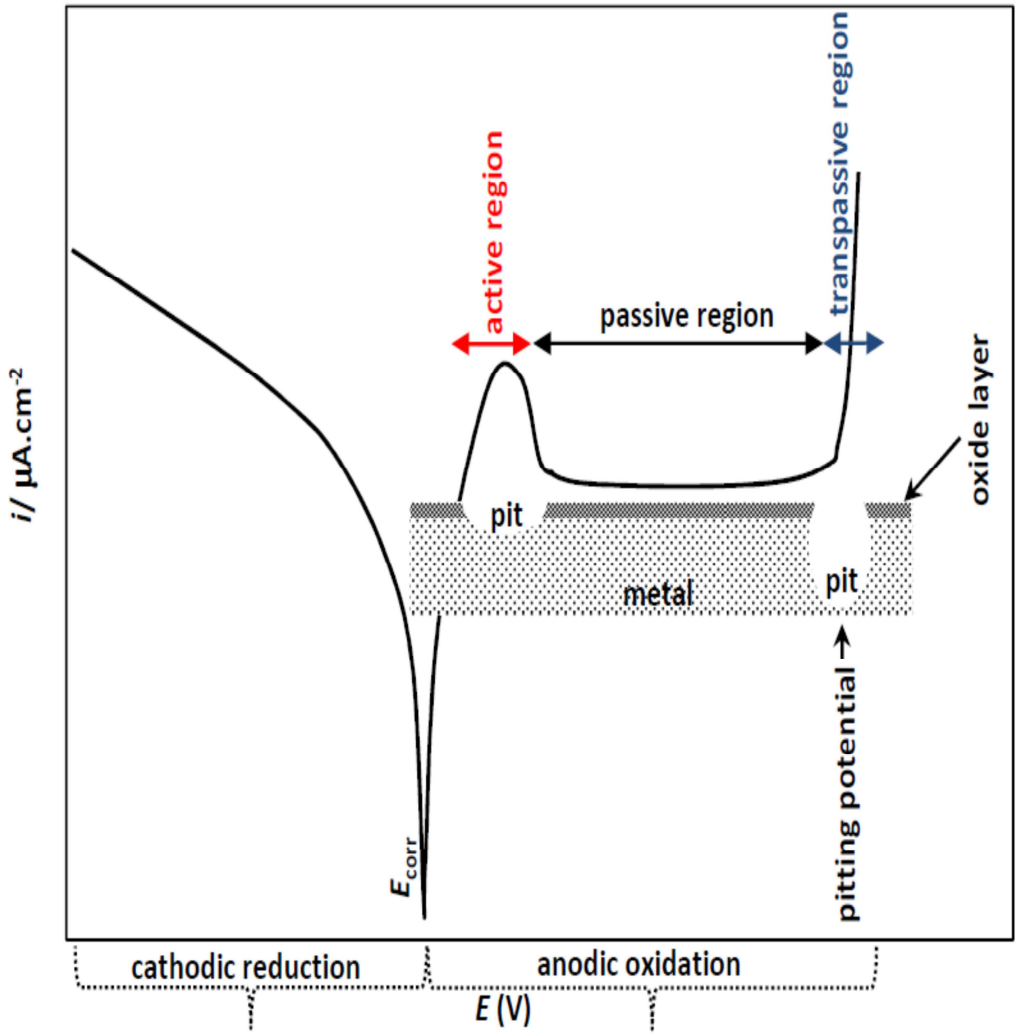

Figure 2.11. *Tafel plot of a metal dissolution with the pits and the passivation formed by shifting the potential from E_{corr} to the active potential, the passive potential and the transpassive potential respectively. Based on information obtained from [20].*

2.3.3. Aqueous corrosion of stainless steel

In the case of stainless steel, a stable and protective oxide layer forms quickly in open air, which reduces the rate of the charge and mass transfer processes that are required for corrosion. This oxide layer consists commonly of Cr(III) ions bonded to O^{2-} (mainly Cr_2O_3 with H_2O ligands) with a thickness of 0.3 to 2.5 nm [1, 20]. The corrosive environment first affects this protective layer. When aggressive ions such as halides act as the oxidizing agent, the corrosion of steel becomes a critical problem and this occurs in stainless steel despite extensive research to prevent the issue [47].

Passivity and activity (corrosion) of metals/alloys in different potentials and pHs are illustrated by Pourbaix diagrams. Here the Pourbaix diagrams of chromium and iron can be useful to see the stability of the passive film on steel and the dissolution potential of iron in various pH and potentials. The Pourbaix diagram of Cr in Figure

2.12 shows a large area in the middle of the plot where Cr_2O_3 is stable. Oxidation of Cr^o occurs on steel according to Equation 2.10:

$$2Cr + 3H_2O \rightarrow Cr_2O_3 + 6H^+ + 6e^- \qquad E_0 = -0.740 \text{ V vs. SHE} \qquad (2.19)$$

Cr_2O_3 precipitates over the steel surface and forms a protective layer on the steel surface. This oxide protects the steel surface from further attack. Moreover, this area is stable from pH 4 to pH 14. This gives the steel good acid protection.
In acidic solutions the passive film dissolution occurs as:

$$Cr_2O_3 + 6H^+ \rightarrow 2Cr^{3+} + 3H_2O \qquad (2.20)$$

Finally, in neutral pHs, at sufficiently positive potentials the transpassive film dissolution occurs as:

$$Cr_2O_3 + 5H_2O \rightarrow 2CrO_4^{2-} + 10H^+ + 6e^- \qquad (2.21)$$

And in alkaline pHs this reaction can occur as:

$$Cr_2O_3 + 10OH^- \rightarrow 2CrO_4^{2-} + 5H_2O + 6e^- \qquad (2.22)$$

The formed CrO_4^{2-} in presence of protons can react as:

$$2CrO_4^{2-} + 2H^+ \rightarrow Cr_2O_7^{2-} + H_2O \qquad (2.23)$$

At the region above Cr_2O_3, we can see that under strongly oxidizing conditions, according to Equations 2.21 and 2.22, Cr^{3+} can oxidize to Cr^{6+}, making the Cr_2O_3 surface unstable. The Pourbaix diagram of Fe shows that the unstable region of Cr (Cr^{6+}) is above the passive region of Fe. Therefore, in this region aggressive ions such as chlorides can attack easily the non–protected iron and cause pitting on the steel.
The Pourbaix diagram of Fe also contains the pH dependence of two important redox systems for metal dissolution, the H_2/H^+ and H_2O/O_2 electrodes.

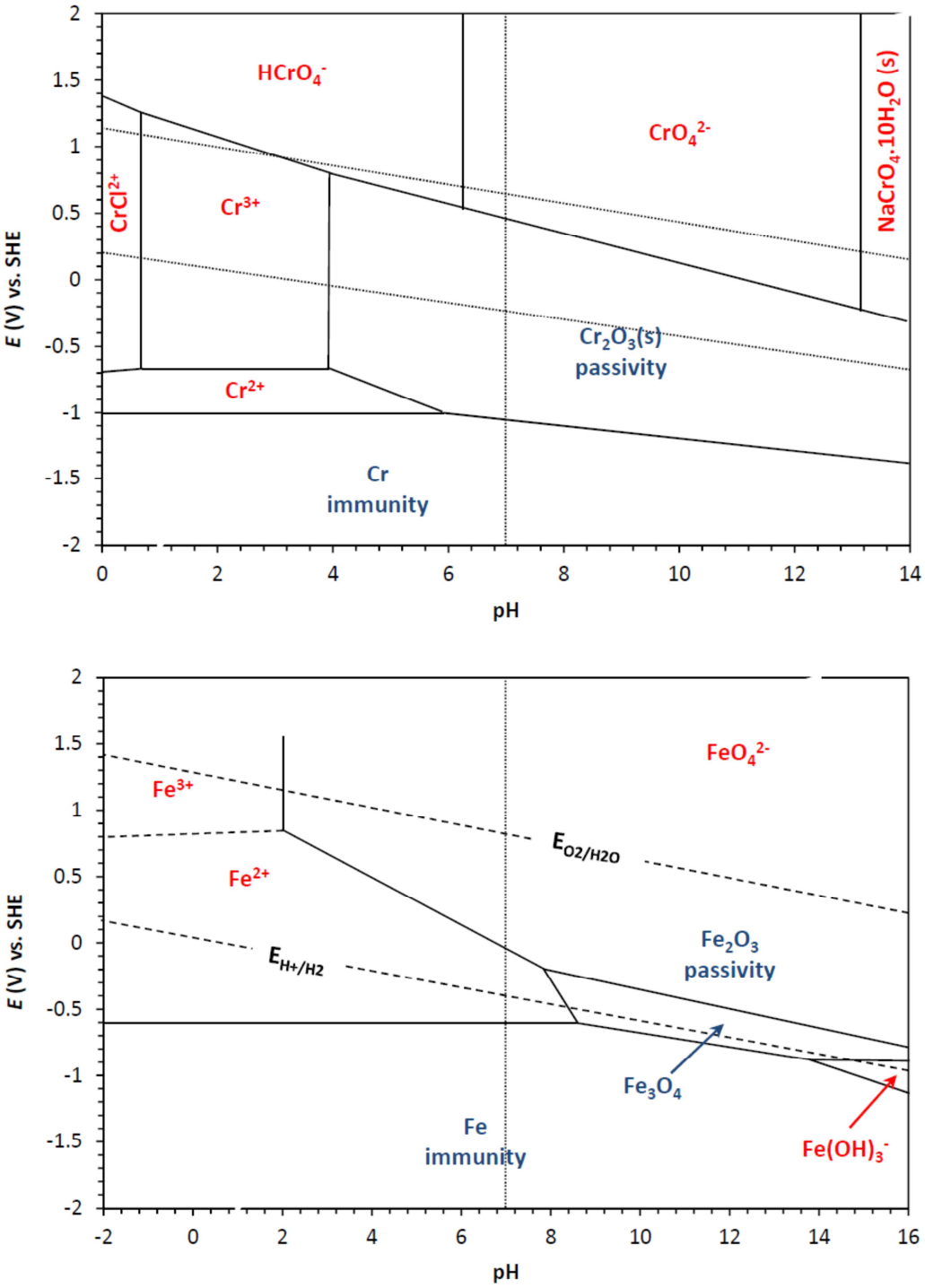

Figure 2.12. *Pourbaix diagrams of (above) chromium and (below) iron. Based on information obtained from [20, 48, 49].*

The electrochemical corrosion of steel in aqueous solutions is usually described by two partial reactions: the anodic dissolution of iron as follows:

$$Fe \rightarrow Fe^{2+} + 2e^{-} \qquad E_0 = -0.409 \text{ V vs. SHE} \qquad (2.24)$$

and simultaneous cathodic reduction of oxygen, water or hydrogen.

However, recent developments in electrochemical surface analysis techniques, such as a double channel microcapillary cell coupled to chemical analysis equipment (Section 1.6), have revealed that although the additional elements in multi–element alloys have higher corrosion resistance than the base metal, they may also be corroded under aggressive conditions.

Although no previous study has reported the multi–element quantitative corrosion process of stainless steel, Homazova et al. [50] performed a time–lapse in situ investigation of the elemental corrosion processes of Al alloys in sodium chloride solution. Their work describes the corrosion of elements such as chromium compared with the corrosion of the base metal (in this case Al).

In the case of the cathodic sub–process, in the vast majority of electrochemical corrosion processes the cathodic reaction is either oxygen and water reduction or hydrogen reduction or all three, depending on the pH of the medium.

In sodium chloride solutions with pH slightly lower than 7 the majority of the cathodic sub–process will be the reduction of the dissolved oxygen. However, as the pH decreases the role of hydrogen reduction becomes dominant.

In near neutral pH solutions reduction of water molecules occur as:

$$2H_2O + 2e^- \rightarrow H_2 + 2OH^- \qquad E_0 = \text{-0.828 V vs. SHE} \qquad (2.25)$$

In the case of oxygen however, in neutral and alkaline solutions the oxygen reduction process can follow two reaction paths: a four–electron pathway described by Equation 2.26, and a two–electron pathway described by Equation 2.27, which results in the formation of hydrogen peroxide.

$$O_2 + 2H_2O + 4e^- \rightarrow 4OH^- \qquad E_0 = 0.401 \text{ V vs. SHE} \qquad (2.26)$$

$$O_2 + 2H_2O + 2e^- \rightarrow 2OH^- + H_2O_2 \qquad E_0 = \text{-0.133 V vs. SHE} \qquad (2.27)$$

The four–electron process can occur through a direct pathway (Eq. 2.26) or an indirect pathway involving the formation of H_2O_2 through Equation 2.27, and then conversion of the produced H_2O_2 to OH^- through a two–electron process [51, 52].

In acidic solutions the oxygen reduction process occurs as:

$$O_2 + 4H^+ + 4e^- \rightarrow 2H_2O \qquad E_0 = 1.228 \text{ V vs. SHE} \qquad (2.28)$$

The chance of each reaction occurring depends on the composition of the electrode surface and experimental conditions. The oxygen reduction reaction has been observed to be influenced by the passive film structure of the 316L austenitic stainless steel surface [53]. According to Bozec et al. [54], in artificial seawater, oxygen reduction on a pre–reduced 316L or 904L stainless steel surface occurs via the four–electron pathway. However, when the reaction occurs on freshly polished steel, both two and four electron pathways are involved [53].

In addition to Equation 2.28, the hydrogen evolution reaction in general is represented by:

$$2H^+ + 2e^- \rightarrow H_2 \qquad (2.29)$$

The standard potential of this reaction at 25 ^{o}C under 1 atm pressure of hydrogen is 0 V vs. SHE and the equilibrium potential of this reaction in neutral solutions is about -0.4 V vs. SHE (according to the equation mentioned in Table 2.2).

The hydrogen evolution and ionization mechanism has been described based on three reactions.

The Volmer reaction suggests that [52]:

$$H^+ + e^- \rightleftharpoons H_{(ads)} \qquad (2.30)$$

According to the Tafel reaction the adsorbed hydrogen atoms can participate in a different reaction to form hydrogen molecules [52]:

$$2H_{(ads)} \rightleftharpoons H_2 \qquad (2.31)$$

Or by the Heyrovsky reaction [52]:

$$H_{(ads)} + H^+ + e^- \rightleftharpoons H_2 \qquad (2.32)$$

Finally part of the adsorbed hydrogen can be absorbed by the metal surface as:

$$H_{(ads)} \rightarrow H_{(abs)} \qquad (2.33)$$

Breakdown of the passive oxide layer can occur through the carbonation process or via a chloride attack. When atmospheric carbon dioxide dissolves in the pore water around the steel substrate, carbonic acid molecules are produced. The pH of the pore water then decreases until the passive layer is broken down. However, chlorides directly attack the weak points of the steel and form pits [55].

Pitting corrosion is an electrochemical oxidation–reduction process, which occurs within localized deeps on the surface of metals coated with a passive film. The pits often appear to be rather small at the surface, but may have larger cross–section areas deeper inside the metal. Since the attack is small at the surface and may be covered by corrosion products, a pitting attack often remains undiscovered until it causes perforation and leakage.

According to some researchers, corrosion is the result of a competition between aggressive ions, such as chlorides, and oxygen, which contribute to the destruction and repair of the protective oxide layer, respectively [56] (Figure 2.10). Chloride ions attack the protective oxide film and cause its breakdown, whilst oxygen simultaneously repairs the formed defects [57]. In fact the attacked sites are deactivated by formation of a new oxide film (mainly Cr_2O_3) in the pit which contains corrosion products. Therefore, pitting occurs when the rate of destruction of the oxide layer exceeds the rate of repair.

An initial pit may form on the steel surface covered by a passive oxide layer as a result of mechanical damage of the passive film (scratches), particles of a second phase emerging on the metal surface (These particles precipitating along the grains boundaries may function as local anodes causing localized galvanic corrosion and formation of initial pits) or localized stresses in form of dislocations emerging on the surface which may become anodes and initiate pits. Also, non–homogeneous environment may dissolve the passive film at certain locations where initial pits form.

Figure 2.13 illustrates the mechanism of the electrochemical pitting corrosion over a steel under chloride attack. The electrons given up by the anode flow to the cathode where they are discharged in the cathodic reaction. The electrolyte enclosed in the pit gains positive electrical charge in contrast to the electrolyte surrounding the pit, which becomes negatively charged. The positively charged pit attracts negative ions of chlorine Cl^- increasing acidity of the electrolyte according to the reaction:

$$FeCl_2 + 2H_2O \rightarrow Fe(OH)_2 + 2HCl \qquad (2.34)$$

pH of the electrolyte inside the pit decreases to acidic pHs, which causes further acceleration of corrosion process. Large ratio between the anode and cathode areas favours increase of the corrosion rate. The formed Ferrous hydroxide ($Fe(OH)_2$) is unstable in presence of oxygen and therefore, Ferric hydroxide ($Fe(OH)_3$) will be formed (Eq. 2.35). Corrosion products ($Fe(OH)_3$) form around the pit resulting in further separation of its electrolyte. Moreover, the formed Ferric hydroxide is insoluble in water and precipitates. This precipitate is not protective [58, 59].

$$4Fe(OH)_2 + O_2 + 2H_2O \rightarrow 4Fe(OH)_3 \qquad (2.35)$$

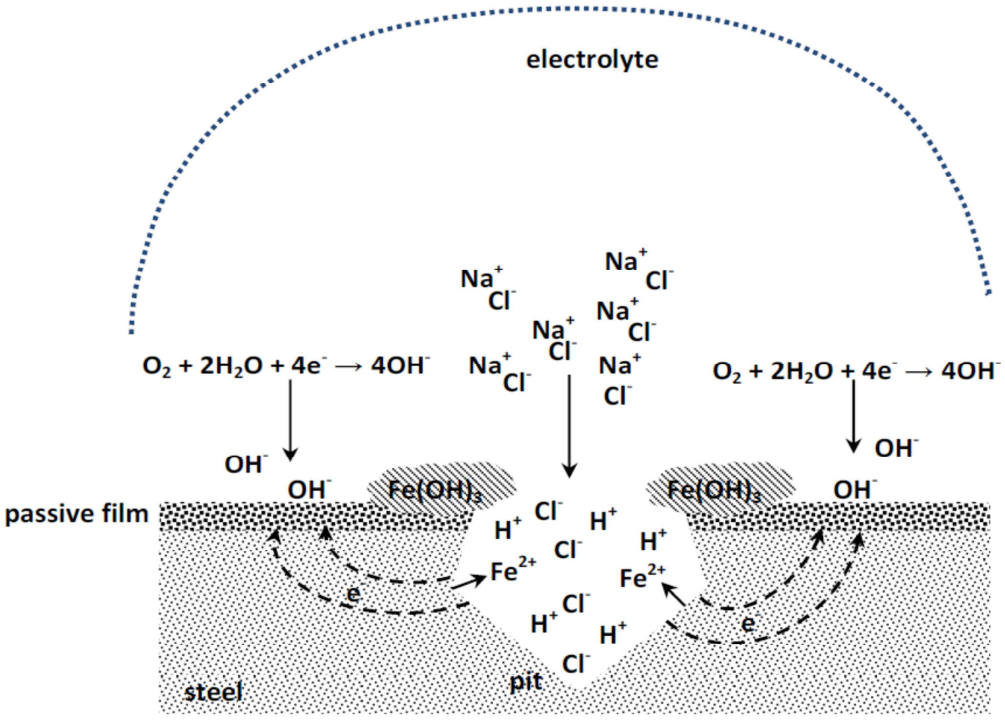

Figure 2.13. *Chloride attack and pitting corrosion on stainless steel. Based on information obtained from [58].*

Electrochemically pitting is detected by a rapid increase in the oxidation current density during the electrochemical corrosion measurement.

Figure 2.14 shows an anodically polarized 316L stainless steel with pits on its surface. The vertical scratches on the optical image were formed during mechanical polishing of the sample.

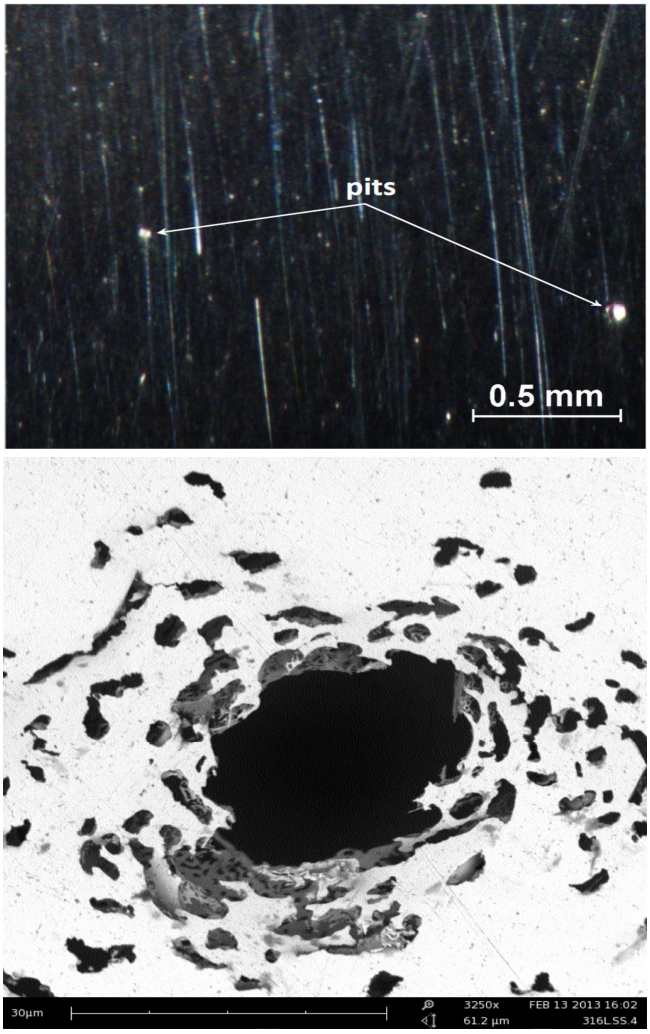

Figure 2.14. *Upper image shows pits formed on a 316L stainless steel coupon after a potentiodynamic polarization in 0.1 M NaCl. Scan rate: 1 mV.s^{-1}. The lower figure shows an SEM image of a pit formed on a 316L stainless steel coupon under the same conditions as above.*

2.3.4. Aqueous corrosion of copper

Copper has good resistance against atmospheric corrosion. It is known that the passive film formed on copper consists of a duplex layer of oxides: an inner layer of cuprous oxide (Cu_2O), and an outer layer of cupric hydroxide ($Cu(OH)_2$) [60]. Despite materials such as steel, in the case of copper, hydrogen evolution does not have a significant role in the corrosion process. Therefore, in non–oxidizing acidic solutions, copper is not corroded. This is attributed to the higher standard redox potential of the Cu/Cu^{2+} system than of the H_2/H^+ couple (Table 2.2). Therefore, corrosion of copper needs a cathodic reaction other than the evolution of H^+ during metal dissolution. However, when oxygen or other oxidants such as chlorides and sulfate ions come into contact with copper, it becomes susceptible to corrosion [61]. Similar to stainless steel

in a solution like sodium chloride the main cathodic reaction during the dissolution of copper will be oxygen reduction which in the case of copper corrosion it is known as a irreversible process. It also has been shown that pitting corrosion of copper occurs with higher intensity and rate in the presence of sulfate ions, which proves the aggressive nature of sulfates in comparison with chloride ions [62].

2.3.4.1. General corrosion

There are many works in the literature regarding the corrosion of copper in aggressive media, particularly in the presence of chloride ions [63–68]. Early investigations into the corrosion of copper in marine environments were performed by Bengough et al. from 1920 to 1924 [69, 70], who proposed that, in neutral chloride solutions, cuprous chloride (CuCl) is the initial corrosion product of copper via Equation 2.36.

$$Cu^{+} + Cl^{-} \rightarrow CuCl \tag{2.36}$$

CuCl is only slightly soluble in sodium chloride and therefore, can react with oxygen and produce cuprous oxide (Cu_2O/cuprite). Cuprite generally oxidized over time to cupric hydroxide ($Cu(OH)_2$), atacamite ($Cu_2(OH)_3Cl$) or malachite ($CuCO_3.Cu(OH)_2$). According to Bengough et al., four patina layers can be formed on a metallic copper exposed to a chloride–containing solution. These layers are shown in Figure 2.15. The layers of corrosion products formed are (from inner to outer): cuprous chloride, cuprous oxide, cupric hydroxide or oxide, and finally atacamite or malachite, depending on the form of the previous layer.

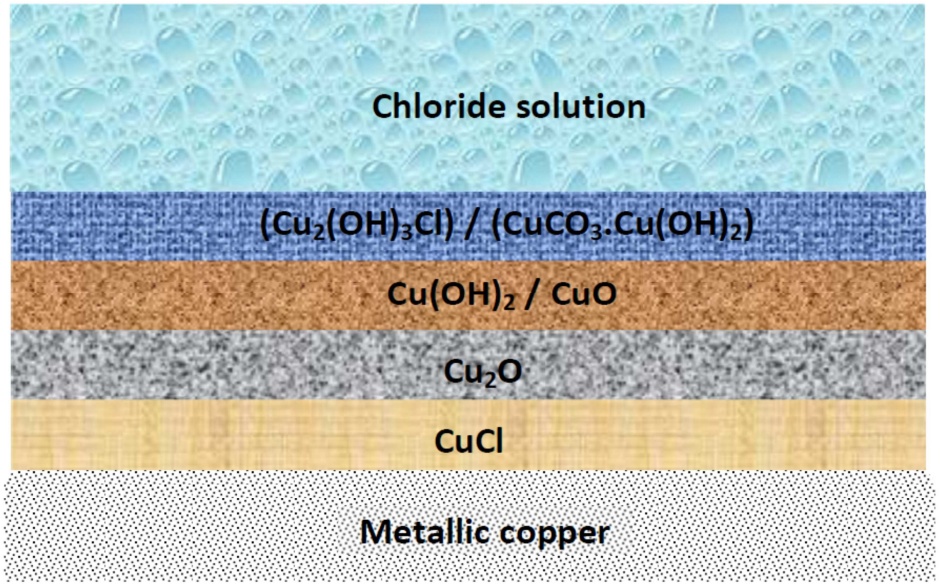

Figure 2.15. *Scheme of patina layers formed on a copper specimen in seawater, as suggested by Bengough et al. [70].*

Later, Lee and Noble [71] observed that cuprous chloride forms complexes of cupric chloride ($CuCl_2^-$) in the form of $CuCl_3^{2-}$ and $CuCl_4^{3-}$ when the chloride concentration becomes higher than 0.7–1 mol.dm^{-3} (Eq. 2.37).

$$Cu^+ + 2Cl^- \rightleftharpoons CuCl_2^- + Cl^- \rightleftharpoons CuCl_3^{2-} + Cl^- \rightleftharpoons CuCl_4^{3-} \qquad (2.37)$$

It is known that cuprite forms on the copper surface as a precipitation [72] according to Equation 2.38:

$$2CuCl_2^- + 2OH^- \rightleftharpoons Cu_2O + H_2O + 4Cl^- \qquad (2.38)$$

The stability of the formed cuprite is depended on the concentration of chloride ions [72].

2.3.4.2. Electrodissolution

Later studies revealed that in chloride containing solutions copper dissolves as Cu^+ at E_{corr}. Cu^{2+} is formed by irreversible oxidation of Cu^+ in presence of oxygen as follows [73]:

$$4Cu^+ + O_2 + 2H_2O \rightarrow 4Cu^{2+} + 4OH^- \qquad (2.39)$$

The Cu^{2+} formed through Eq. 2.39 can also be reduced by chloride ions via an irreversible reaction [73]:

$$Cu^{2+} + 2Cl^- \rightarrow CuCl_2^- + e^- \qquad (2.40)$$

However, added to these equations there are also three other reversible models suggested for the anodic dissolution of copper in the presence of chlorides. The main difference between these models is the form of the initial reaction.

$$Cu + 2Cl^- \rightleftharpoons CuCl_2^- + e^- \qquad (2.41)$$

$$\begin{aligned} Cu &\rightleftharpoons Cu^+ + e^- \\ Cu^+ + 2Cl^- &\rightleftharpoons CuCl_2^- \end{aligned} \qquad (2.42)$$

$$\begin{aligned} Cu + Cl^- &\rightleftharpoons CuCl + e^- \\ CuCl + Cl^- &\rightleftharpoons CuCl_2^- \end{aligned} \qquad (2.43)$$

The reactions denoted in Equations 2.41 and 2.42 show the direct formation of cupric chloride from copper [74–80], whilst the reaction shown in Equation 2.43 represents the dissolution of copper to cuprous chloride in the initial step [81–84].

Analogous to the behavior in stainless steels, a thin protective oxide film is formed on copper in open air. Therefore, the corrosion process of copper initiates with breakdown of this oxide film, which is a well–known phenomenon that occurs rapidly in the presence of oxidants such as chloride ions. However, there are significant differences between the corrosion mechanisms of copper and steel. The anodic partial reaction during the dissolution of steel is usually considered as a pure charge transfer reaction and the cathodic part as a mixed charge, mass transfer controlled process (Section 4.1). In the case of copper, the anodic reversible reactions shown above are assumed to be under mixed charge transfer and mass transfer controlled and the cathodic part, depending on the oxygen concentration, is described as a mass transfer or kinetically limited reaction [85].

The anodic or cathodic reaction may be diffusion controlled when the electron transfer step is faster than diffusion. However, a charge transfer controlled reaction follows Tafel behavior. In corrosion studies when the cathodic current density in a *i–E* plot is vertical it means that the process is independent of the applied potential and

therefore, it is mass transfer controlled. In order to maintain the reaction rate, diffusion of the reacting species (for example oxygen) through the electrolyte becomes important, then the cathodic reaction may be under mixed charge–mass transfer control [86].

Unlike stainless steel, the thick patina layer that forms on copper during its corrosion (Section 5.3.3) means that observation of pits on corroded copper is only possible after removal of the corrosion products. This can be achieved by ultrasonic cleaning of the sample after reducing the corroded surface [62].

Bibliography

[1] J. Gordon Parr, A. Hanson, An Introduction to Stainless Steel. American Society for Metals, Metals Park, Ohio (1965).

[2] K. H. Lo, C. H. Shek, J. K. L. Lai, Mat. Sci. Eng. R., 65 (2009) 39–104.

[3] J. R. Davis, Stainless Steels, ASM Specialty Handbook, ASM International, Materials park, Ohio (1994).

[4] H. M. Cobb, The History of Stainless Steel. ASM International, Materials Park, Ohio (2010).

[5] S. K. Naha, International Year of Chemistry 2011, Science Reporter (2011).

[6] N. R. Baddoo, J. Constr. Steel Res. 64 (2008) 1199–1206.

[7] www.steel.org, (last visit on 10.03.2013).

[8] P. J. Blau, K. G. Budinski, Wear 225–229, Part 2 (1999) 1159–1170.

[9] www.cencenelec.eu/standards, (last visit on 10.03.2013).

[10] L. Selwyn, Metals and Corrosion, A Handbook For the Conservation Professional. Canadian Conservation Institute, Ottawa (2004).

[11] G. George, H. Shaikh, S. Ningshen, U. K. Mudali, Corrosion of Austenitic Stainless Steel: Mechanism, Mitigation and Monitoring, H. S. Khatak, B. Raj (Eds.), Alpha Science International Ltd., Pangbourne (2002) p. 1–53.

[12] J. K. L. Lai, C. H. Shek, K. H. Lo, Stainless Steels: An Introduction and Their Recent Developments (2012) (eBook).

[13] D. A. Scott, Copper and Bronze in Art, Corrosion, Colorants, Conservation. The Getty Conservation Institute, Los Angeles (2002).

[14] K. F. Khaled, Mater. Chem. Phys. 125 (2011) 427–433.

[15] L. Nunez, E. Reguera, F. Corvo, E. Gonzalez, C. Vazquez, Corros. Sci. 47 (2005) 461–484.

[16] N. Anyadike, Copper, A Material for the New Millennium, Woodhead Publishing, Cambridge (2002).

[17] H. Leidheiser Jr, The Corrosion of Copper, Tin and their Alloys, The Corrosion Monograph Series. John Wiley and Sons, New York (1971).

[18] J. R. Davis, Copper and Copper Alloys. ASM Specialty Handbook, ASM International, Materials Park, Ohio (2001).

[19] H. Lipowsky, E. Arpaci, Copper in the Automotive Industry. Wiley–VCH Verlag GmbH & Co., Weinheim (2007).

[20] H. H. Strehblow, Corrosion and Environmental Degradation, Vol. 1, M. Schutze (Eds.), Materials Science and Technology Series, Weinheim (2000) p. 1–66.

[21] D. Landolt, Corrosion Mechanisms in Theory and Practice, P. Marcus, J. Oudar (Eds.), Dekker, New York (1995) p. 1–18.

[22] G. Gedge, J. Constr. Steel Res. 64 (2008) 1194–1198.

[23] D. D. Macdonald, M. C. H. McKubre, Electrochemical Corrosion Testing, F. Mansfeld, U. Bertocci (Eds.), American Society for Testing and Materials, Philadelphia (1981) p. 110–149.

[24] A. Groysman, Corrosion for Everybody. Springer Dordrecht Heidelberg London New York (2010).

[25] C. Wagner, W. Traud, Z. Elektrochem. 44 (1938) 391–402.

[26] D. C. Graham, Chem. Rev., 41 (1947) 441–501.

[27] B. J. Little, P. A. Wagner, Modern Aspects of Electrochemistry, Vol. 1, J. O'M. Bockris, B. E. Conway, R. E. White (Eds.), Butterworths, London (1954) p. 233–239.

[28] P. Delahay, Double Layer and Electrode Kinetics, Wiley–Interscience, New York (1965).

[29] D. M. Mohilner, Electroanalytical Chemistry, Vol. 1, A. J. Bard (Eds.), Dekker, New York (1966) p. 241–409.

[30] D. E. Smith, AC Polarography and Related Techniques: Theory and Practice, A. J. Bard (Eds.), Dekker, New York (1966) p. 1–157.

[31] D. E. Smith, Electroanalytical Chemistry, Vol. 1, A. J. Bard (Eds.), Dekker, New York (1966) p. 1–155.

[32] A. M. Bond, Modern Polarographic Techniques in Analytical Chemistry, Dekker, New York (1980).

[33] A. J. Bard, L. R. Faulkner, Electrochemical Methods, Wiley, New York (1980).

[34] E. Horwood, Instrumental Methods in Electrochemistry, Southampton Electrochemistry Group, Chichester (1985).

[35] Z. Galus, Fundamentals of Electrochemical Analysis, Ellis Horwood, New York, Polish Scientific Publishers PWN, Warsaw (1994).

[36] M. E. Orazem, B. Tribollet, Electrochemical Impedance Spectroscopy, the Electrochemical Society Series, Wiley, New Jersey (2008).

[37] D. D. Macdonald, Electrochim Acta 51 (2006) 1376–1388.

[38] D. D. Macdonald, Electrochim Acta 35 (1990) 1509–1525.

[39] J. Mathiyarasu, N. Palaniswamy, V. S. Muralidharan, J. Chem. Sci. 111 (1999) 377–386.

[40] M. Georgiadou, R. Alkire, J. Appl. Electrochem. 28 (1998) 127–134.

[41] F. Mansfled, H. Shih, H. Greene, C. H. Tsai, Electrochemical Impedance, Analysis and Interpretation, J. R. Scully, D. C. Silverman, M. W. Kendig (Eds.), American Society for Testing and Materials (ASTM), Philadelphia (1993) p. 37–53.

[42] R. Cottis, S. Turgoose, Corrosion Testing Made Easy: Electrochemical Impedance and Noise. NACE International, Houston (1999).

[43] P. I. Dolin, B. V. Ershler, Acta Physicochim, URSS 13 (1940) 747–779.

[44] J. E. B. Randles, Discuss. Faraday Soc. 1 (1947) 11–19.

[45] J. Keir, Philos. Trans. Royal Soc. London, 80 (1790) 359–384.

[46] N. Sato, G. Okamoto, Electrochemical Passivation of Metals in Comprehensive Treatise of Electrochemistry, Vol. 4, J. O'M. Bockris, R. E. White (Eds.), Plenum Publishing Corporation, New York, London (1981) p. 193–295.

[47] R. D. Moser, P. M. Singh, L. F. Kahn, K. E. Kurtis, Corros. Sci. 57 (2012) 241–253.

[48] M. J. M. Portero, J. G. Antón, J. L. Guiñón, V. P. Herranz, Corros. Sci. 51 (2009) 807–819.

[49] H. Kaesche, Mettalic Corrosion, Principles of Physical Chemistry and Current Problems (English translation of Die Korrosion der Metalle, 2nd ed.). National Association of Corrosion Engineers, Houston, Texas (1985).

[50] N. Homazava, A. Ulrich, M. Trottmann, U. Krahenbuhl, J. Anal. Atom. Spectrom. 22 (2007) 1122–1130.

[51] H. Ashassi–Sorkhabi, E. Asghari, Corros. Sci. 51 (2009) 1828–1835.

[52] J. W. Oldfield, Galvanic Corrosion, H. P. Hack (Eds.), American Society for Testing and Materials, Philadelphia (1988) p. 5–22.

[53] Y. P. Kim, M. Fregonese, H. Mazille, D. Feron, G. Santarini, Corros. Sci. 48 (2006) 3945–3959.

[54] N. Le Bozec, C. Compere, M. L'Her, A. Laouenan, D. Costa, P. Marcus, Corros. Sci. 43(4) (2001) 765–786.

[55] R. E. Weyers, Techniques to Assess the Corrosion Activity of Steel Reinforced Concrete Structures, N. S. Berke, E. Escalante, C. K. Nmai, D. Whiting (Eds.), American Society for Testing and Materials (ASTM), Baltimore (1996) p. 3–22.

[56] G. A. Ghering, M. H. Peterson, Corrosion 37(4) (1981) 232–242.

[57] K. Jafarzadeh, T. Shahrabi, S. M. M. Hadavi, M. G. Hosseini, J. Mater. Sci. Technol. 23 (2007) 623–628.

[58] Fong–Yuan Ma, Corrosive Effects of Chlorides on Metals, Pitting Corrosion, N. Bensalah (Eds.), ISBN: 978-953-51-0275-5, InTech (2012) p. 7–178.

[59] A. Pardo, M. C. Merino, A. E. Coy, F. Viejo, R. Arrabal, E. Matykins, Corros. Sci. 50 (2008) 1796–1806.

[60] H. Strehblow, B. Titze, Electrochim. Acta. 25 (1980) 839–850.

[61] M. Finsgar, I. Milosev, Corros. Sci. 52 (2010) 2737–2749.

[62] G. Mankowiski, J. P. Duthil, A. Giusti, Corros. Sci. 39(1) (1997) 27–42.

[63] A. M. Alfantazi, T. M. Ahmed, D. Tromans, Mater. Des. 30 (2009) 2425–2430.

[64] S. M. Milic, M. M. Antonijevic, Corros. Sci. 51 (2009) 28–34.

[65] G. Mankowski, J. P. Duthil, A. Giusti, Corros. Sci. 39 (1997) 27–42.

[66] A. L. Bacarella, J. C. Griess, J. Electrochem. Soc. 120 (1973) 459–465.

[67] D. Strasvetsky, O. Khaselev, M. Auinat, Y. Ein-Eli, Electrochim. Acta. 51 (2006) 5660–5668.

[68] M. Scendo, Corros. Sci. 50 (2008) 2070–2077.

[69] G. D. Bengough, R. M. Jones, R. Pirret, J. I. Met. 23 (1920) 65–158.

[70] G. D. Bengough, R. May, J. I. Met. 32 (1924) 81–269.

[71] H. P. Lee, K. Noble, J. Electrochem. Sco. 133 (1986) 2035–2043.

[72] F. King, L. Ahonen, C. Taxen, U. Viorinen, L. Werme, Copper Corrosion under Expected Conditions in a Deep Geologic Repository, Posiva Report, Helsinki, Finland (2002).

[73] G. Kear, B. D. Barker, F. C. Walsh, Corros. Sci. 46 (2004) 109–135.

[74] F. King, M. J. Quin, C. D. Litke, J. Electroanal. Chem. 385 (1995) 45–55.

[75] R. J. K. Wood, S. A. Fry, J. Fluids Eng. 112 (1990) 218–224.

[76] C. Deslouis, B. Tribollet, G. Mengoli, M. Musiani, J. Appl. Electrochem. 18 (1988) 374–383.

[77] H. P. Lee, K. Nobe, J. Electrochem. Soc. 133 (1986) 2035–2043.

[78] M. Sanchez, J. Gamby, H. Perrot, D. Rose, V. Vivier, Electrochem. Comm. 12 (2010) 1230–1232.

[79] G. Kear, F. C. Walsh, D. B. Barker, K. S. Stokes, Electrochemical Corrosion Characteristics of Copper in Filtered and Artificial Seawater as a Function of Mass Transfer Conditions, EUROCORR 2000 Conference, Institute of Corrosion. Leighton Buzzard, UK, (2000).

[80] D. Wagner, H. Peimemann, H. Siedlarek, S. A. Campbell, N. Campbell, F. C. Walsh, Developments in Marine Corrosion. The Royal Society of Chemistry, Cambridge, UK (1998) 103–118.

[81] F. B. Mansfeld, G. Liu, H. Xiao, C. H. Tsai, B. J. Little, Corros. Sci. 36 (1994) 2063–2095.

[82] W. H. Smyrl, J. Electrochem. Soc. 132 (1985) 1555–1562.

[83] J. O. M. Bockris, D. Drazic, Electrochim. Acta. 7 (1962) 293–313.

[84] L. Caceres, T. Vargas, L. Herrera, Corros. Sci. 49 (2007) 3168–3184.

[85] F. King, C. D. Litke, M. J. Quinn, D. M. Leneveu, Corros. Sci. 37(5) (1995) 833–851.

[86] R. G. Kelly, J. R. Scully, D. W. Shoesmith, R. G. Buchheit, Electrochemical Techniques in Corrosion Science and Engineering, Marcel Dekker Inc. New York (2003).

Chapter 3

Comparative investigation of 304L stainless steel using a microcapillary cell and a conventional setup

3.1. Introduction

In principle every electrochemical reaction, which occurs at a macro scale electrode, can also occur on a micro scale. However, it is well known that there are similarities and differences between macro and micro scale electrochemical processes. Charge transfer reactions that occur at the surface–electrolyte interface are identical in both macro and micro systems [1]. But in the case of a diffusion layer, the dimension of the solid surface becomes important. In micro systems higher convergent diffusions occur due to their high limiting current densities [2]. Increasing the mass transport in micro systems is one of the most important differences between the two systems. By decreasing the surface area in micro systems the double layer capacitance is reduced. In addition micro systems obviously decrease the magnitude of the current passed [3], whereby small currents in the range of a few nA to some pA can be measured. Therefore, the size of the working electrode and the rate of mass transfer processes that occur at the surface of the working electrode are two key factors that control the kinetics of the microelectrochemical reactions in micro systems. According to the theory the diffusion limited current on a micro scale increases with the electrode radius while the diffusion limited current density decreases linearly with the radius [4, 5].

The objective of this chapter is to study the ability of a microcapillary electrochemical technique in the surface investigation of 304L stainless steel and more specifically to make a comparison between micro scale and conventional large scale surface analyses using voltammetric methods. This chapter also consists of the corrosion study of a 304L stainless steel sample on micro scale aerated conditions using a modified microcapillary cell.

3.2. Experimental

3.2.1. Specimens, chemicals and surface preparation

Analytical grade NaCl was purchased from Fluka. Both micro and large scale measurements were performed on 304L stainless steel with the following chemical composition (wt. %): Cr: 17.65, Ni: 8.59, Mn: 1.75, Si: 0.41, C: 0.017, P: 0.032 and S: 0.005. The steel samples (coupons with a diameter of 12.5 mm and thickness of 2 mm) were mechanically grounded with silicon carbide paper down to 600 grit and then polished with a polishing cloth (MicroCloth, Buehler) using alumina powder (<0.5 μm). They were then washed with distilled water and rinsed ultrasonically in ethanol for 5 min.

3.2.2. Electrochemical setups

The micro scale electrochemical measurements were performed using a homemade microcapillary cell (Figure 3.1) attached to an Autolab Eco Chemiepotentiostat (PGSTAT 10). The setup is based on a common three–electrode system containing a thin platinum wire as counter electrode, and a sealed microcapillary with a silicone gasket and with a ground tip diameter of 150 μm which touches only a small part of the solid sample placed on a platinum plate and forms the working electrode and a saturated Ag/AgCl/KCl reference electrode (In 25 ^{o}C the standard electrode potential of this reference electrode against standard hydrogen electrode (SHE) is about 0.230 V ± 10 mV). The platinum plate itself is attached to a fiberglass plate with a number of holes and plastic screws, which makes it possible to fix different samples with different sizes on it before measurement (not shown in Figure 3.1). To minimize the Ohmic resistance during the measurement the counter electrode (here platinum wire) was placed near the tip of the microcapillary. The microcapillaries were obtained through the procedure described in Section 1.3.

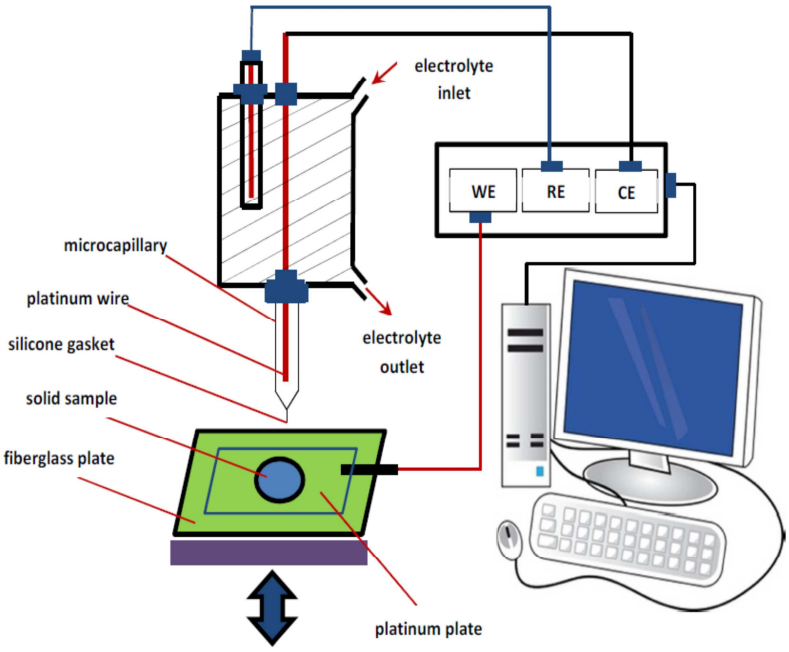

Figure 3.1. *Schematic drawing of the setup of the capillary–based droplet cell.*

The large scale electrochemical measurements were performed using the same potentiostat in a three–electrode cell with a saturated Ag/AgCl/KCl reference electrode and a platinum plate as auxiliary electrode.

Scanning electron images of the surface were taken using a Phenom–FEI electron microscope. Detailed information about scanning electron microscopy (SEM) can be found in [6].

3.3. Results and discussion

3.3.1. Comparison of localized and conventional electrochemical measurements

Figure 3.2 shows the potentiodynamic polarization curves of the stainless steel sample after 6 continuous polarizations obtained by the micro scale (a) and the conventional macro scale experiments (b). In addition the variation of E_{corr} versus the number of polarizations performed for both micro and macro measurements is provided. Both micro and macro scale E_{corr} measurements were repeated at least three times and their standard deviation was calculated. Each series of the micro measurements was performed on one specific spot of the sample.

The micro scale potentiodynamic polarization curves show that the corrosion potential of the steel shifts towards nobler potentials after the 2nd and the 3rd polarization but decreases after the 4th polarizations (Figure 3.2a).

The macro scale graphs show that E_{corr} decreases versus the number of the potentiodynamic polarizations (Figure 3.2b).

Although the E_{corr} shift in both macro and micro scale measurements is not significant (< 0.1 V), a comparison of the cathodic and the anodic parts of the obtained plots can reveal the different formed corrosion environments with different corrosion procedures under two different setups/ electrochemical cells.

The micro scale polarization curves show that the cathodic current density does not change significantly during the potentiodynamic polarizations. This means that potentiodynamic polarization of the surface under the microcapillary does not change the oxygen concentration in the trapped measurement area and therefore, the oxygen reduction rate remains almost constant. The constant oxygen concentration is attributed to the transport of oxygen through the silicone gasket under the microcapillary. As has been discussed in Section 1.5.2.5, due to the high permeation of oxygen through the silicone membrane the air–silicone–electrolyte interface can be considered also as only air–electrolyte interface. Therefore, the diffusion of oxygen into the trapped surface during the electrochemical measurement effects the cathodic reaction which is known as oxygen reduction reaction (Eq. 2.26, 2.27). This is the main reason that one needs to consider the influence of the oxygen transport from the surrounding area of the capillary on corrosion of metals/alloys when the microcapillary technique is used.

In the micro scale measurements, unlike the cathodic parts of the Tafel plots, the anodic current density of steel decreases after each potentiodynamic polarization. In Figure 3.2a due to the presence of enough oxygen in the micro cell the corrosion process occurs with greater intensity. After the first polarization the anodic current density decreases as the surface is covered by the corrosion products (mainly $Fe(OH)_3$) and this decrease in the anodic/passive current density is continuously observed until the 6th polarization.

In the case of the large scale measurements, the polarization graphs reveal that the cathodic current density of the graphs decreases after each polarization and this shifts the E_{corr} of steel towards less noble potentials. Moreover, the anodic parts of these graphs (passive current density) increases continuously after each polarization.

Based on the obtained information through the potentiodynamic polarization curves measured by the large scale steel electrodes it can be concluded that the cathodic current density of steel during the potentiodynamic polarization process decreases

after each polarization because less oxygen gets reduced over the steel surface (Eq. 2.26 and 2.27). This means every potentiodynamic polarization performed on the surface makes the procedure of oxygen reduction more difficult. This is directly related to the effect of the potentiodynamic polarization on the diffusion layer of the surface. Although in the large scale measurements after each polarization scan the generated gas bubbles have been removed from the surface of the electrode by gently stirring the solution, during each potentiodynamic polarization part of the formed gas bubbles remain in the metal–electrolyte interface and block the pathway of oxygen reduction. This decreases the rate of the oxygen reduction reaction. The passive current density however continuously increases.

Finally Figure 3.2 depicts that E_{pit} of steel is higher for when it is measured in micro scale level. Similar results have been reported by Böhni et al. [7]. These authors have studied the pitting potentials of stainless steel measured by microelectrodes with different diameters from 50 μm to 1000 μm (large scale) and observed that the pitting potentials of steel decreases with increasing surface area because larger surface area exposes more weak points to the electrolyte and therefore, pitting can occur at lower potentials. According to Schultze and Bressel [8], the charge transfer reactions and reaction mechanisms in solution in both micro and macro systems are the same. In spite of this, some differences appear when the applied potential or current focuses on a micro point. More specifically, the difference arises when a random phenomenon such as pit formation becomes dominant [8, 9]. Therefore, the difference in the corrosion potentials, the pitting potentials and also in the current densities can be concluded as the result of the decrease in the exposed surface area.

In Figure 3.2a, the E_{pit} values measured by the micro cell do not show any significant change after 6 polarizations. This potential is detectable around 0.7 V after each scan. In the macro scale measurements however, E_{pit} of the steel changes after each polarization. According to our measurements this change in the E_{pit} values in the large scale measurements is not regular and may increase or decrease after each potentiodynamic polarization.

Moreover, comparison of the calculated standard deviations of the E_{corr} variations of steel versus number of the potentiodynamic polarizations on micro and macro scale levels reveals that the micro scale plots have a lower reproducibility than the large scale disc electrode plots. The main reason for this is the effect of oxygen of the surrounding area of the gasket on the corrosion performance of the trapped area under the microcapillary. This means that in order to obtain proper electrochemical data using microcapillary technique one needs to consider the transferred oxygen gradient

through the silicone membrane and perform the measurements under controlled/ aerated environment.

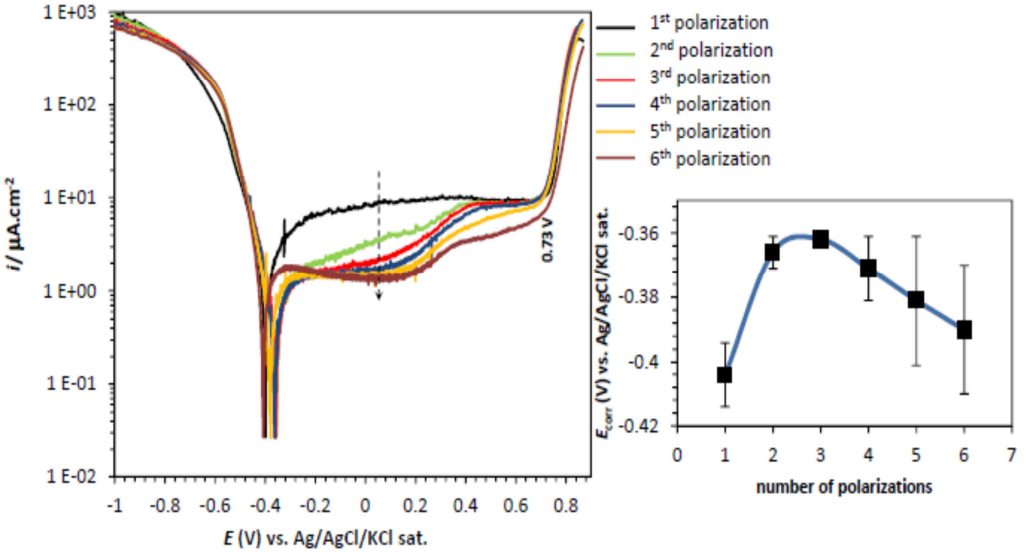

(a)

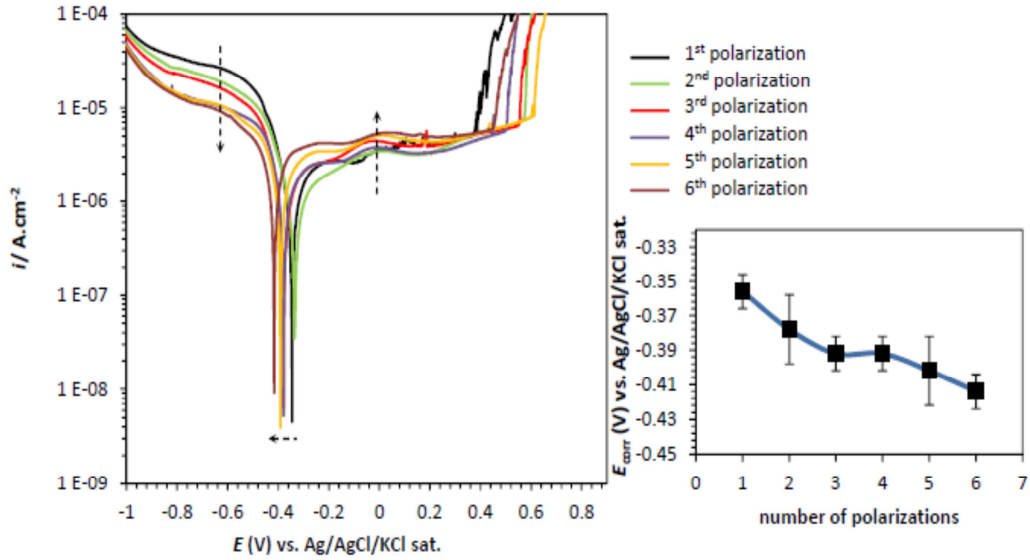

(b)

Figure 3.2. *Tafel plots of the 304L stainless steel sample in a 0.1 M NaCl solution (6 polarizations) with the variation of the E_{corr} of steel versus the number of potentiodynamic polarization scans. (a) micro scale by a microcapillary with a tip diameter of 150 µm. (b) large scale. (scan rate: 1 mV.s^{-1}).*

In order to decrease the effect of the oxygen diffusion through the silicone gasket, we suggest the use of a nitrogen gas shield around the microcapillary tip. As it is expected

it decreases the amount of the oxygen diffusion through the silicone gasket and decreases the total concentration of the oxygen inside the measurement area compared to the bare microcapillary. Figure 3.3 is the schematic view of the modified microcapillary setup which we have used to study the effect of nitrogen shield over the corrosion of steel.

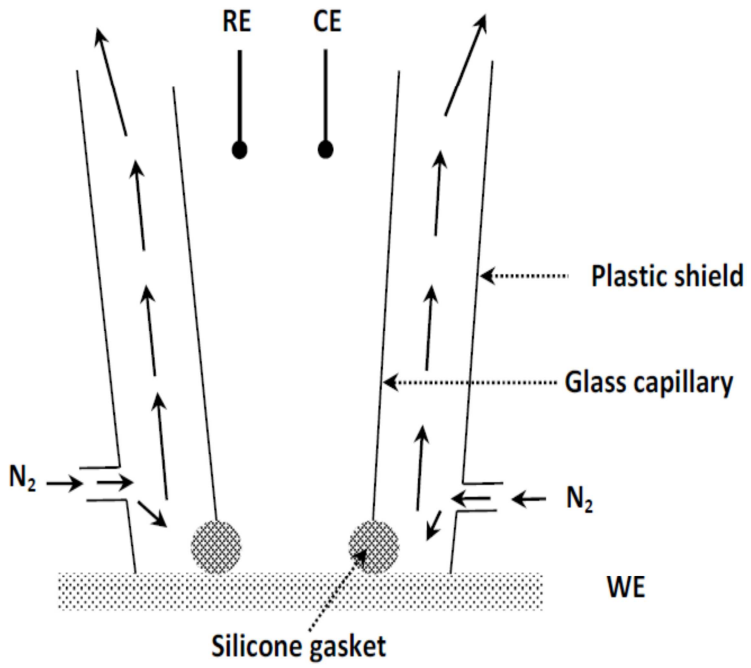

***Figure 3.3**. Scheme of a modified glass capillary covered by a nitrogen gas shield.*

A stream of nitrogen was flushed through the plastic shield during the potentiodynamic measurements and the effect of the surrounding aeration on the electrochemical response of steel especially on the oxygen reduction rate was investigated. The results are shown in Figure 3.4.

The latter shows that in comparison to the potentiodynamic curves measured by the non–modified capillary the total current density drops after application of the nitrogen gas shield. After the first polarization both the cathodic and the anodic current densities decrease and E_{corr} shifts towards less noble potentials compared to the plot measured under deaerated conditions. In Figure 3.4 less oxygen reduction occurs which reduces significantly the amount of corrosion under the capillary. Furthermore, similar to the large scale measurements, here also after each potentiodynamic polarization scan E_{corr} decreases. Comparison of the standard deviations of the micro scale measurements calculated for the modified and the non–modified setups (Figures

3.2a and 3.4) shows that the measurements performed under the aerated environment have better reproducibility than the non–aerated measurements.

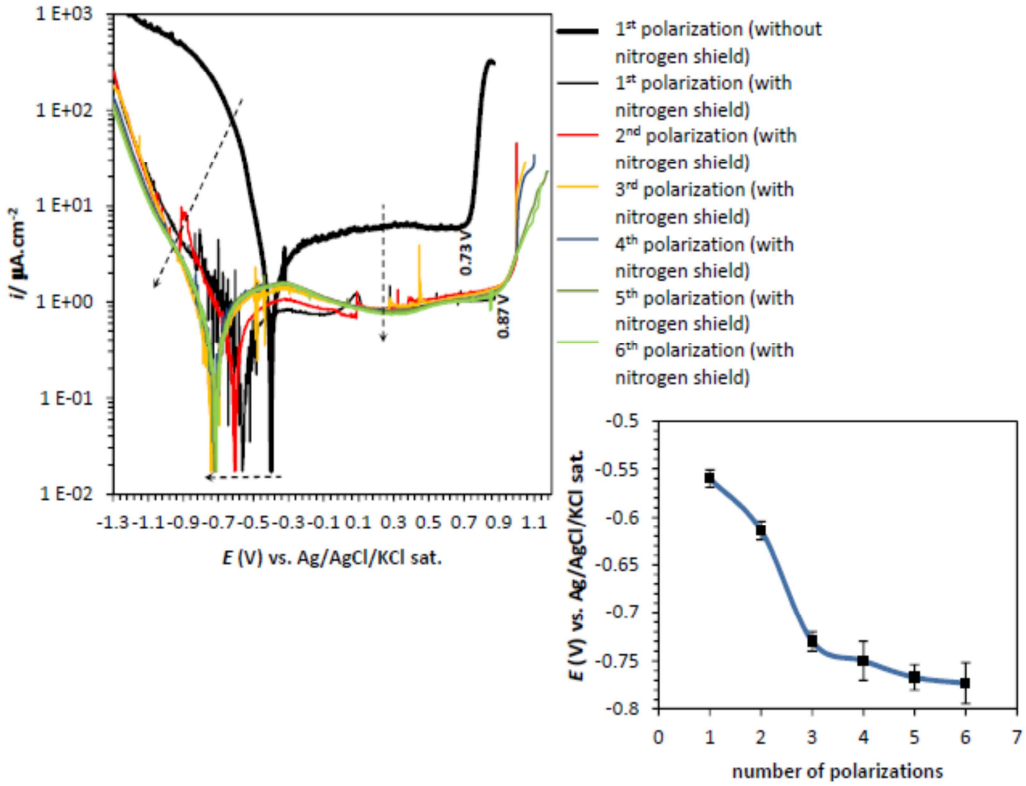

Figure 3.4. *Tafel plots of the 304L stainless steel sample in a 0.1 M NaCl solution (6 polarizations) measured under a microcapillary with a tip diameter of 150 µm with and without nitrogen gas shield with the variation of the E_{corr} of steel versus the number of potentiodynamic polarization scans under aerated conditions. (scan rate: 1 mV.s^{-1}).*

These graphs also reveal that in presence of lower oxygen concentrations the pitting corrosion of steel appears at greater positive potentials which shows the higher resistance of steel against pitting corrosion when less oxygen is available.

Figure 3.5 shows the SEM image of a corroded area of the steel sample after 6 potentiodynamic polarization scans under a modified microcapillary with nitrogen shielding.

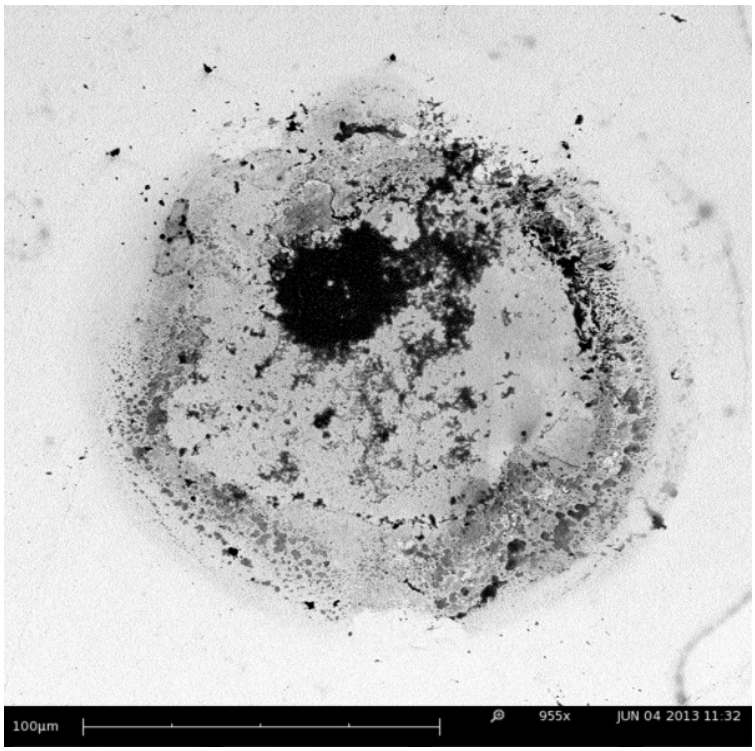

Figure 3.5. *Scanning electron image of the 304L stainless steel sample after 6 polarizations by a microcapillary with nitrogen shield and a tip diameter of 150 µm using linear sweep voltammetry in a 0.1 M NaCl solution. Scan rate: 1 mV.s^{-1}.*

3.4. Conclusions

Capability of the microcapillary technique in electrochemical investigation of stainless steel in sodium chloride solution was investigated and the results were compared with the electrochemical responses of steel obtained by a conventional large scale disc electrode. The results revealed that different corrosion environment is created by the microcapillary technique compared to the large scale disc electrode immersed in the electrolyte. Despite several advantages of the microcapillary technique the micro corrosion cell constructed under the microcapillary with a silicone gasket is strongly under effect of the surrounding area of the silicone membrane. Due to the diffusion of oxygen from the surrounding area of the silicone gasket into the measurement area, the cathodic current density of steel which is produced mainly through the reduction of oxygen does not change after 6 continuously potentiodynamic polarization cycles. While after each polarization the passive current density under the capillary decreases. When a large scale disc electrode was polarized the rate of oxygen reduction decreases after each polarization and unlike the micro measurements the anodic current density increases when more polarizations are applied over the steel surface.

An inert gas shielding was suggested to control the oxygen transfer through the silicone gasket in the micro cell. The results showed that the current density of steel drops when the potentiodynamic polarization of steel is performed under aerated environments. This is attributed to the lower oxygen concentration under the microcapillary than non–modified microcapillary setup.

Bibliography

[1] J. W. Schultze, A. Bressel, Electrochim. Acta 47 (2001) 3–21.

[2] J. C. Eklund, A. M. Bond, J. A. Alden, R. G. Compton, Adv. Phys. Org. Chem. 32 (1999) 1–120.

[3] N.V. Rees, R.G. Compton, Russ. J. Electrochem. 44 (2008) 368–389.

[4] R. M. Wightman, Electroanalytical Chemistry, Vol. 15, A. J. Bard (Eds.), Marcel Dekker, New York, Basel (1989) p. 267–353.

[5] J. Heinze, Angewandte chemie, Int. Ed. Engl. 32 (1993) 1268–1288.

[6] D. F. Blake, Instrumental Surface Analysis of Geologic Materials, D. L. Perry (Eds.), VCH Publishers, Inc. New York (1990) p. 11–43.

[7] H. Böhni, T. Suter, A. Schreyer, Electrochim. Acta 40 (1995) 1361–1368.

[8] J.W. Schultze, A. Bressel, Electrochim. Acta 47 (2001) 3–21.

[9] J.W. Schultze, V. Tsakova, Electrochim. Acta 44 (1999) 3605–3627.

Chapter 4
Cathodic polarization of 304L and 316L stainless steels in NaCl solution

This study investigates the effect of prior cathodic polarization on the electrochemical corrosion of types 304L and 316L stainless steels. The main goal is to examine the effect of prior hydrogen evolution on the electrochemical corrosion responses of steel and to determine any differences in this process between micro and macro scale levels as well as stagnant and dynamic media containing sodium chloride.

The experiments of the first section of this chapter have been performed on grade 316L stainless steel in a 0.1 M NaCl solution and the micro scale measurements of the second section have been performed on 304L stainless steel in a 1 M NaCl solution. Although in this chapter two different grades of austenitic stainless steel have been studied in two different concentration of sodium chloride solution, the mechanisms of the anodic and the cathodic processes are the same for both grades of stainless steel. Here only higher concentration increases the current density compared to a 0.1 M solution. When a modified microcapillary setup with nitrogen shielding is used, in some potentials the measured current drops to a few nano/pico ampere. In this case high electrolyte concentration can increase the measured current (the positive side effect).

4.1. Cathodic polarization of 316L stainless steel large scale disc electrode under static and dynamic conditions

4.1.1. Introduction

Studies regarding flow–accelerated corrosion, also known as flow induced corrosion, and its hydrodynamic properties performed up to now can generally be divided into two major groups. One group has focused on the effects of fluid flow upon the electrochemical responses obtained from corrosion processes [1–16]. The other group has investigated the mechanical properties of a corrosive environment under single–phase and multi–phase flow conditions, different mechanisms and regimes of fluid flow, and their effects on the corrosion of metals and alloys in media containing solid particles. Data obtained through the electrochemical measurements partly support the ideas of the latter group [17–31].

In principle, corrosion under fluid flow is a combination of electrochemical and mechanical phenomena whose combined synergistic effect, in the case of certain metals such as aluminum, is responsible for up to 50 % of the total mass loss [32]. Although it has been reported that fluid flow, especially at high velocities, can remove formed micro galvanic cells, known as corrosion sites from the surface and therefore decrease the corrosion rate, there is no doubt that the increase of the flow velocity below this critical rate increases the corrosion rate [33].

From a mechanical point of view flow accelerated–corrosion usually has three consecutive steps [17]: (1) the formation of metallic ions at the metal surface by the electrochemical oxidation of metal atoms, (2) the diffusional mass transfer of metallic ions formed in the oxide layer–electrolyte interface and (3) the mass transfer of the formed metallic ions from the oxide–electrolyte interface into the bulk electrolyte. Figure 4.1 shows these layers and the diffusion region [2]. In the hydrodynamic layer between the bulk electrolyte and the oxide layer, reactants such as chloride ions move towards the metal oxide layer and formed corrosion products towards the bulk solution. Increasing the mass transfer coefficient and decreasing the diffusion layer can also increase the corrosion rate [34].

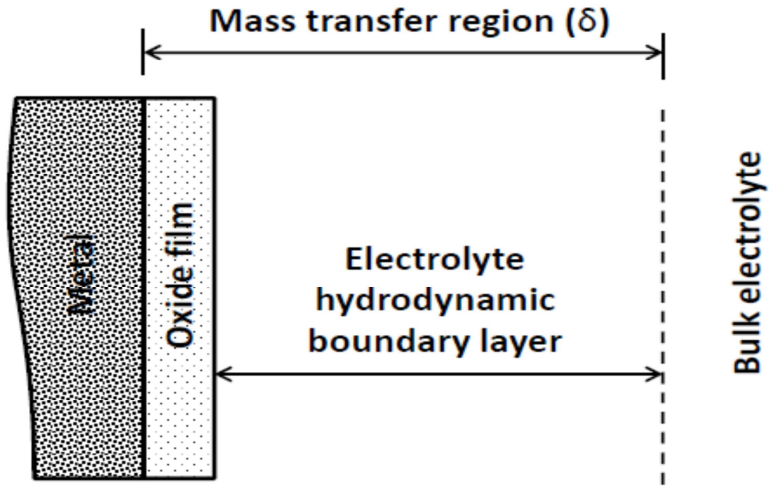

Figure 4.1. *Diffusion layer at the working electrode surface. Based on information obtained from [17].*

In the case of stainless steel, fluid flow and its velocity are significant parameters which always need to be considered especially in pitting corrosion. It has been proven that austenitic steels such as 316 are in lower risk of pitting corrosion at high flow velocities. Velocities greater than 1.5 $m.s^{-1}$ have been suggested in the literature to

avoid pit formation [35, 36]. These high velocities deactivate the pits at the initial stages of their formation.

In chloride containing solutions the breakdown of the oxide film, which may cause pitting corrosion in stainless steel, occurs through chloride attack. Aggressive chloride ions directly attack the weak points of the steel [37]. These attacks may form pits over the surface (Figures 2.10 and 2.13). Literature data have shown that corrosion is a result of the competition between different aggressive ions, such as chlorides and oxygen, which contribute to the destruction and repair of the protective oxide layer, respectively [33]. Chloride ions attack the protective oxide film and cause its breakdown, whilst oxygen simultaneously repairs the formed defects [16]. Therefore, pitting occurs when the rate of destruction of the oxide layer exceeds the rate of repair.

In addition, during the corrosion process of steel the evolution of oxygen and hydrogen gas bubbles on the metal–electrolyte interface is a well–known phenomenon [38]. The latter occurs with greater intensity when the metal is cathodically polarized and hydrogen is introduced into the surface. This process called cathodic polarization can be described as follows.

In a near neutral pH solution, such as sodium chloride, the reduction of hydrogen and water generates hydrogen atoms and molecules. Part of the hydrogen atoms form through Equations 2.30–2.33, which describe the hydrogen evolution mechanisms. However hydrogen atoms are also generated on the surface of steel through the electrochemical reduction of water molecule:

$$H_2O + e^- \rightarrow H_{(ads)} + OH^- \qquad (4.1)$$

The adsorbed hydrogen atoms can combined to H_2 molecules by the chemical reaction mentioned in Equation 2.31 or through the electrochemical reaction with protons (Eq. 2.32) or can electrochemically react with water:

$$H_{(ads)} + H_2O + e^- \rightarrow H_2 + OH^- \qquad (4.2)$$

Part of the hydrogen atoms can be absorbed by the steel surface according to Equation 2.33.

Due to the weak acidic pH of sodium chloride solution, the majority of the hydrogen atoms which are absorbed by the steel are produced by the water reduction process described above [38–41].

The generated hydrogen atoms that penetrate the metal, break down the local oxide film and form micro pits/cracks and metal particles. These pits act as preferential sites during the anodic dissolution of the metal [42]. Therefore, this process can increase the corrosion rate and the passive current density of iron–based alloys [43], promote anodic dissolution [44], decrease the stability of the passive layer [45] and increase the pitting susceptibility [46]. Moreover, hydrogen and chloride ions have a synergistic effect during the corrosion in chloride–containing media [47].

The total anodic current density produced by a cathodically polarized surface in chloride containing solutions is expressed as:

$$i_{(a)} = i_{(0)} + i_{(H^*)} + i_{(Cl^-)} \qquad (4.3)$$

In this equation $i_{(a)}$ is the total oxidation current density of a cathodically polarized surface in the presence of chloride ions, $i_{(0)}$ is the anodic current density of the specimen in a chloride free solution without cathodic polarization, $i_{(H^*)}$ is the anodic current density produced by oxidation of hydrogen diffused into the surface which occurs according to Butler–Volmer equation (Eq. 2.30) and $i_{(Cl^-)}$ indicates the anodic current density increase contributed only by chloride ions.

However, in practice the total anodic current density of a cathodically polarized surface in the presence of chloride ions has higher values than $i_{(a)}$ represented in Equation 4.3. This indicates that there is a synergistic effect between hydrogen and chloride ions on the anodic current density. Therefore, the total anodic current density of a cathodically polarized surface in the presence of chlorides must be expressed as:

$$i_{(a)} = i_{(0)} + i_{(H^*)} + i_{(Cl^-)} + i_{(H^*,Cl^-)} \qquad (4.4)$$

In this equation the last term indicates the anodic current density produced by the synergistic effect of hydrogen and chloride ions [47].

The cathodic polarization process called also cathodic corrosion, has been recently reported by Rodriguez et al. [48] as a simple technique for producing metal nanoparticles.

This study investigates the effect of prior cathodic polarization on the electrochemical corrosion of 316L stainless steel under static and under two different flow conditions. The main goal is to examine the effect of prior hydrogen evolution on the electrochemical corrosion response of steel and to determine any differences in this

process between stagnant and dynamic media with different flow regimes containing sodium chloride.

4.1.2. Experimental

4.1.2.1. Specimens, chemicals and surface preparation

A 0.1 M sodium chloride solution was prepared using analytical grade NaCl powder (Fluka). All the experiments in this work were performed on 316L stainless steel coupons with the following chemical composition (in wt. %): C 0.024, Si 0.46, Mn 1.22, P 0.038, S 0.0048, Ni 9.69, Cr 16.45, Mo 1.95, Cu 0.35, Al 0.020. All coupons are 12.5 mm in diameter and 2 mm thick. They were ground with 600 grit silicon carbide paper and then polished with a polishing cloth (MicroCloth, Buehler) using 1.0 μm and then 0.5 μm alumina particles. Finally, the samples were washed with distilled water and acetone and rinsed ultrasonically in ethanol for five minutes. To apply similar experimental conditions on the samples, all measurements were performed within one hour of polishing.

4.1.2.2. Cell design and electrochemical measurements

In this study we constructed two different dynamic condition systems. One contains a rotating disc electrode (RDE) and the other one is a homemade flow cell setup. The rotating disc electrode setup (CTV101–Radiometer Copenhagen, France), with a maximum 5000 rotations per minute, was immersed in a fiberglass cell with 100 mL electrolyte and for every measurement a proper rotation rate was applied through the digital speed controller. The homemade flow cell (Figure 4.2) had an almost 1 L electrolyte container and was equipped with a water pump (ProFlow u 500, 6W, max. 440 L h^{-1}, D–67141 Neuhofen, Germany). In this setup the electrodes were immersed in a fiberglass cell with an inner diameter of 3.5 cm and the electrolyte was pumped through a plastic tub with an inner diameter of 6 mm. This way a maximum flow rate of 8.6 $cm^3.s^{-1}$ was applied over the sample.

Both static and flow setups used a graphite rod with a diameter of 2 mm as a counter electrode and a saturated Ag/AgCl/KCl reference electrode attached to an Autolab Eco Chemie potentiostat (PGSTAT 10). All measurements were performed in a 0.1 M sodium chloride solution.

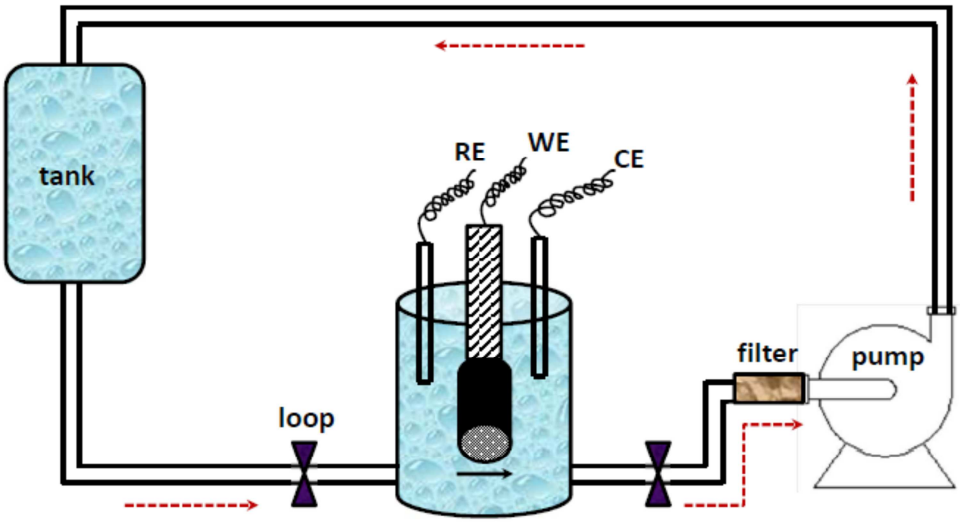

Figure 4.2. *Schematic diagram of the flow cell.*

To apply a cathodic polarization to the samples, a potentiostatic polarization was carried out at three different potentials (-1.3 V, -1.5 V, and -1.7 V vs. Ag/AgCl/KCl), each time for a duration of 600 s. The potentiodynamic polarization curves of the samples were recorded before and after the cathodic polarization in the potential range of -1.5 V and 1.3 V (vs. Ag/AgCl/KCl) with a scan rate of 1 $mV.s^{-1}$. In addition, electrochemical impedance spectroscopy measurements of the steel samples were carried out in the frequency range of 10 kHz to 0.01 Hz, with an amplitude of 10 mV at open circuit potential. Nyquist plots were recorded before and after the cathodic polarization of each sample at different cathodic potentials and under static and flow conditions.

4.1.2.3. Scanning electron and atomic force microscopy

The surface topography of the samples was examined by atomic force microscopy (AFM) after cathodic polarization by three different cathodic potentials under static and flow conditions. For this we used a Dimension Edge microscope (Bruker) with an antimony–doped silicon tip in tapping mode. The roughness parameters (in this work R_a, R_q) were provided by the software of the instrument. Further information about AFM and its applications can be found in [49].

SEM–EDS analyses were performed by a JSM–7600F (JEOL, Tokyo–Japan) scanning electron microscope and a X–MAX^N–50 EDS detector (Oxford Instruments).

4.1.3. Results and discussion

4.1.3.1. Flow motion and produced flow regime

Figure 4.3 represents the flow regime constructed by a RDE. It is known that the rotation of the electrode produces a fluid flow in a vertical direction from the solution towards the electrode surface [50, 51]. The fluid flow constructed by the flow cell, however, has a different regime. Here the electrolyte is pumped in a straight direction over the surface and exits from the cell through the outlet tube. However, we know that the electrolyte stream produced by the flow cell makes a complex vortex flow regime when it reaches the immersed electrode. Although in this work we did not study the exact flow structure produced by the flow cell, it is clear that completely different flow regimes are produced by these two flow setups. In this work these two different flow regimes were applied over the steel sample with various velocities and the corrosion behavior of the steel before and after cathodic polarization at 3 different cathodic potentials was investigated.

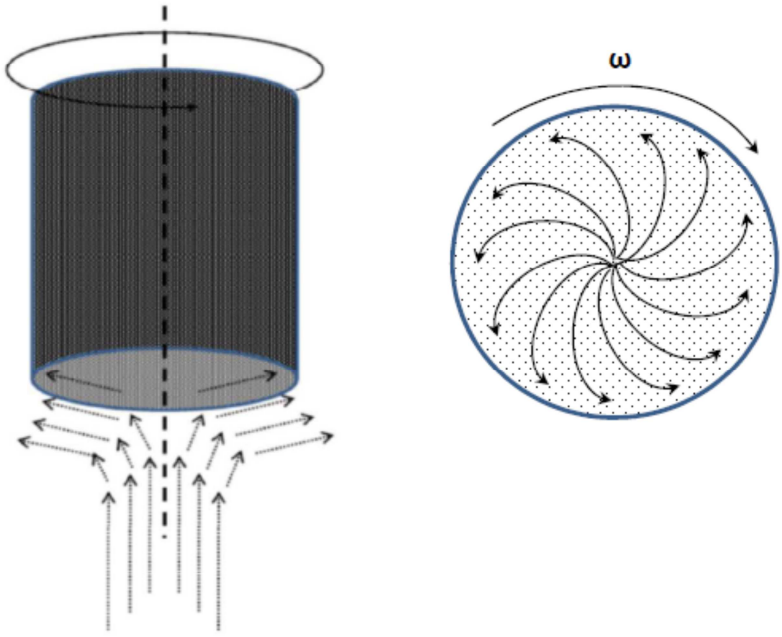

Figure 4.3. *Fluid flow profile produced by a RDE. Based on information obtained from [50, 51].*

4.1.3.2. Potentiodynamic polarization under static and flow conditions

Figure 4.4(a, b) shows the potentiodynamic polarization curves of a freshly polished 316L stainless steel coupon in a 0.1 M sodium chloride solution under static and flow conditions. These graphs were obtained using the homemade flow cell and a RDE. The applied flow rates were 1.3 $cm^3.s^{-1}$, 5.5 $cm^3.s^{-1}$, and 8.6 $cm^3.s^{-1}$ for the flow cell

and 50 rpm up to 3000 rpm for the RDE. The polarization curves show that the cathodic current density of the steel increases with flow velocity. This can be attributed to the higher rate of the cathodic reduction reaction of the dissolved oxygen in the flow system [41] (Eq. 2.26 and 2.27). In sodium chloride solution the equilibrium potentials of Equations 2.26 and 2.27 will be about 0.732 (V/ SHE) and 0.198 (V/SHE) respectively.

In Figure 4.4a (flow cell), the corrosion potential, E_{corr}, of steel changes from -0.39 V to -0.21 V (vs. Ag/AgCl/KCl) when a flow velocity of 1.3 $cm^3.s^{-1}$ is applied, increasing to -0.13 V (vs. Ag/AgCl/KCl) for a flow rate of 8.6 $cm^3.s^{-1}$. However, the anodic current densities obtained for different flow velocities show no significant difference.

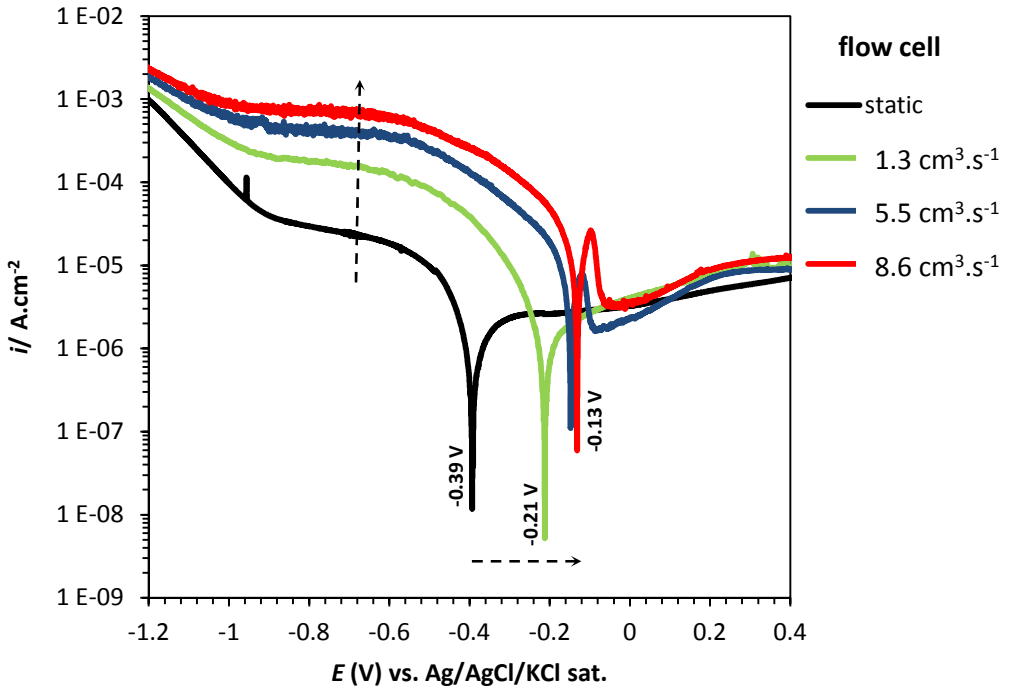

(a)

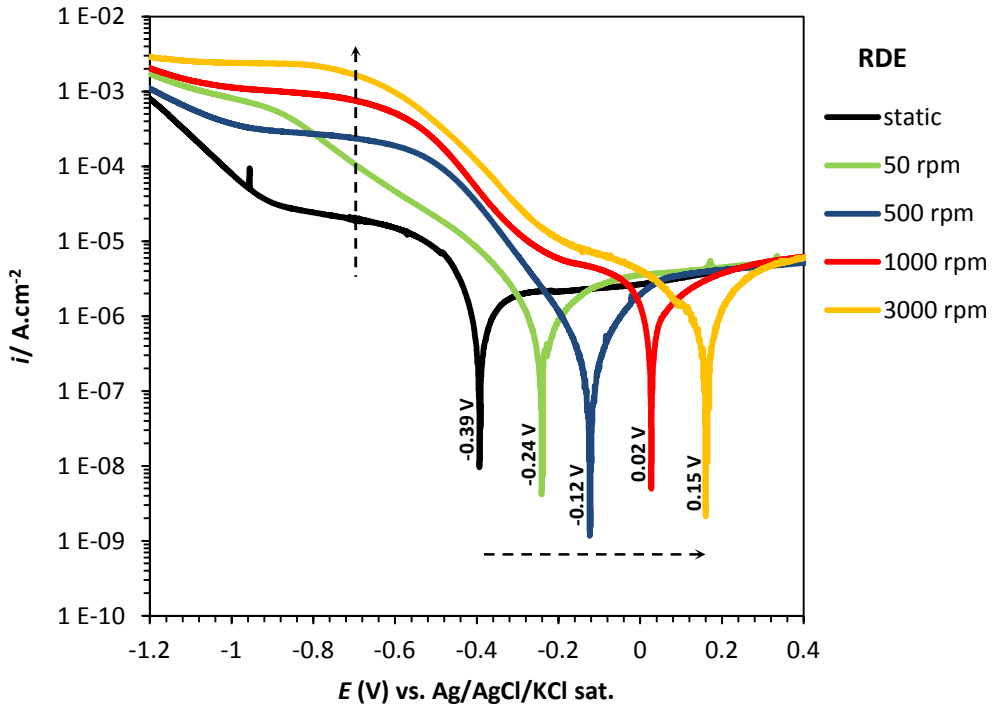

(b)

Figure 4.4. *Potentiodynamic polarization curves of steel before cathodic polarization under static and flow conditions. (a) flow cell, (b) RDE.*

Similar results were obtained using the RDE (Figure 4.4b). Here the E_{corr} of steel shifts to -0.24 V (vs. Ag/AgCl/KCl) under 50 rpm rotation rate and parallel to the increase of the rotation rate this potential increases. Finally when applying a high rotation rate (3000 rpm) the E_{corr} appears at 0.15 V (vs. Ag/AgCl/KCl).

Based on these measurements and considering the anodic and the cathodic reactions occurred on the steel surface during the anodic dissolution, the observed current and potential shifts can be explained as follows.

The main oxidation and reduction reactions during the corrosion of steel in sodium chloride solution have been mentioned in Chapter 2 (Eq. 2.24–2.27). The anodic equation shows the anodic dissolution of iron (Eq. 2.24) and is known as a pure charge transfer–controlled process [52]. The second is a cathodic reaction, described in the literature as a mixed charge transfer and mass transfer–controlled process (Eq. 2.26, 2.27) [53–55]. In the presence of a fluid flow, the diffusion–controlled cathodic reduction of dissolved oxygen is dominant. Therefore, under flow conditions, the mass transfer of oxygen from the electrolyte to the metal surface – and therefore the cathodic current density–increases, which shifts the corrosion potential towards nobler potentials.

4.1.3.3. Effect of flow velocity on the pit nucleation

According to our measurements on stainless steel, the maximum flow velocity which pits can form was found about 1.3 $cm^3.s^{-1}$ using the flow cell described in Figure 4.2. Figure 4.5 shows optical micrographs of four steel coupons after a potentiodynamic polarization in 0.1 M NaCl with a scan rate of 1 $mV.s^{-1}$ under static conditions (a) and under a fluid flow (b–d) constructed by the homemade flow cell. Figure 4.5a clearly shows pits which cover the entire surface, while after polarization of the sample under a 1.3 $cm^3.s^{-1}$ velocity the number of pits reduced and under higher velocities (5.5 and 8.6 $cm^3.s^{-1}$) no pitting was observed.

Similar experiments were performed using a RDE in order to find the maximum rotation rate where pitting occurs over the steel surface. The results showed that with rotation rates below 500 rpm, pitting is easily detected after a potentiodynamic polarization. However, higher rotation rates prevent pitting over the steel surface.

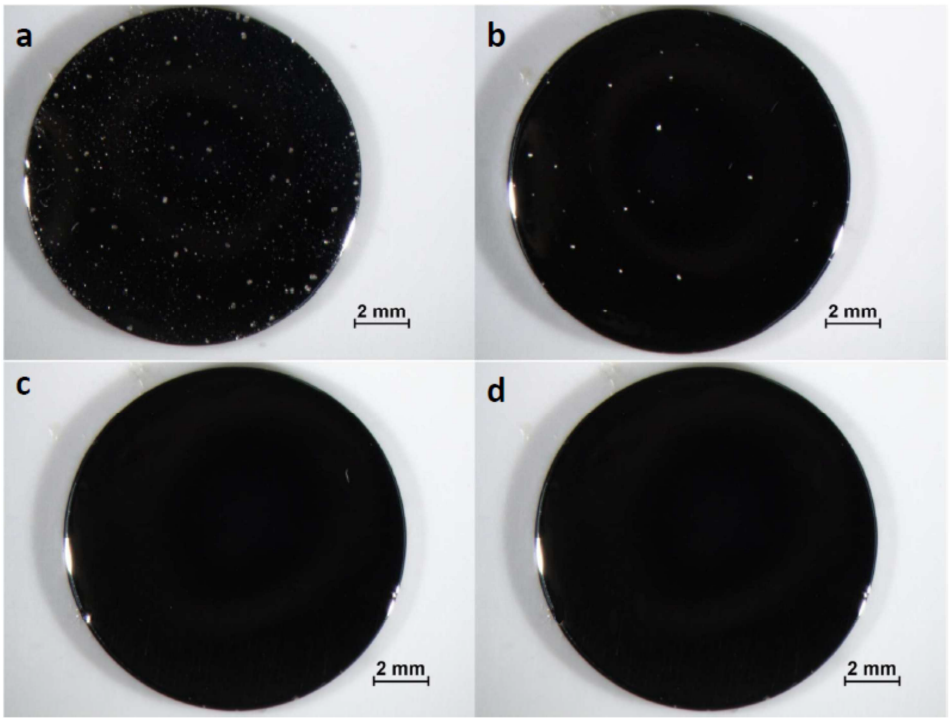

Figure 4.5. *Optical micrographs of the pitting corrosion on the steel coupons after a potentiodynamic polarization in a 0.1 M NaCl solution under different flow velocities produced by the flow cell. (a) static, (b) 1.3 $cm^3.s^{-1}$, (c) 5.5 $cm^3.s^{-1}$, (d) 8.6 $cm^3.s^{-1}$ (scan rate: 1 $mV.s^{-1}$).*

4.1.3.4. Effect of the flow velocity on cathodically polarized steel

Figure 4.6a shows the potentiodynamic polarization curves of steel before and after cathodic polarization of the samples at three different potentials under static conditions.

In this work after each potentiostatic polarization measurement the generated hydrogen gas bubbles were removed from the surface of the steel electrode by gently stirring the solution after the measurement for static conditions. Under dynamic conditions however, the produced electrolyte flow removes the gas bubbles from the surface during the cathodic polarization.

Similar to the non–polarized curves shown in Figure 4.4, the cathodic parts of the potentiostatic polarization plots here also exhibit a greater current density, which can be attributed to the higher mass transfer of the cathodic reactions on the electrode–electrolyte interface (Eq. 2.26 and 2.27). The corrosion potential of the non–polarized sample is around -0.39 V (vs. Ag/AgCl/KCl), which increases to -0.09 V (vs. Ag/AgCl/KCl) after polarization at -1.3 V (vs. Ag/AgCl/KCl) for 600 s. By increasing the cathodic polarization potential to -1.5 V, E_{corr} shifts to -0.05 V (vs. Ag/AgCl/KCl) and, finally, after polarization at -1.7 V (vs. Ag/AgCl/KCl) for 600 s, this potential reaches 0.01 V (vs. Ag/AgCl/KCl). Unlike in Figure 4.4, the cathodically polarized samples show higher anodic current densities than the non–polarized samples, increasing corrosion current densities for all the cathodically polarized samples.

The potentiodynamic graphs in Figure 4.6a show that more oxygen gets reduced over the cathodically polarized steel. Therefore it can be concluded that the thickness of the diffusion layer decreases under effect of cathodic polarization under static conditions and this increases the rate of oxygen mass transfer and raises the cathodic current density during the potentiodynamic polarization.

When the potential reaches the anodic part of the potentiostatic polarization curves, the hydrogen–containing micropits act as preferential sites for chloride ions and increase the anodic current density and favor pitting. Furthermore, the oxidation of the absorbed hydrogen atoms and also the synergistic effect of hydrogen and chloride ions contribute the oxidation current density (Eq. 4.4) and this increases the total current density of the cathodically polarized steel.

Figure 4.6b shows the potentiostatic polarization curves of the same series of the experiments measured under the RDE flow conditions with a rotation rate of 500 rpm. This figure reveals that the cathodic polarization of steel under the flow regime of the RDE increases the cathodic current density produced by the reduction of oxygen during the potentiodynamic polarization of steel. Similar to Figure 4.6a here also due to the decrease in the thickness of the diffusion layer during the cathodic polarization process the mass transfer rate of oxygen increases and results in higher cathodic current density in the measured potentiodynamic polarization graphs. Moreover, the anodic current density of steel increases and the pitting potential which is known to be independent of flow [56] shifts towards less noble potentials after application of

greater cathodic potentials. Similar results with only higher current densities were obtained when higher rotation rates (up to 5000 rpm) were applied.

Figure 4.6c shows the potentiodynamic polarization curves of steel before and after 600 s cathodic polarization by three cathodic potentials under flow conditions constructed by the flow cell with a flow velocity of 8.6 $cm^3.s^{-1}$. Unlike the static conditions and the graphs measured under flow regime of the RDE, here after application of cathodic polarization the cathodic current densities decrease. In addition, E_{corr} of the steel shifts towards less noble potentials. Under a flow of 8.6 $cm^3.s^{-1}$, E_{corr} is found to be -0.13 V (vs. Ag/AgCl/KCl), which decreases to -0.31 V, -0.38 V, and -0.46 V (vs. Ag/AgCl/KCl) after cathodically polarizing the steel samples with cathodic potentials of -1.3 V, -1.5 V, and -1.7 V (vs. Ag/AgCl/KCl) for 600 s, respectively.

The Tafel plots of Figure 4.6c reveal that under the flow regime of the flow cell the rate of the oxygen reduction reaction decreases with the application of a greater cathodic potential during the cathodic polarization process. This can be attributed to the increase of the thickness of the diffusion layer which directly effects over the mass transfer rate of the dissolved oxygen and therefore, reduces the cathodic current density.

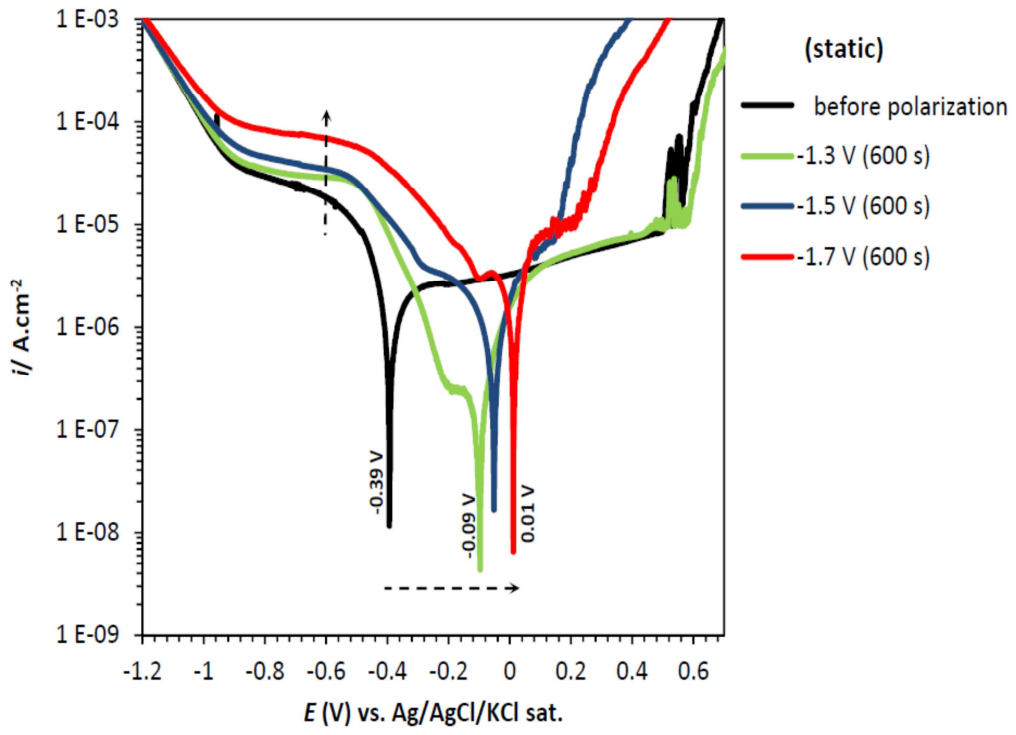

(a)

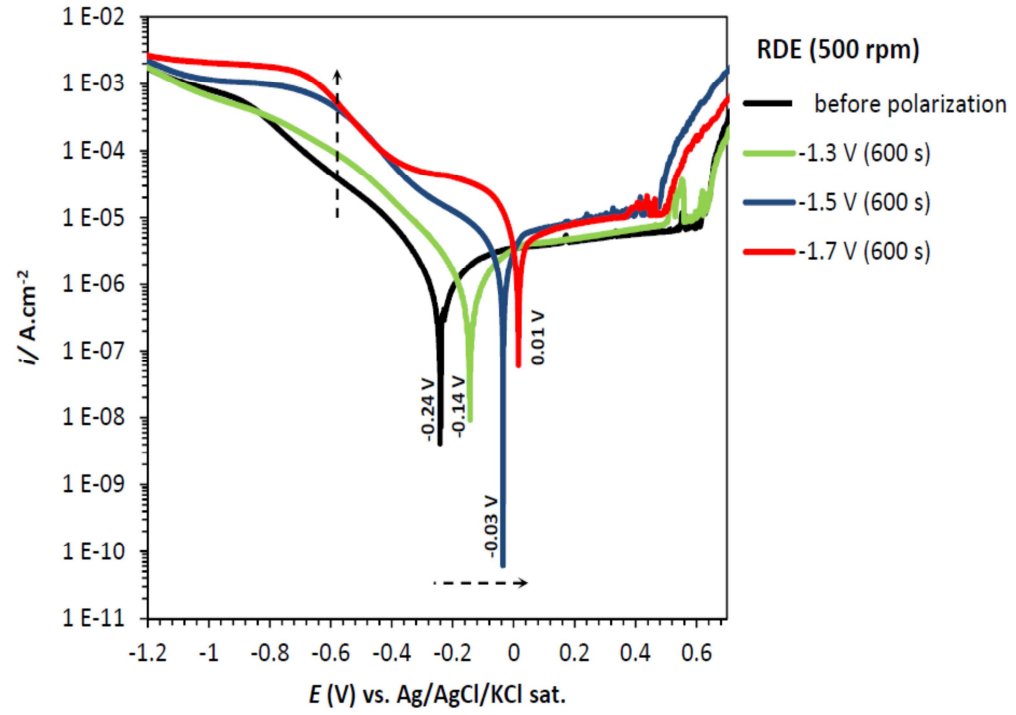

(b)

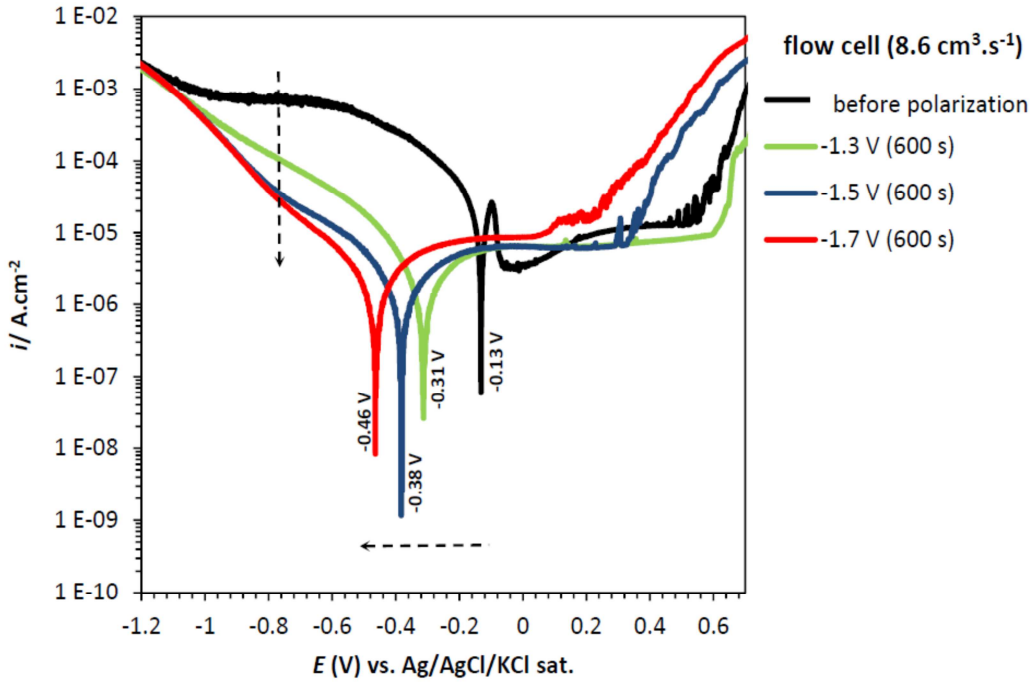

(c)

Figure 4.6. *Potentiodynamic polarization curves of steel before and after cathodic polarization by three different cathodic potentials under (a) static, (b) fluid flow applied by the RDE (500 rpm) (c) 8.6 $cm^3.s^{-1}$ fluid flow applied by the flow cell.*

Figure 4.7 shows the variation of E_{corr} of the cathodically polarized steel versus the applied cathodic potentials under both static and flow conditions with two flow regimes. Each E_{corr} value represents an average of at least 3 measurements. When a greater cathodic potential is applied during cathodic polarization under flow conditions constructed by the flow cell (8.6 $cm^3.s^{-1}$), E_{corr} decreases. However, under static conditions and also under flow regime of the RDE, E_{corr} increases with the applied cathodic potential.

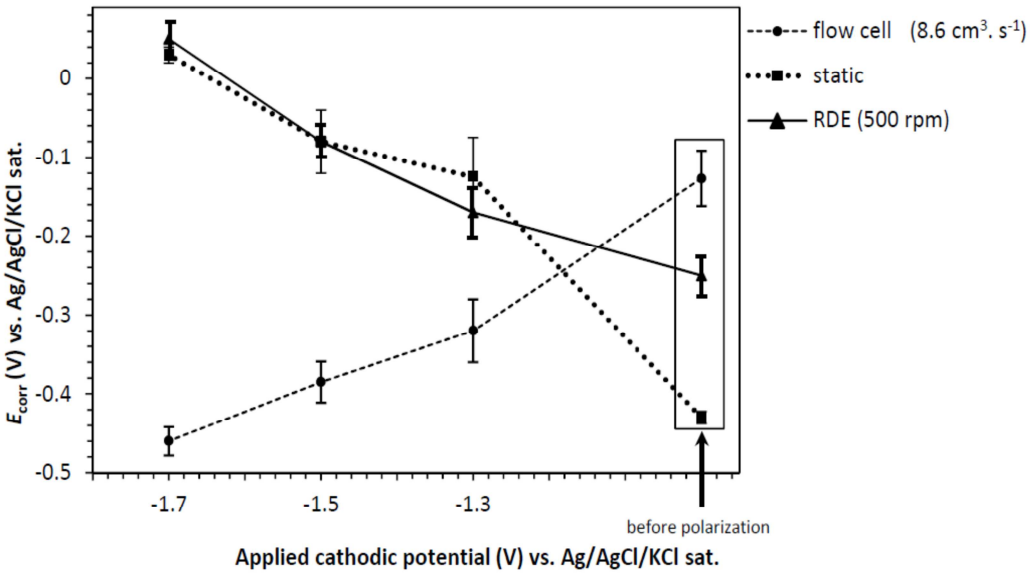

Figure 4.7. *Variations of the E_{corr} of steel versus the applied cathodic potential under static conditions and two different flow regimes.*

Figure 4.8 depicts the hydrogen reduction process over the steel surface during the cathodic polarization and its effect on the cathodic current density produced under static and two different flow conditions (RDE and flow cell) for three different cathodic potentials. The dotted arrows show the cathodic current reduction after the accumulation of hydrogen gas bubbles on the steel surface under static conditions. In the case of 300 s and 500 s cathodic polarization at a potential of -1.7 V (vs. Ag/AgCl/KCl) under static conditions, a rapid increase in the cathodic current density is detected, which is attributed to the exit of hydrogen bubbles. The formed gas bubbles during the cathodic polarization decrease the active surface area and therefore reduce the cathodic current density under static conditions. According to our observation during the measurements under static conditions small gas bubbles appear from the beginning of the polarization process. These small bubbles after become larger and cover a larger area of the surface and decrease the current density. Further

increase in the size of the bubbles over the surface exit the hydrogen bubble and once again increases the cathodic current density. However, under the both flow conditions, the chronoamperograms exhibit almost constant values after 600 s of polarization.

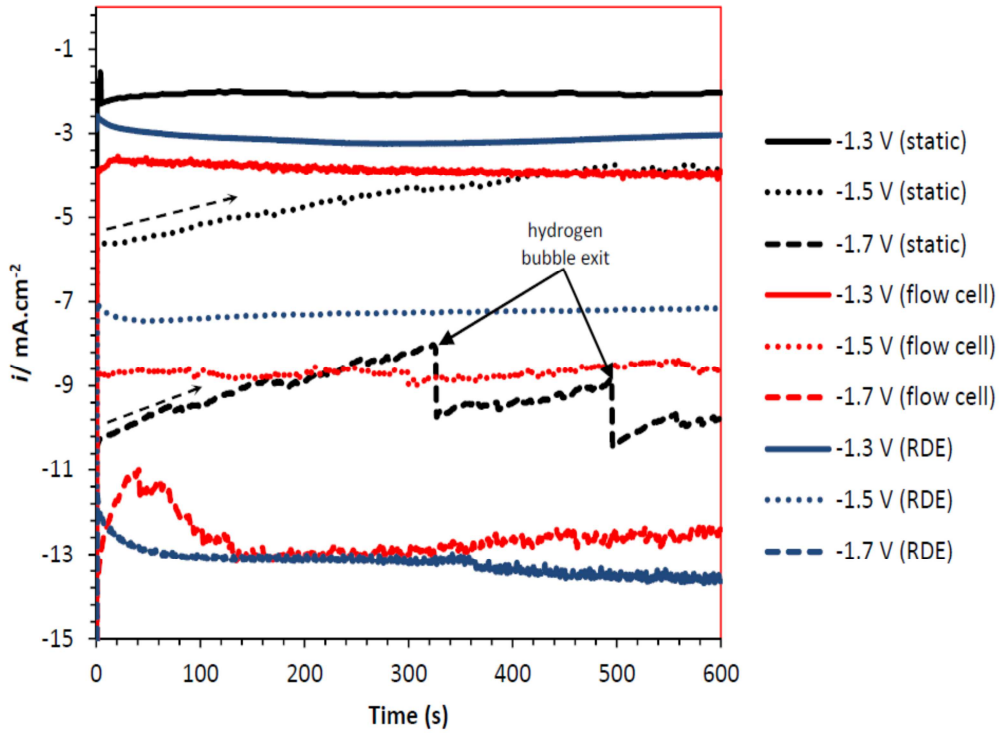

Figure 4.8. *Chronoamperograms of steel for three different cathodic potentials under static conditions and two different flow regimes.*

4.1.3.5. Surface morphology of the cathodically polarized steel

Figure 4.9 shows the AFM images of the steel surface before and after cathodic polarization for 600 s at three different cathodic potentials under both static and flow conditions constructed by the flow cell. The cathodic corrosion of the surface forms metal particles that are transferred into the electrolyte. After a 600 s polarization of the surface at -1.3 V (vs. Ag/AgCl/KCl) in static mode, the surface roughness increases and keeps on increasing as the cathodic potentials become larger. This growth intensifies under flow conditions, with peak heights reaching 44.5 nm, 56.9 nm, and 66.9 nm after 600 s cathodic polarization at -1.3 V, -1.5 V, and -1.7 V (vs. Ag/AgCl/KCl), respectively. It is obvious that sharpening of the surface grooves increases the true surface area.

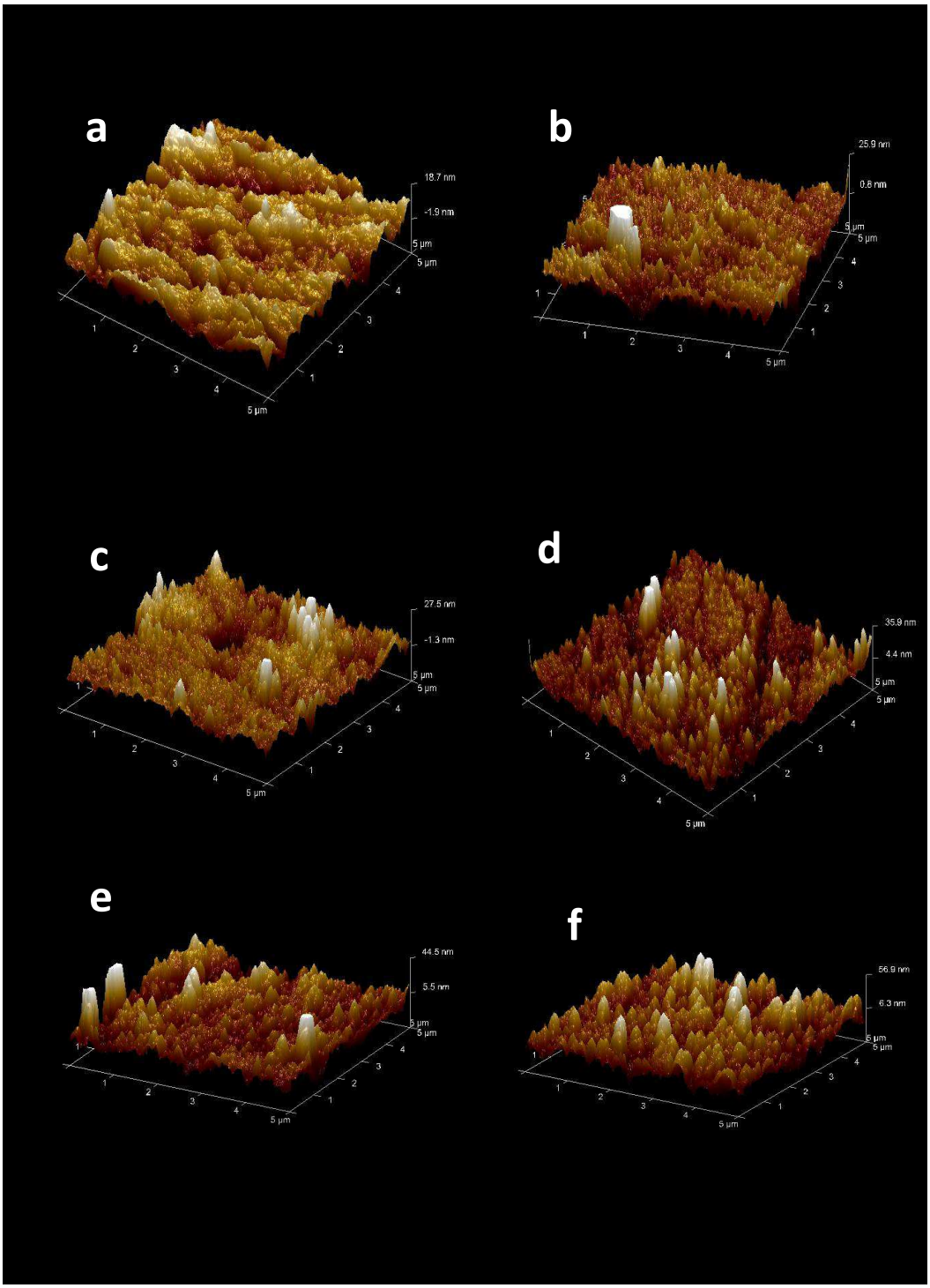
a
18.7 nm
-1.9 nm
5 µm
5 µm
b
25.9 nm
0.8 nm
5 µm
5 µm
c
27.5 nm
-1.3 nm
5 µm
5 µm
d
35.9 nm
4.4 nm
5 µm
5 µm
e
44.5 nm
5.5 nm
5 µm
5 µm
f
56.9 nm
6.3 nm
5 µm
5 µm

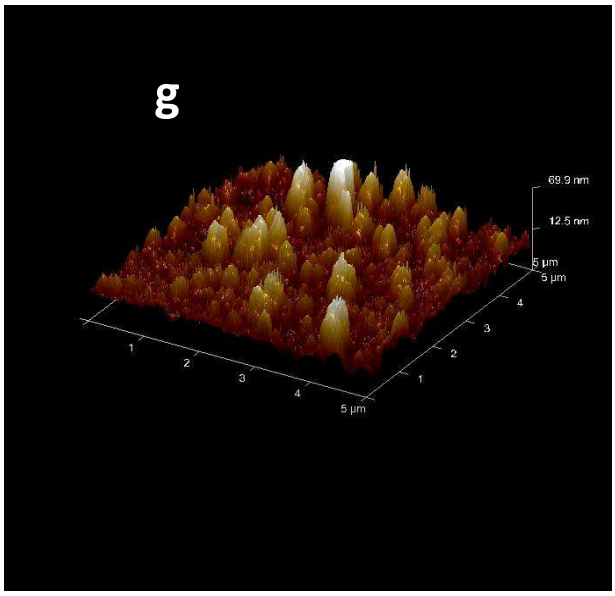

Figure 4.9. *Atomic force microscopy images of steel (a) before cathodic polarization under static conditions, (b) after 600 s cathodic polarization by -1.3 V (vs. Ag/AgCl/KCl) under static conditions, (c) after 600 s cathodic polarization by -1.5 V (vs. Ag/AgCl/KCl) under static conditions, (d) after 600 s cathodic polarization by -1.7 V (vs. Ag/AgCl/KCl) under static conditions, (e) after 600 s cathodic polarization by -1.3 V (vs. Ag/AgCl/KCl) under 8.6 $cm^3.s^{-1}$ flow, (f) after 600 s cathodic polarization by -1.5 V (vs. Ag/AgCl/KCl) under 8.6 $cm^3.s^{-1}$ flow, (g) after 600 s cathodic polarization by -1.7 V (vs. Ag/AgCl/KCl) under 8.6 $cm^3.s^{-1}$ flow. The flow conditions was produced by the flow cell.*

Figure 4.10 shows the variation of the roughness parameters R_a and R_q of steel versus the cathodic potentials applied under both static and flow conditions. Here R_a and R_q are the arithmetic mean and root mean squared, respectively, of the deviations in height from the profile mean value. Both the R_a and R_q parameters increase with the cathodic potential; however, they increase with the slope after the samples are polarized under the fluid flow that has the greater cathodic polarization effect on the surface topography of steel under flow conditions.

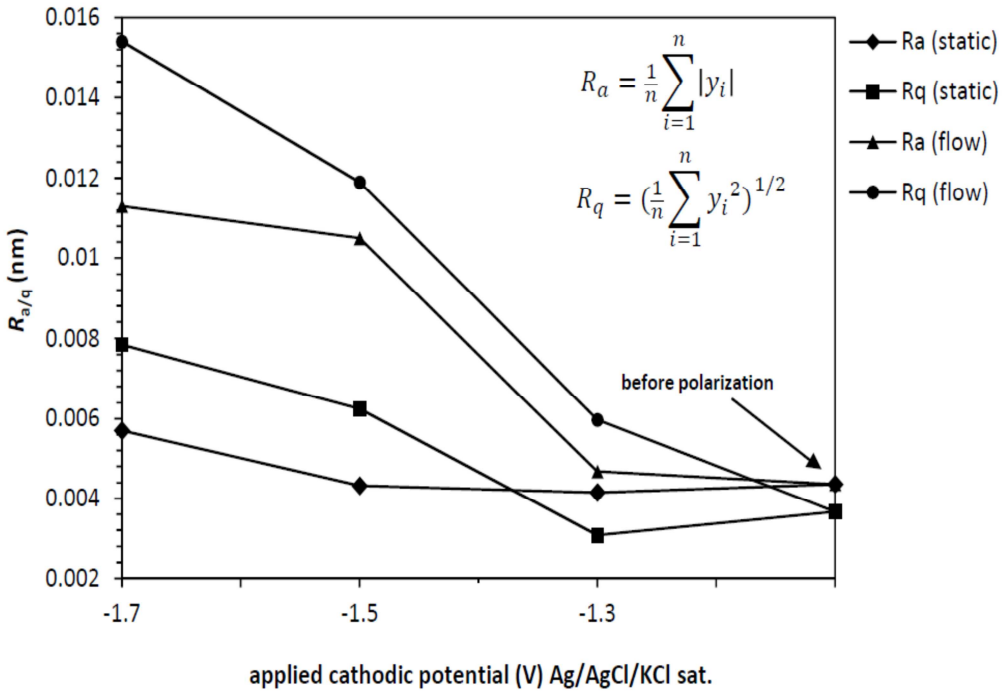

Figure 4.10. *The roughness parameters (R_a and R_q) of the steel surface versus the applied cathodic potential after 600 s cathodic polarization in 0.1 M sodium chloride solution.*

Figure 4.11 represents the SEM images of the steel samples before and after 600 s cathodic polarization under static conditions and flow conditions constructed by the RDE with a rotation rate of 500 rpm. These images clearly show the formed metal particle clusters over the steel surface. It is expected that part of the formed metal particles are transferred into the solution during the cathodic polarization.

In image d the characterization of the observed particles was performed by energy dispersive spectroscopy (EDS). The spectra are shown in Figure 4.12. The EDS analysis performed on the white part of the metal cluster shows sharp peaks of aluminum and oxygen. Higher intensity of the aluminum peak than of iron and chromium reveals the major part of the white cluster to be Al_2O_3.

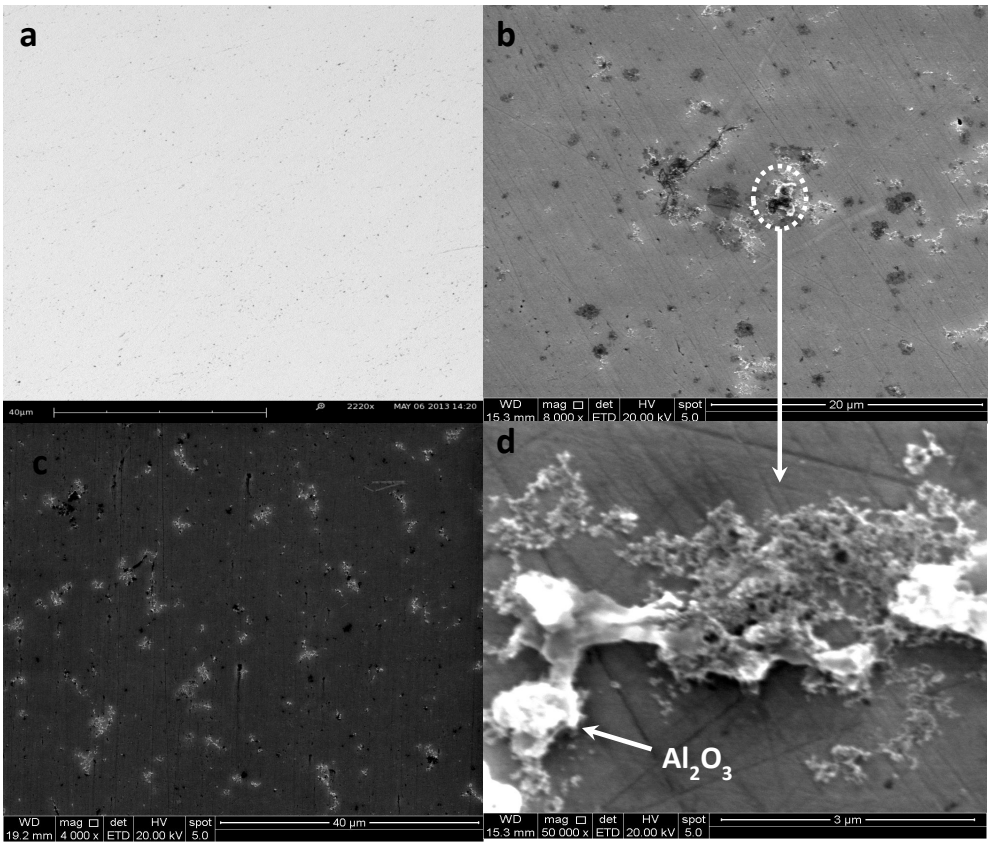

Figure 4.11. *SEM images of steel (a) before cathodic polarization, (b) after 600 s cathodic polarization at -1.7 V (vs. Ag/AgCl/KCl) under static conditions, (c) after 600 s cathodic polarization at -1.7 V (vs. Ag/AgCl/KCl) under flow conditions constructed by the RDE (500 rpm) and (d) focused view of image (b).*

The EDS spectrum of the black part of the metal cluster however, shows a sharp iron peak. Here the second sharpest peak is observed for chromium. Considering the lower intensity of aluminum and oxygen peaks compared to the white area of the cluster depicts the presence of iron and chromium as the major elements in the darker part of the analyzed metal cluster. In this analysis other elements such as carbon, silicon, molybdenum and nickel particles were detected as well which reveals that the cathodic polarization process produces metal particles over the surface.

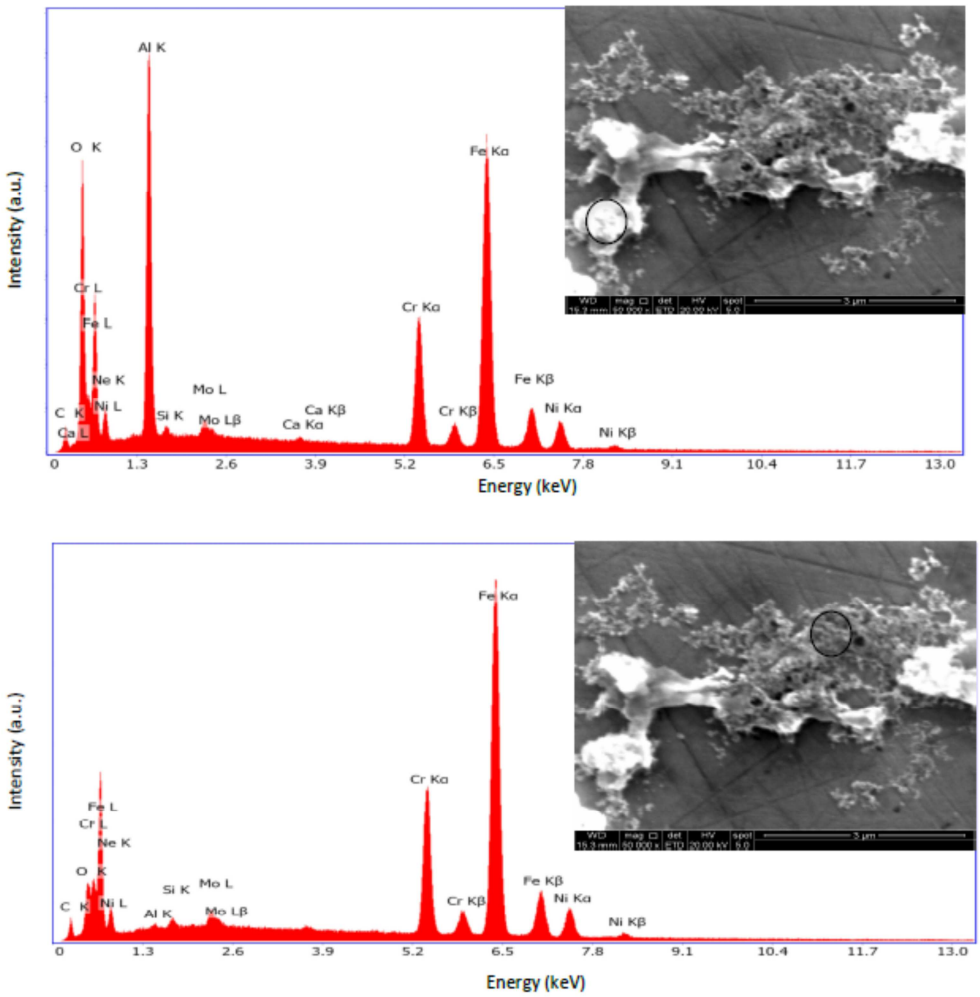

Figure 4.12. *SEM–EDS spectra of the metal particle clusters formed on steel after 600 s cathodic polarization at -1.7 V (vs. Ag/AgCl/KCl) under static conditions.*

4.1.3.6. Electrochemical impedance spectroscopy

The corrosion resistance of steel before and after cathodic polarization under static and dynamic conditions produced by the flow cell was investigated by electrochemical impedance spectroscopy. The Nyquist graphs in Figure 4.13a show lower imaginary impedance values after cathodic polarization at -1.5 V and -1.7 V (vs. Ag/AgCl/KCl), while the Nyquist graphs of the non–polarized sample and the cathodically polarized sample at a potential of -1.3 V (vs. Ag/AgCl/KCl) almost overlap. Under flow conditions, however, the effect of cathodic polarization is clearer. At low velocities (Figure 4.13b) the Nyquist graphs of the cathodically polarized steel at -1.3 V and -1.5 V (vs. Ag/AgCl/KCl) overlap. As expected, the smallest diameter of the impedance graph is observed for the cathodically polarized steel after application of a -1.7 V (vs. Ag/AgCl/KCl) cathodic potential. At a flow velocity of 8.6 $cm^3.s^{-1}$ (Figure 4.13c) the diameter of the cathodically polarized graphs decreases more significantly, where the

maximum imaginary impedance of the polarized steel after applying a cathodic potential of -1.3 V (vs. Ag/AgCl/KCl) is about 8 kΩ cm^2, which decreases to around 3 kΩ cm^2 after the steel is polarized at -1.5 V and -1.7 V (vs. Ag/AgCl/KCl). Moreover, the graphs for both the static and flow modes show that the corrosion resistance of steel decreases with increasing cathodic polarization potential, especially for high flow velocities. Similar results were observed when a RDE was used to produce the flow conditions (not shown).

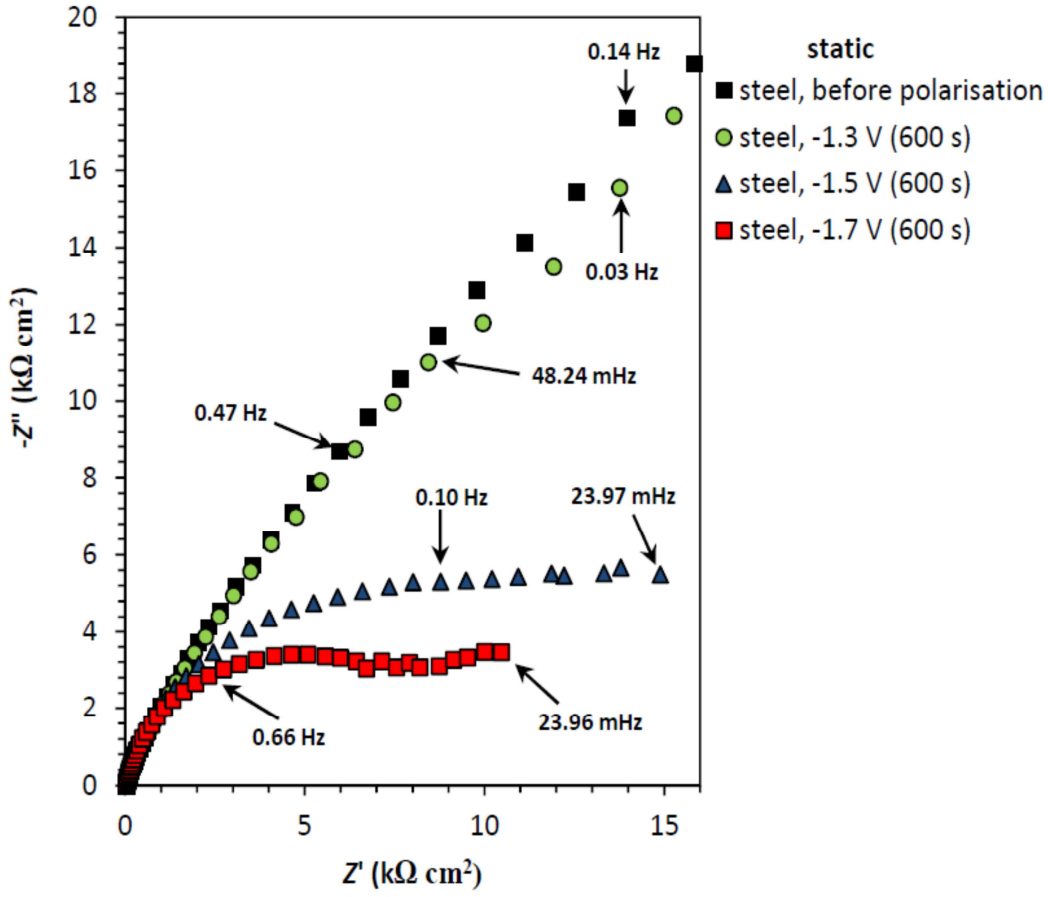

(a)

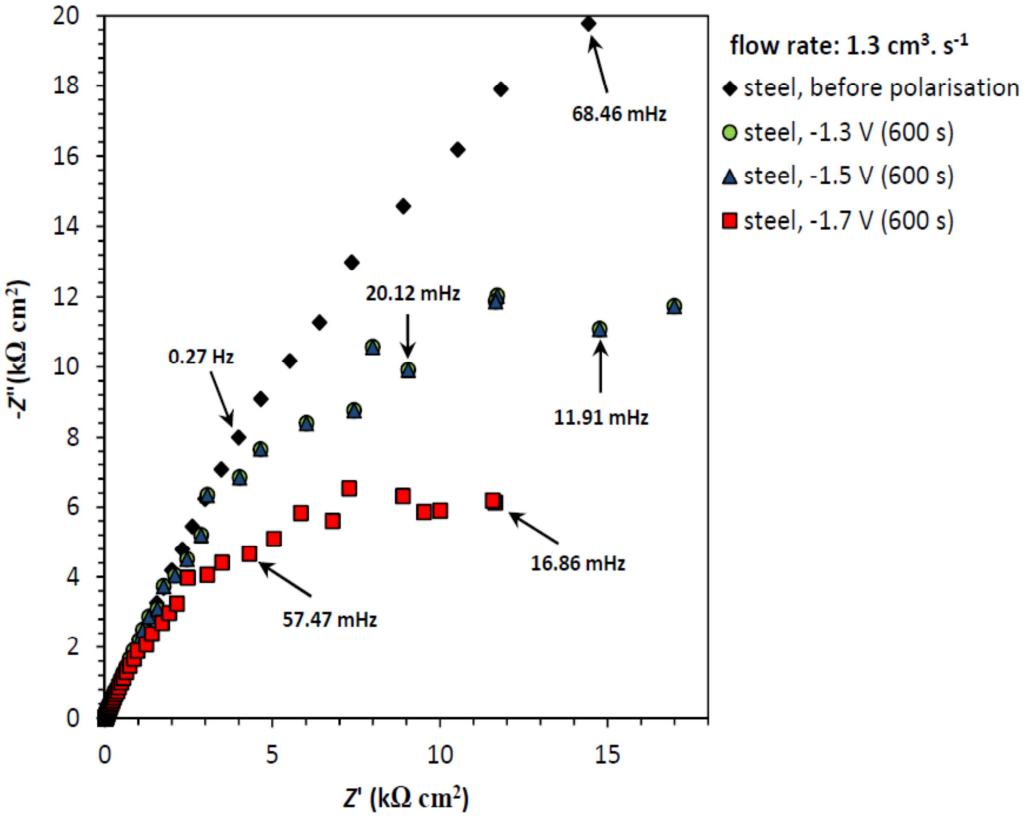

(b)

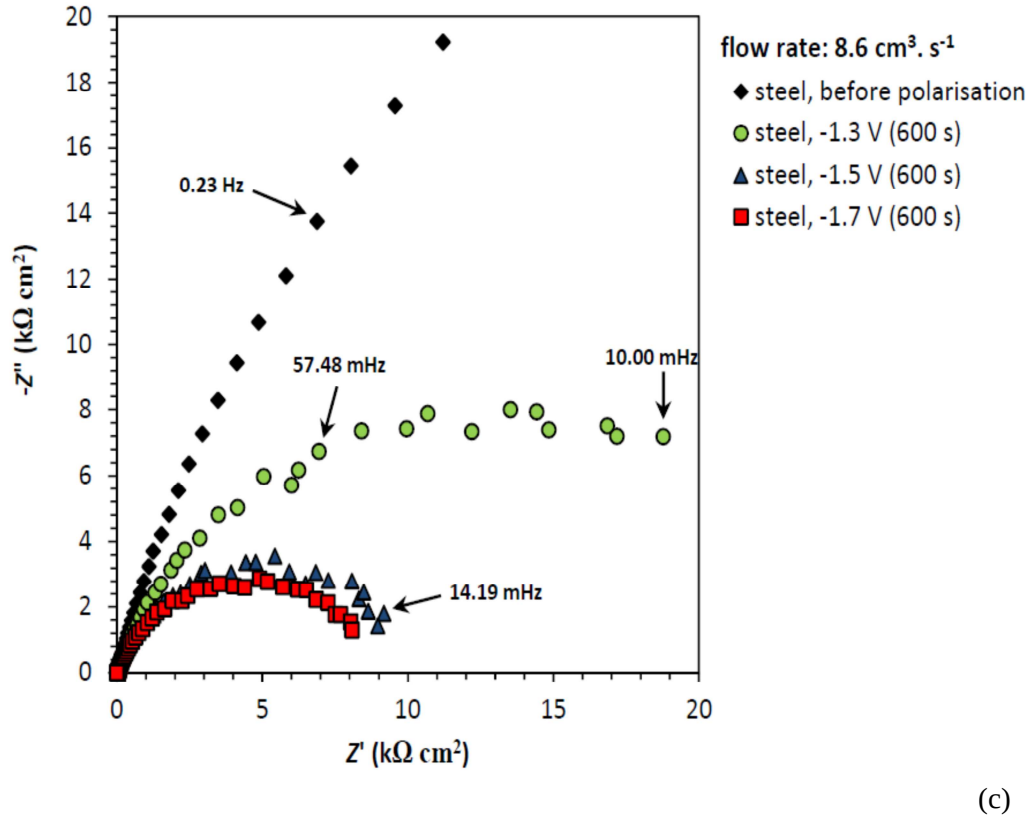

(c)

Figure 4.13. *Nyquist graphs of steel before and after cathodic polarization for three different cathodic potentials under (a) static, (b) low flow*

velocity (1.3 $cm^3.s^{-1}$), and (c) high flow velocity (8.6 $cm^3.s^{-1}$) conditions. The flow conditions were produced by the flow cell.

According to the measured potentiodynamic polarization curves and the Nyquist graphs and the obtained AFM images (Figure 4.9) it can be concluded that as the hydrogen entry on the surface occurs with greater intensity with application of greater cathodic potential, the cathodic corrosion process changes the morphology of the oxide film and increases the true surface area of the steel with more intensity. Greater amount of the absorbed hydrogen into the oxide film decreases the stability of the passive layer and increases the corrosion current density and therefore decreases the corrosion resistance of the steel.

These results are in good agreement with the impedance data reported by some other authors [42, 57–59] where the application of the cathodic polarization process with greater intensity decreases the diameter of the impedance graphs.

4.2. Cathodic polarization of 304L stainless steel on a static micro scale

The second part of this work involves the investigation of type 304L stainless steel in the presence of chloride ions but on a micro scale level. This was performed by cathodically polarizing the steel in a 1 M sodium chloride solution under a 200 μm microcapillary. The main idea of the miniaturization of the cathodic polarization process was to study the effect of the geometry of the working electrode on the corrosion procedure of steel especially its effect on E_{pit} of steel during the dissolution of steel in an aggressive media such as NaCl solution.

The microcell setup described in Chapter 3 was used for miniaturization of the working electrode (304L stainless steel).

4.2.1. Experimental

4.2.1.1. Chemicals

A 1 M sodium chloride solution was prepared using analytical grade NaCl powder (Fluka). In addition a mixture of 1.5:1 ratio HNO_3/H_2O (Fluka) was prepared to etch the sample.

4.2.1.2. Specimen and surface preparation

A 304L stainless steel coupon with the following chemical composition (wt. %): Cr: 17.65, Ni: 8.59, Mn: 1.75, Si: 0.41, C: 0.017, P: 0.032 and S: 0.005 was used in this study.

The preparation procedure of the steel sample (diameter of 12.5 mm and thickness of 2 mm) was the same as Section 4.1. The microcapillary diameter used in this work is about 200 μm (wetted area ~ 314×10^{-6} cm^2). The procedure described in Section 1.3 was followed to make the microcapillary.

Observation of the steel microstructure becames possible after a surface etching procedure. Etching was done by immersing a polished steel coupon in a 1.5 : 1 mixture of HNO_3/H_2O for up to 80 s [60]. An optical image of the steel coupon after etching is shown in Figure 4.14. The mean grain size of the steel was estimated using the linear intercept method. The main idea of this method is counting the number of grains intercepted by one or more straight lines sufficiently long enough to yield at least 50 intercepts [61]. The mean grain size of the steel used in this work is about 19.26 μm. The latter was obtained after three linear intercept measurements on three microscopic images of different areas of the sample.

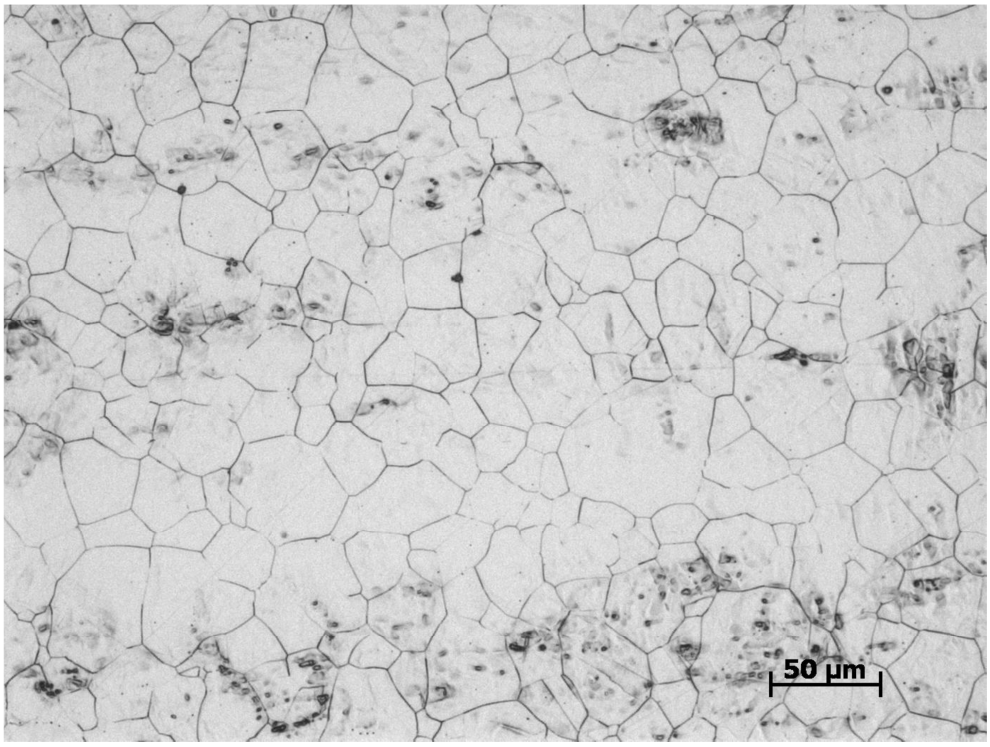

Figure 4.14. *Optical image of the microstructure of the etched 304L stainless steel sample.*

4.2.2. Electrochemical measurements

The potentiostatic polarization was performed at five different potentials (-1, -1.3, -1.5, -1.7 and -1.9 V vs. Ag/AgCl/KCl) each with a duration time of 600 s. Tafel plots of the steel sample were recorded before and after each cathodic polarization in the potential range of -1.5 and 1.3 V (vs. Ag/AgCl/KCl) and a scan rate of 10 $mV.s^{-1}$. The

latter allowed us to determine the corrosion potentials, corrosion currents and also the pitting potentials of the stainless steel under the different conditions. In between the potential polarization at a specific voltage, followed by the linear sweep voltammetry as described above, the microcapillary was moved to another spot of the sample for a new set of measurements at a different potential.

Each series of the measurements was performed on one steel coupon after one surface preparation procedure in two small surface areas of about 4 × 4 mm next to each other. In order to test the reproducibility of the measurements the experiments were also repeated on two other coupons under the same conditions.

4.2.3. X–ray photoelectron spectroscopy and atomic force microscopy

The surface analysis of the measured area after the electrochemical measurements was performed by X–ray photoelectron spectroscopy (S–probe monochromatized XPS spectrometer) with a voltage and power of the source of respectively 10 kV and 200 W. Further information about XPS can be found in [62].

Atomic force microscopy was used to investigate the roughness of the catodically polarized steel. The measurements were performed with a Nanoscope IIIa Multimode instruments applying tapping mode.

4.2.4. Results and discussion

4.2.4.1. Potentiostatic and potentiodynamic polarization

Figure 4.15 shows the variation of the corrosion potential (E_{corr}), the anodic current density and the pitting potential (E_{pit}) of the steel sample in the 1 M sodium chloride solution before and after cathodic polarization. The corrosion potential of steel after the cathodic polarization decreases as greater negative cathodic potential is applied. The potential for the non–polarized sample is around -0.568 V (vs. Ag/AgCl/KCl) and this decreases to -0.627 V (vs. Ag/AgCl/KCl) after the polarization of -1 V during 600 s. By increasing the cathodic polarization to -1.3 V, the corrosion potential of the sample decreases to -0.651 V (vs. Ag/AgCl/KCl). Finally after polarizing the sample at -1.5 V, -1.7 V and -1.9 V, the corrosion potential of steel decreases further to -0.670 V (vs. Ag/AgCl/KCl).

This decreases in E_{corr} is attributed to the lower reduction rate of oxygen in the cathodically polarized surface. Part of the generated gas bubbles (mainly hydrogen) remains over the steel surface under the microcapillary and also in the diffusion layer and blocks the pathway of oxygen. Therefore, less oxygen participates in the reduction reaction during the potentiodynamic polarization. This decreases the

cathodic current density in the Tafel plots and shifts the E_{corr} towards more negative potentials.

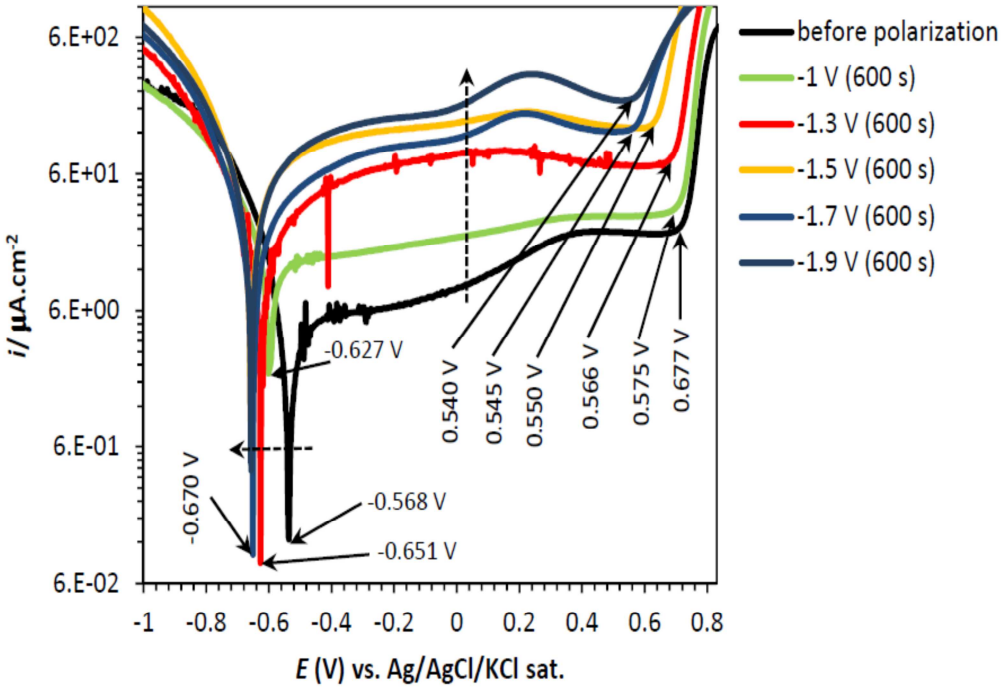

Figure 4.15. *Variation of the anodic current density, E_{corr} and E_{pit} of steel (a) before and after 600 s of potentiostatic polarization at five different potentials (b) -1 V, (c) -1.3 V, (d) -1.5 V, (e) -1.7 V and (f) -1.9 V (vs. Ag/AgCl/KCl) in a 1 M sodium chloride solution. Tip diameter of the microcapillary is ca. 200 µm.*

Figure 4.15 also demonstrates that the pit initiation of the non–polarized steel sample appears at 0.677 V (vs. Ag/AgCl/KCl) while after the potentiostatic polarization of -1 V (vs. Ag/AgCl/KCl), the pit nucleation starts at more negative potentials (0.575 V vs. Ag/AgCl/KCl) and then continuously drops till 0.540 V (vs. Ag/AgCl/KCl) as greater negative cathodic potentials are applied. The pitting of steel starts at less noble potentials after the cathodic polarization because the cathodic polarization process affects the protective oxide layer of the steel and creates more weak points over the measured surface. Therefore, pitting initiates at lower potentials than non–polarized (cathodically) surface.

Another effect of the cathodic polarization appears at the anodic part of the Tafel plots in Figure 4.15 where the anodic/passive current density increases when applying

higher cathodic potentials. This can be explained in a similar way to the previous section of this chapter (Section 4.1), where the effect of prior cathodic polarization on a large scale steel disc electrode was discussed.

However, also here the cathodic polarization of steel under the microcapillary causes micro cracks/pits on the surface, increases the true surface area and promotes the anodic dissolution of steel. Greater negative cathodic potentials affect the oxide layer with greater intensity and this results in a larger anodic current density for cathodically polarized surfaces than non–polarized sample.

Overall, Figure 4.15 clearly shows that the pitting potential, the corrosion potential and in general the corrosion resistance depend on the applied cathodic potential which cathodically corrodes metals–alloys. This current and the potential shift and its amount are attributed to the hydrogen atoms, which absorb into the passive layer during the cathodic polarization process [1].

Similar results were obtained when a modified microcapillary setup with a nitrogen shielding was used (Figure 3.3). Due to the lower rate of oxygen reduction and therefore, a lower cathodic current density of the potentiodynamic polarization curves, lower current density (anodic and cathodic) and more negative corrosion potentials compared to the potentiodynamic polarization curves measured by the non–modified setup (Figure 3.4).

In contrast to Figure 4.6a, on a micro scale with an increase of the applied cathodic potential, E_{corr} of steel shifts towards more negative potentials. However, the anodic parts of the potentiodynamic polarization curves on both macro (Figure 4.6a) and micro scale (Figure 4.15) show a higher current density for a greater cathodic potential. It can be concluded from these two figures that the differences between the micro and macro scale corrosion cells with different oxygen concentration constructed by the microcapillary and a conventional large scale disc electrode directly affect the kinetics of the reduction of the dissolved oxygen during the anodic polarization. Under the microcapillary the rate of the oxygen reduction does not change significantly. Part of the generated hydrogen bubbles remains in the diffusion layer of the measured surface, blocks the pathway of oxygen and therefore, decreases the rate of the oxygen transfer. However, similar to Figure 4.6a here also the cathodic polarization process decreases the thickness of the diffusion layer which can increase the rate of mass transfer. The competition between these two factors results in the almost constant cathodic current densities in Figure 4.15.

4.2.4.2. X–ray photoelectron spectroscopy

The chemical composition of the corroded area after 600 s potentiostatic polarization at -1.3 V (vs. Ag/AgCl/KCl) was studied by XPS (Figure 4.16). The spectra show only steel elements with the highest concentration (here Fe, Cr). Low intensity peaks of Na and Cl also were detected which are not mentioned in this figure. According to these results the expected composition of the corroded area of the steel are mainly Fe_2O_3 and Cr_2O_3 plus small amounts of $FeCl_3$ and $CrCl_3$.

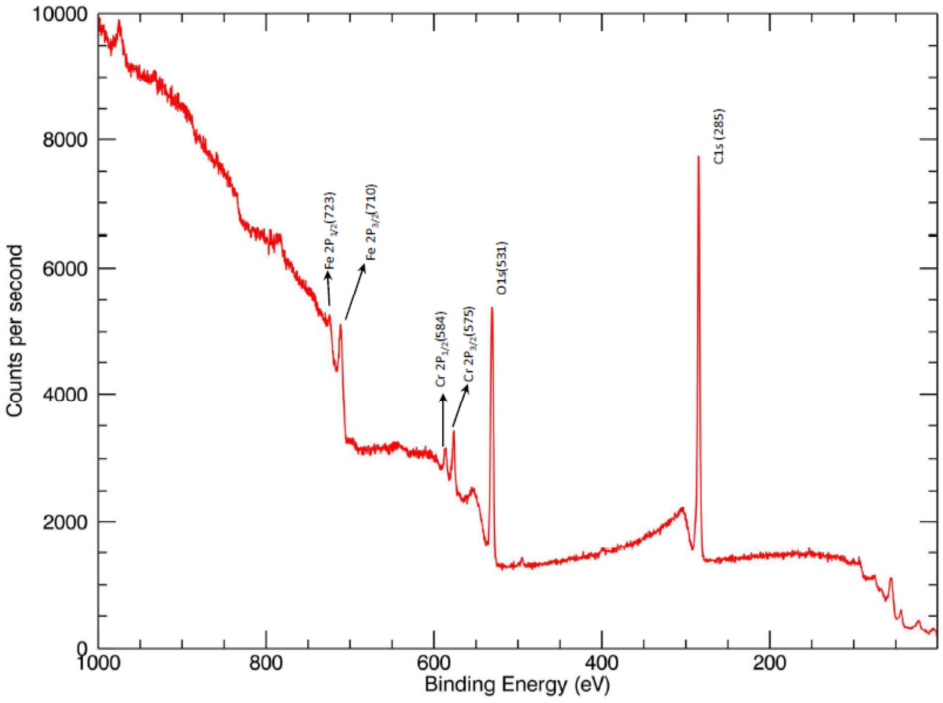

(a)

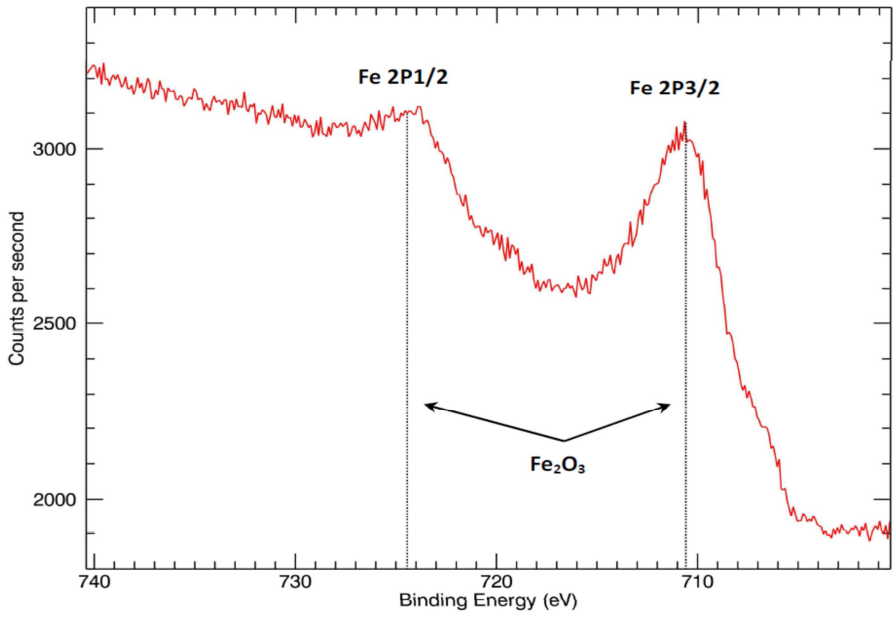

(b)

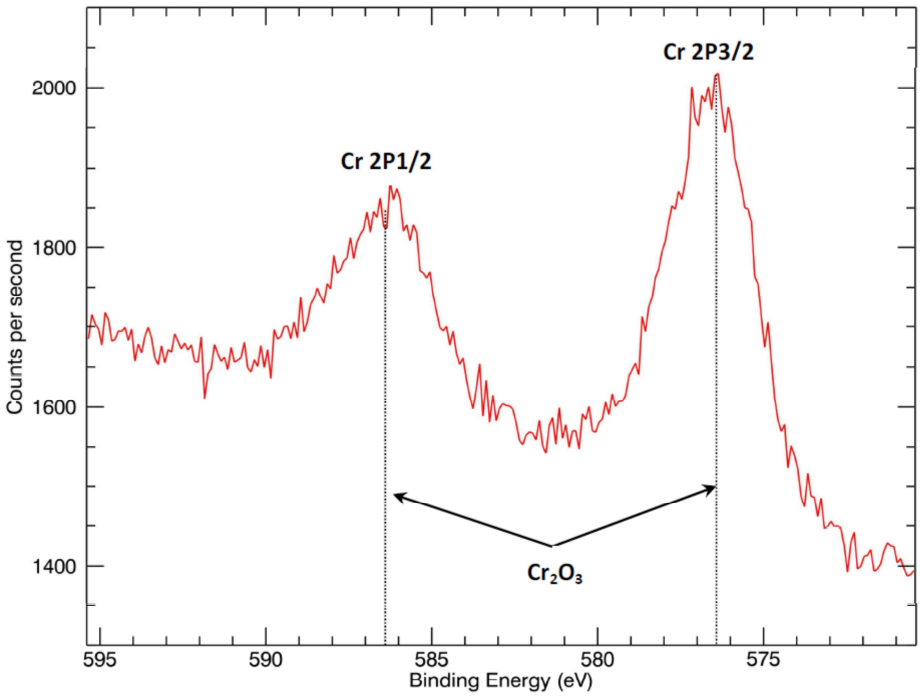

(c)

Figure 4.16. *XPS spectra of the corroded area of steel after a potentiostatic polarization at -1.3 V (vs. Ag/AgCl/KCl) in a 1 M sodium chloride solution. (a) survey spectrum (b) Fe_2O_3 and (c) Cr_2O_3 spectra with the relative references.*

4.2.4.3. Atomic force microscopy

Figure 4.17 depicts the surface morphology of the steel sample after 600 s cathodic polarization at -1 V (a) and -1.7 V (b, c) (vs. Ag/AgCl/KCl) under a 200 µm microcapillary. Similar to Figure 4.9 (Section 4.1), here also applying greater cathodic potential results deeper valleys and higher ridges. In Figure 4.17a the peak heights of the polarized surface after applying -1 V (vs. Ag/AgCl/KCl) cathodic potential is about 80 nm which this reaches to 2000 nm after applying -1.7 V (vs. Ag/AgCl/KCl) (Figure 4.17b). The formed metal nanoparticles during the cathodic polarization are clearly observed in Figure 4.17c. despite the conventional setup, under the capillary setup all produced corrosion products or nanoparticles remain on the surface of the sample.

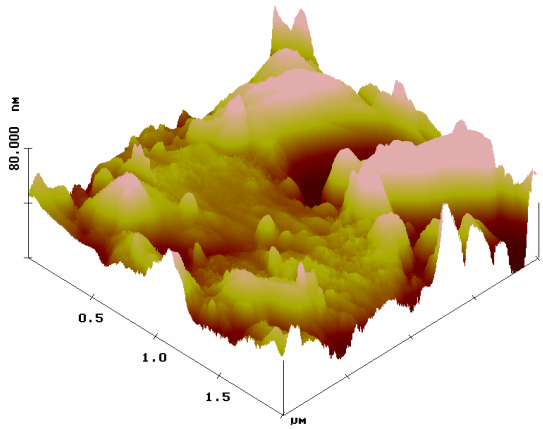

(a)

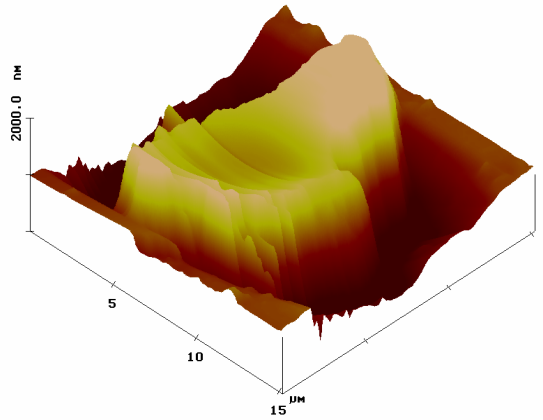

(b)

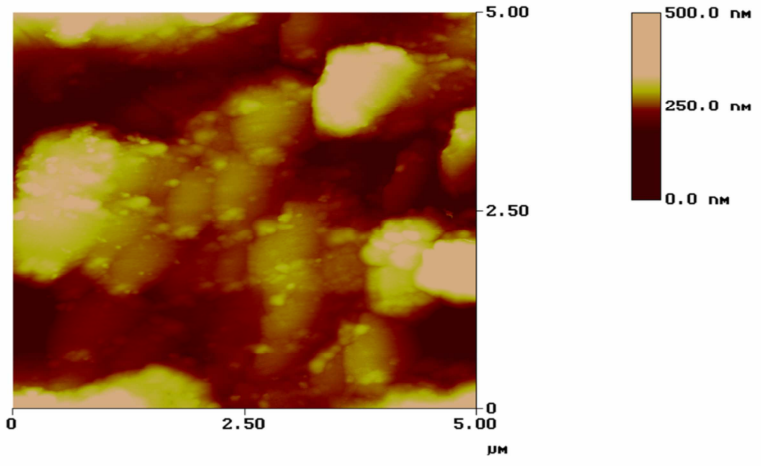

(c)

Figure 4.17. *Atomic force microscopy images of steel (a) after cathodic polarization at -1 V for 600 s, (b,c) with the same duration at -1.7 V vs. Ag/AgCl/KCl.*

4.3. Conclusions

This study investigated the effect of cathodic polarization on the electrochemical corrosion of stainless steel under micro/macro static and macro flow conditions with two different flow regimes. In macro scale level completely opposite effects on the rates of oxygen reduction were found under stagnant and flow conditions produced by the flow cell with vortex flow regime, while the dynamic conditions constructed by the RDE showed similar results with the stagnant conditions only with higher current density. Under static conditions, the cathodic polarization accelerates the mixed charge transfer–mass transfer oxygen reduction process by decreasing the thickness of the diffusion layer at the metal–electrolyte interface. This increases the rate of oxygen reduction reaction during the anodic corrosion of steel and therefore, the higher cathodic current density of the cathodically polarized steel shifts the corrosion potential towards nobler potentials. Under macro scale flow conditions, depending on the flow regime applied over the steel surface during the potentiostatic and potentiodynamic polarization processes the thickness of the diffusion layer may decrease or increase. Similarly the flow regime produced by the RDE reduces the thickness of the diffusion layer during the cathodic polarization process and enhances the rate of the oxygen reduction reaction. This increases the cathodic current density, the corrosion potential and corrosion current density as well. Unlike the RDE, application of the flow regime constructed by the flow cell during the potentiostatic and the potentiodynamic polarizations increases the thickness of the diffusion layer, decreases the cathodic current density and corrosion current density of the Tafel plots and shifts the corrosion potential of steel towards less noble potentials. In all the investigated cases, application of the cathodic polarization results in higher anodic current density and lower pitting potential. These results reveal the key role of the applied flow regime on the corrosion performance of the steel.

On a micro scale however, similar to the macro scale measurements parallel to the increase of the applied cathodic potential, the anodic current density increases after application of cathodic polarization. Also as the macro scale measurements E_{pit} shifts towards less nobler potentials during the anodic dissolution after application of greater cathodic potential because more weak points are generated by absorption of hydrogen over the surface.

In both macro and micro scale measurements part of the produced anodic current density is attributed to the oxidation of the hydrogen atoms which absorb the surface during the cathodic polarization process. Therefore, the total anodic current density of the cathodically polarized steel is the result of the metal dissolution, oxidation of the

absorbed hydrogen and chloride atoms plus the synergistic effect of hydrogen and chloride ions.

The observed results in this work are in good agreement with the results reported by Yang et al. [47], who studied the synergistic effect of hydrogen and chloride ions on the corrosion performance of 304L stainless steel. They also observed that hydrogen and chloride ions increase the anodic current density and also hydrogen enhances the effect of chloride ions on the pitting potential of steel something which supports our observations.

Further attentions must be paid on the pH changes during the cathodic polarization process especially under static conditions.

Bibliography

[1] C. F. Dong, K. Xiao, X. G. Li, Y. F. Cheng, Wear 270 (2010) 39–45.

[2] D. Zheng, D. Che, Y. Liu, Corros. Sci. 50 (2008) 3005–3020.

[3] J. A. Wharton, R. J. K. Wood, Wear 256 (2004) 525–536.

[4] S. Nesic, G. T. Solvi, J. Enerhaug, Corrosion 51 (1995) 773–787.

[5] R. J. K. Wood, S. P. Hutton, D. J. Schiffrin, Corros. Sci. 30 (1990) 1177–1201.

[6] L. Niu, Y. F. Cheng, Wear 265 (2008) 367–374.

[7] B. T. Lu, J. L. Luo, H. X. Guo, L. C. Mao, Corros. Sci. 53 (2011) 432–440.

[8] A. Rauf, E. Mahdi, Int. J. Electrochem. Sci. 7 (2012) 5692–5707.

[9] R. Leiva–García, M. J. Muñoz–Portero, J. García–Antón, R. Sánchez–Tovar, Int. J. Electrochem. Sci. 7 (2012) 1332–1347.

[10] M. T. Montañés, R. Sánchez–Tovar, J. García–Antón, V. Pérez–Herranz, Int. J. Electrochem. Sci. 7 (2012) 747–759.

[11] A. Y. Musa, A. A. H. Kadhum, A. Mohamad, A. Daud, M. Takriff, S. K. Kamarudin, N. Muhamad, Int. J. Electrochem. Sci. 4 (2009) 707–716.

[12] M. A. Deyab, J. Solid State Electrochem. 13 (2009) 1737–1742.

[13] K. Jafarzadeh, T. Shahrabi, A. A. Oskouei, J. Solid State Electrochem. 39 (2009) 1725–1731.

[14] Y. Wang, G. P. Bierwagen, J. Coating Technol. Res. 6 (2009) 429–436.

[15] Y. Liu, Y. F. Cheng, J. Appl. Electrochem. 39 (2009) 1267–1272.

[16] K. Jafarzadeh, T. Shahrabi, S. M. M. Hadavi, M. G. Hosseini, J. Mater. Sci. Technol. 23 (2007) 623–628.

[17] J. M. Pietralik, E–J. Adv. Maint. 4 (2012) 63–78.

[18] J. Villarreal, D. Laverde, C. Fuentes, Corros. Sci. 48 (2006) 2363–2379.

[19] A. S. Shehata, S. A. Nosier, G. H. Sedahmed, Chem. Eng. Proc. 41 (2002) 659–666.

[20] H. Nanjo, Y. Kurata, N. Sanada, K. Miyauchi, R. Ohshima, K. Koike, Wear 186 (1995) 573–578.

[21] Y. Wang, Y. G. Zheng, W. Ke, W. H. Sun, W. L. Hou, X. C. Cheng, J. Q. Wang, Corros. Sci. 53 (2011) 3177–3185.

[22] H. Subramanian, P. Madasamy, H. Kumawat, R. G. Thomas, T. V. Krishnamohan, S. Velmurugan, S. V. Narasimhan, Corros. Sci. 54 (2012) 45–51.

[23] W. H. Ahmed, M. M. Bello, M. E. Nakla, A. Al Sarkhi, Nucl. Eng. Des. 252 (2012) 52–67.

[24] R. Malka, S. Nesic, D. A. Gulino, Wear 262 (2007) 791–799.

[25] X. Wu, H. Jing, Y. Zheng, Z. Yao, W. Ke, Wear 256 (2004) 133–144.

[26] X. X. Yuan, M. D. Pandey, G. A. Bickel, Nucl. Eng. Des. 238 (2008) 16–24.

[27] R. C. Barik, J. A. Wharton, R. J. K. Wood, K. S. Tan, K. R. Stokes, Wear 259 (2005) 230–242.

[28] X. Hu, R. Barker, A. Neville, A. Gnanavelu, Wear 271 (2011) 1295–1301.

[29] H. Zhu, Y. Lin, D. Zeng, Y. Zhou, J. Xie, Y. Wu, Eng. Fail. Anal. 22 (2012) 83–91.

[30] V. Kain, S. Roychowdhury, P. Ahmedabadi, D.K. Barua, Eng. Fail. Anal. 18 (2011) 2028–2041.

[31] K. H. Kim, S. H. Park, K. M. Hwang, Microsyst. Technol. 16 (2010) 1945–1950.

[32] H. X. Guo, B. T. Lu, J. L. Luo, Electrochim. Acta 51 (2005) 315–323.

[33] G. A. Gehring, M. H. Peterson, Corrosion 37 (1981) 232–242.

[34] D. M. G. García, E. B. Tamarit, J. García–Antón, Int. J. Electrochem. Sci. 6 (2011) 1237–1249.

[35] F. L. LaQue, Marine Corrosion, Wiley, New York (1975).

[36] M.G. Fontana, Corrosion Engineering, 3rd ed., McGraw–Hill, Singapore (1987).

[37] R. E. Weyers, Techniques to Assess the Corrosion Activity of Steel Reinforced Concrete Structures, N. S. Berke, E. Escalante, C. K. Nmai, D. Whiting (Eds.), American Society for Testing and Materials (ASTM), Baltimore (1996) p. 3–22.

[38] H. W. Pickering, R. P. Frankenthal, J. Electrochem. Soc. 119 (1972) 1297–1304.

[39] L. J. Qiao, W. Y. Chu, C. M. Hsiao, Scr. Metall. 22 (1988) 627–630.

[40] L. J. Qiao, J. L. Luo, X. Mao, Corrosion 54 (1998) 115–120.

[41] Y. P. Kim, M. Fregonese, H. Mazille, D. Feron, G. Santarini, Corros. Sci. 48 (2006) 3945–3959.

[42] W. J. Lee, S. I. Pyun, Mater. Sci. Eng. A 279 (2000) 130–137.

[43] R. Nishimura, H. Habazaki, A. Kawashima, K. Asami, K. Hashimoto, Mater. Sci. Eng. A 25 (1991) 1074–1077.

[44] M. Hasegava, M. Osawa, Corrosion 39 (1983) 115–119.

[45] Q. Yang, L. J. Qiao, S. Chiovelli, J. L. Luo, Corrosion 54 (1998) 628–633.

[46] H. Yashiro, B. Pound, N. Kumagai, K. Tanno, Corros. Sci. 40 (1998) 781–791.

[47] Q. Yang, J. L. Luo, Electrochim. Acta 45 (2000) 3927–3937.

[48] P. Rodriguez, F. D. Tichelaar, M. T. M. Koper, A. I. Yanson, J. Am. Chem. Soc. 133 (2011) 17626–17629.

[49] P. Eaton, P. West, Atomic Force Microscopy, Oxford Univ. Press, Oxford (2010).

[50] M. Baune, V. Breunig–Lyriti, P. J. Plath, Int. J. Bifurcation Chaos 12 (2002) 2835–2845.

[51] C. A. Real–Ramirez, R. M. Tello, L. F. H. Reyes, J. I. G. Trejo, , Int. J. Chem. Reac. Eng. 8 (2010) 1–48.

[52] J. O. M. Bockris, D. Drazic, Electrochim. Acta 7 (1962) 293–313.

[53] L. Caceres, T. Vargas, L. Herrera, Corros. Sci. 49 (2007) 3168–3184.

[54] Y. Miyata, S. Asakura, Corros. Sci. 44 (2002) 589–602.

[55] A. Davydov, K. V. Rybalka, L. A. Belketaeva, G. R. Engelhardt, P. Jayaweera, D. D. MacDonald, Corros. Sci. 47 (2005) 195–215.

[56] J. N. Harb, R. C. Alkire, Corros. Sci. 29 (1989) 31–43.

[57] M. Kliskic, J. Radosevic, S. Gudic, M. Smith, Electrochim. Acta 43 (21–22) (1998) 3241–3255.

[58] M. C. Li, Y. F. Cheng, Electrochim. Acta 52 (2007) 8111–8117.

[59] Y. F. Cheng, L. Niu, Electrochem. Comm. 9 (2007) 558–562.

[60] P. V. Mahalakshmi, S. C. Vanithakumari, J. Gopal, U. K. Mudali, B. Raj, Current Sci., 101 (2011) 1328–1336.

[61] ASTM E 112–Standard Test Methods for Determining Average Grain Size, 229–251 (NTU).

[62] D. P. Woodruff, T. A. Delchar, Modern Techniques in Surface Science, Cambridge Univ. Press, New York (1986).

Chapter 5

Investigation of the corrosion behavior of copper in NaCl solution in micro and macro scales

5.1. Introduction

It is known that the corrosion mechanism of copper is strongly dependent on the presence of chloride ions. Several attempts to describe the corrosion mechanism of copper in different chloride containing media have been reported in the literature [1–10]. The main differences among the available models are the descriptions of the initial electrodissolution reactions of the bare copper. Three reversible mechanisms have been considered (Eq. 2.41–2.43).

This study investigates the electrochemical corrosion of copper in macro and micro systems in various NaCl solutions using two different corrosion cells constructed by a conventional large scale electrochemical cell and a microcapillary electrochemical droplet cell. Ranges of pH and chloride concentration promoting local and global corrosion of unalloyed copper are examined, as are conditions promoting breakdown of the passive oxide film.

Linear sweep voltammetry and chronoamperometry are used to determine electrochemical surface plots for copper in NaCl, at both the micro and macro scales. An experimental design strategy known as central composite design (CCD) was implemented to minimize the number of experiments required, and additionally determine which variable (pH or NaCl concentration) has the greater influence on the corrosion of copper. Furthermore, this design strategy was able to reveal correlations between the pH and NaCl concentration.

5.2. Experimental

5.2.1. Chemicals

Sodium chloride solutions were prepared using analytical grade NaCl powder (Fluka). The prepared concentrations and pH values ranged from 0.01 to 5 M and 3 to 11, respectively. The pH was measured using a digital pH meter (ORION, model: 420 A) and adjusted with NaOH (4 M) or HCl (37%) purchased from Fluka as necessary. The total volume of each solution was 50 mL, of which 10 mL was used for the measurements.

5.2.2. Specimen and surface preparation

All experiments were performed on pure copper coupons with a diameter of 12.5 mm and a thickness of 2 mm (Goodfellow Cambrige Ltd., 99.9% purity, temper: half hard). The coupons were ground with silicon carbide paper down to 600 grit and then polished with a polishing cloth (MicroCloth, Buehler) using 1.0 μm and 0.5 μm alumina in sequence. Finally, samples were washed with distilled water and rinsed ultrasonically in ethanol for 5 minutes.

5.2.3. Electrochemical setup

The electrochemical setups used in this work are the same as the previous chapters.

A microcapillary cell was used for micro measurements. For the macro scale measurements a conventional electrochemical setup was used.

The potentiodynamic polarization measurements were performed using linear sweep voltammetry, in the potential range of -1 to 1 V (vs. Ag/AgCl/KCl) with a scan rate of 10 and 1 $mV.s^{-1}$ for the micro scale and macro scale measurements, respectively. The high scan rate for the micro scale measurements was selected to avoid leakage of the microcapillary (Section 1.5.2.3). The potentiostatic measurements were performed at a potential higher than the corrosion potential of copper (250 mV (vs. Ag/AgCl/KCl)) with a duration of 200 s for both micro and macro systems.

5.2.4. Experimental design

A Box–Wilson central composite design [11] was implemented in order to design a short series of experiments to study the pitting potential, corrosion potential, and stabilized passive current of copper in sodium chloride solution. A wide range of concentrations (0.01 to 5 M) and pH values (3 to 11) was investigated at both the micro and macro scales. The central composite design enables an analysis of the correlation between these factors and reveals likely interactions between pH and sodium chloride concentration. The polynomial equations, response surface, and central design for a particular response were obtained using the statistical software package Essential Regression 97 [12, 13]. For an experimental design with two factors, the model includes linear, quadratic, and cross terms that may be expressed as follows:

$$Response = b_0 + b_1 \times F_1 + b_2 \times F_2 + b_3 \times F_1 \times F_1 + b_4 \times F_2 \times F_2 + b_5 \times F_1 \times F_2 \qquad (5.1)$$

The response is either the pitting potential (E_{pit}), the corrosion potential (E_{corr}), or the passive current (i_{pass}). F_1 and F_2 are the variable parameters (NaCl concentration and pH, respectively), and b_0 through b_5 are the coefficient values obtained through a multivariate linear regression. The term b_0 indicates the intercept, which is used in calculating the error. The statistical significance of the predicted model was evaluated by an analysis of variance (ANOVA) and least square technique. Replicates (n = 4) of the central points were performed to estimate the experimental error.

5.3. Results and discussion

5.3.1. Potentiodynamic and potentiostatic measurements

Figure 5.1 shows a typical potentiodynamic polarization curve of pure copper in 3.82 M NaCl (pH = 9.8) taken at the micro scale level, where the two peaks represent the formation of Cu(I) and Cu(II). The figure also shows the pitting potential, which is the potential where the pitting starts, and is indicated by a rapid rise in the oxidation current.

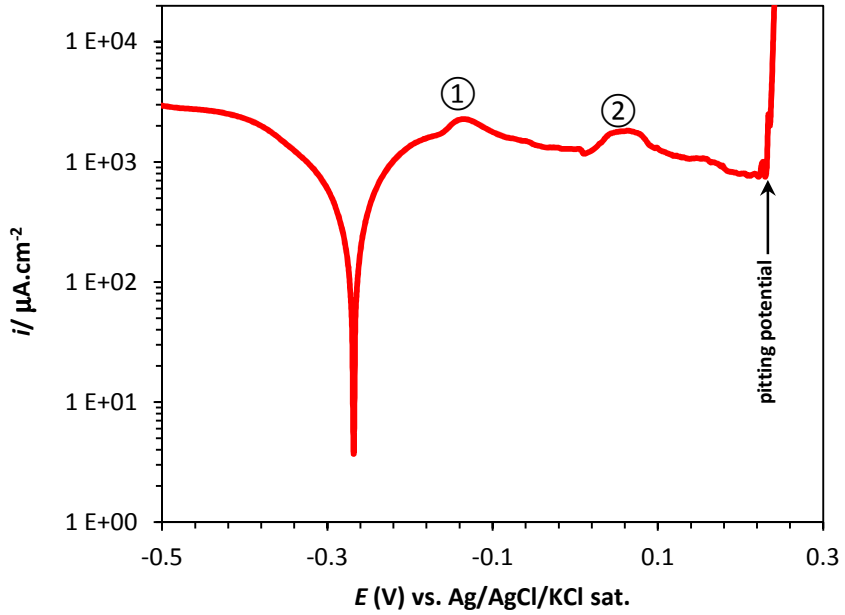

Figure 5.1. *Potentiodynamic polarization curve of pure copper in 3.82 M NaCl (pH = 9.8) obtained using a microcapillary with a tip diameter of ~100 µm. The numbers 1 and 2 indicate the position of the peaks representing the formation of Cu(I) and Cu(II), respectively.*

Figure 5.2a shows similar curves taken at different pH values (acidic, neutral, and alkaline). In all cases, peaks 1 and 2 can be clearly identified, which is not the case when using a conventional macro scale setup. In the latter case, two separate anodic peaks can only be distinguished at highly alkaline pH values [14].

Figure 5.2a–d also shows the variations of the pitting and corrosion potential of copper parallel to the variations of the pH and the NaCl concentration at the micro and macro scale. At the micro scale, the pitting potential of copper decreases from 546 to 270 mV (vs. Ag/AgCl/KCl) with increasing pH values (3, 7, and 11, respectively) (Figure 5.2a). Higher concentrations of NaCl in neutral pH (7) result in increasingly lower pitting potentials for copper (Figure 5.2c).

The macro scale potentiodynamic polarization curves of copper in Figures 5.2b,d reveal a very short passive area in the anodic region, especially for high chloride concentrations. The passive area before the pit nucleation (and therefore the pitting potential) is detectable only for low chloride concentrations (0.01 M). The E_{corr} value shifts towards more negative potentials as the chloride concentration is increased.

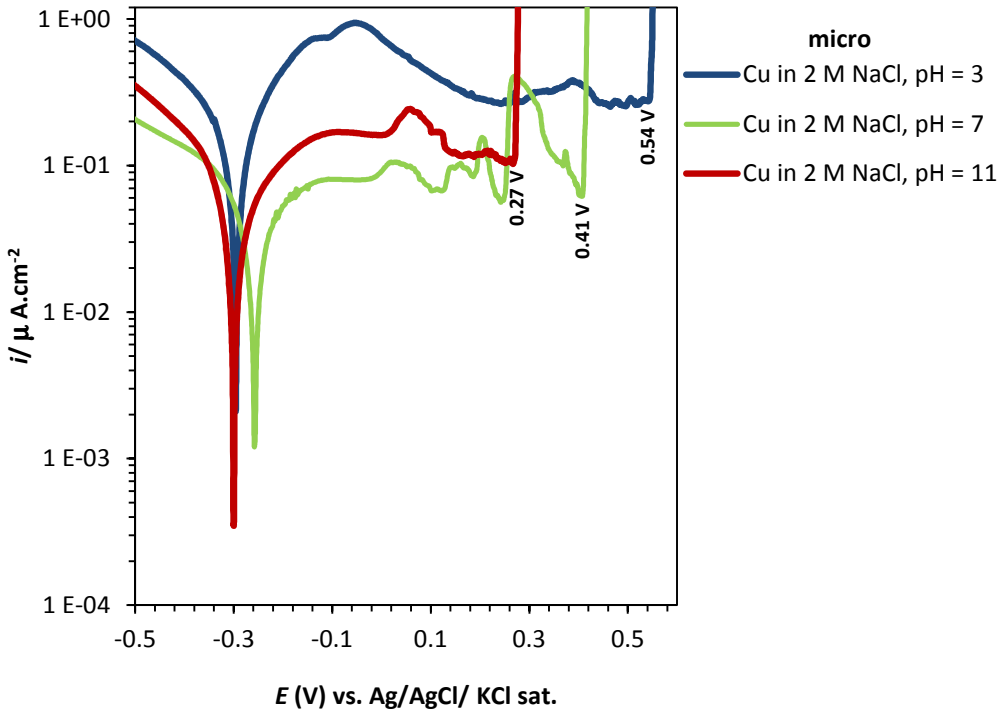

(a)

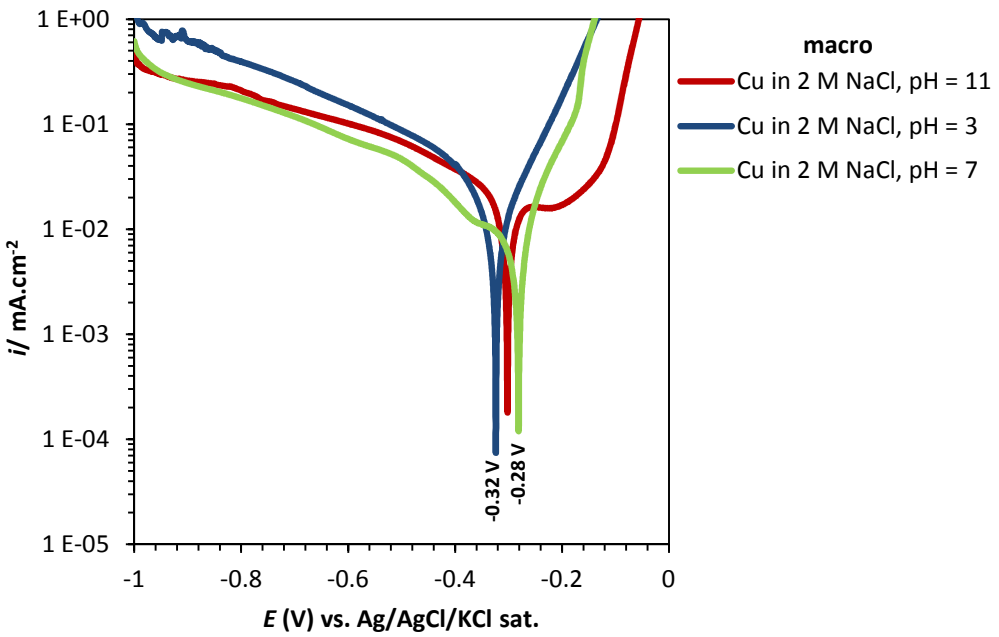
1 E+00
1 E-01
1 E-02
1 E-03
1 E-04
1 E-05
i/ mA.cm-2
-1
-0.8
-0.6
-0.4
-0.2
0
E (V) vs. Ag/AgCl/KCl sat.
-0.32 V
-0.28 V
macro
Cu in 2 M NaCl, pH = 11
Cu in 2 M NaCl, pH = 3
Cu in 2 M NaCl, pH = 7

(b)

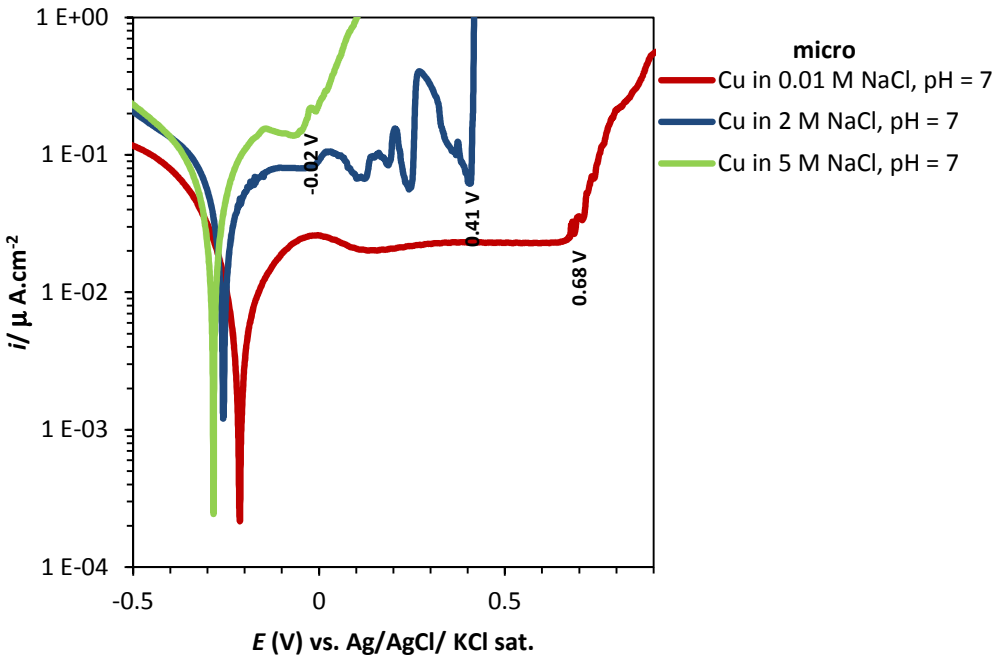
1 E+00
1 E-01
1 E-02
1 E-03
1 E-04
i/ µ A.cm-2
-0.5
0
0.5
E (V) vs. Ag/AgCl/ KCl sat.
-0.02 V
0.41 V
0.68 V
micro
Cu in 0.01 M NaCl, pH = 7
Cu in 2 M NaCl, pH = 7
Cu in 5 M NaCl, pH = 7

(c)

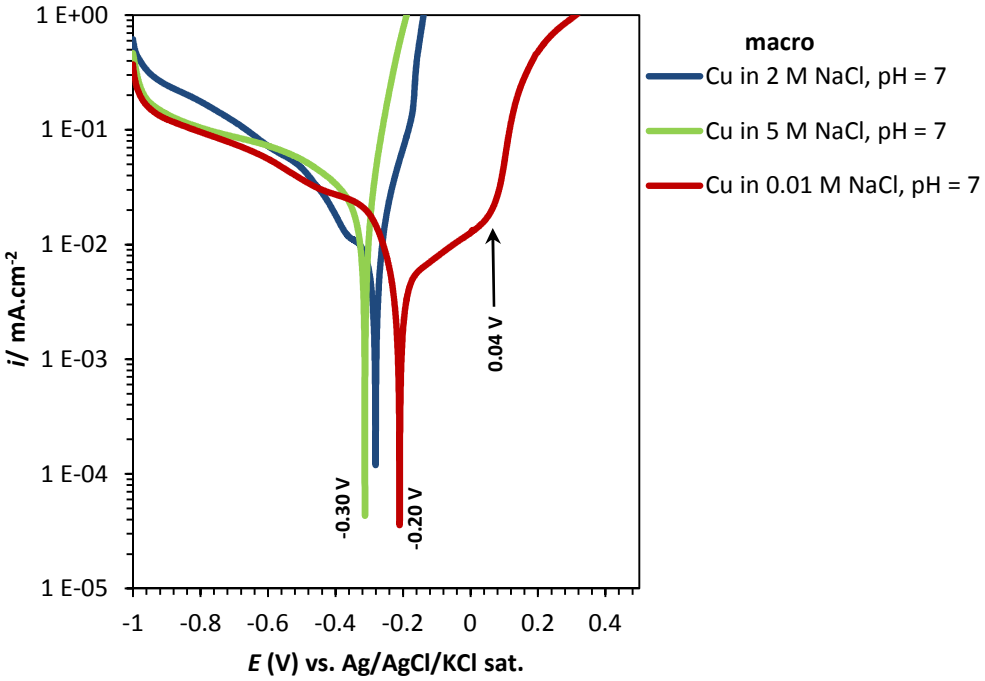

(d)

Figure 5.2. *Potentiodynamic polarization curves of pure copper for various (a, b) pH values and (c, d) NaCl concentrations at both micro and macro scales. The tip diameter of the used microcapillary is ~100 μm.*

Figure 5.3a–d shows the potentiostatic polarization curves of copper in NaCl for different pH values and different chloride concentrations in micro (a and c) and macro (b and d) systems. At the micro scale, i_{pass} of copper shows a sharp decrease at neutral pH (7) whilst the values at acidic and alkaline pH are higher (Figure 5.3a). In addition, higher NaCl concentrations show higher passive current densities for the micro system (Figure 5.3c). Figure 5.3b,d shows that higher i_{pass} values are obtained at neutral and acidic pHs and higher chloride concentrations, and that changes in pH have no significant effect on the response in acidic and neutral pHs.

In this figure the initial current density is due to the dissolution of copper to cuprous cations that react in turn with Cl^- ions from the solution and form CuCl and further $CuCl_2^-$. The decreases in the current density with time are due to the formation of a porous oxide layer (Cu_2O). The formation of the oxide layer provides partial protection and does not allow the current to increase.

The corrosion of copper with an oxide film typically starts with the removal of the passive oxide layer, followed by oxidation of the copper to different oxidation states. This process forms corroded pits, which are detected through the rapid increase of the

oxidation current. Figures 5.2a, 5.2c, 5.3a and 5.3c therefore suggest that in micro scale systems the pit corrosion of pure copper in sodium chloride solutions occurs more readily at higher NaCl concentrations and alkaline pH values; however, the passive current of oxide film breakdown is higher at acidic pH and high NaCl concentrations. In macro scale systems the corrosion parameters of copper are dominated by the chloride concentration.

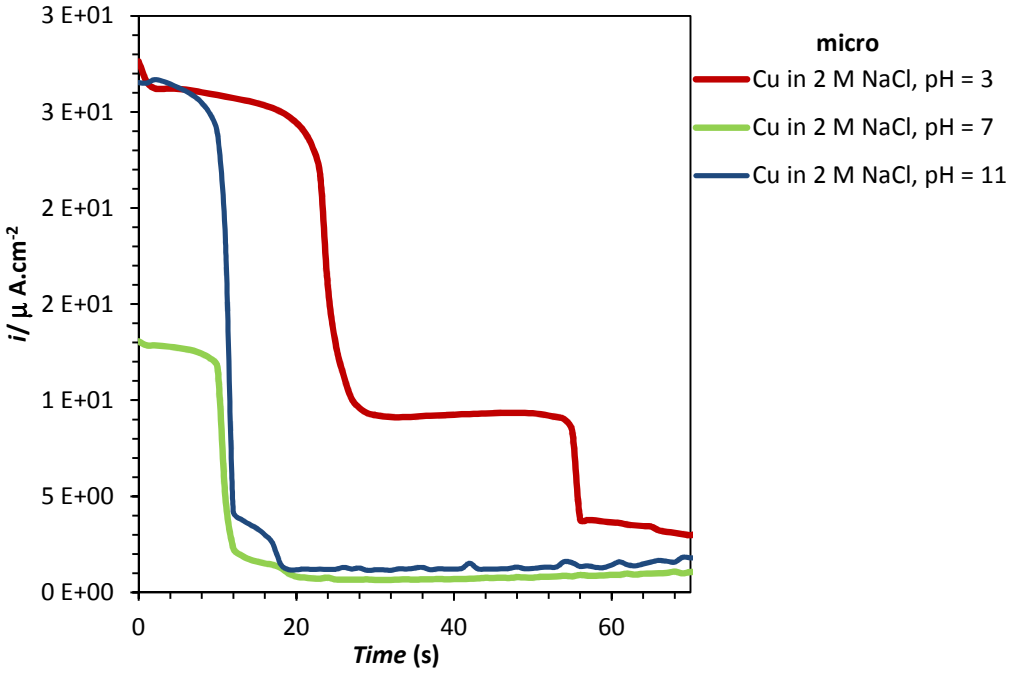

(a)

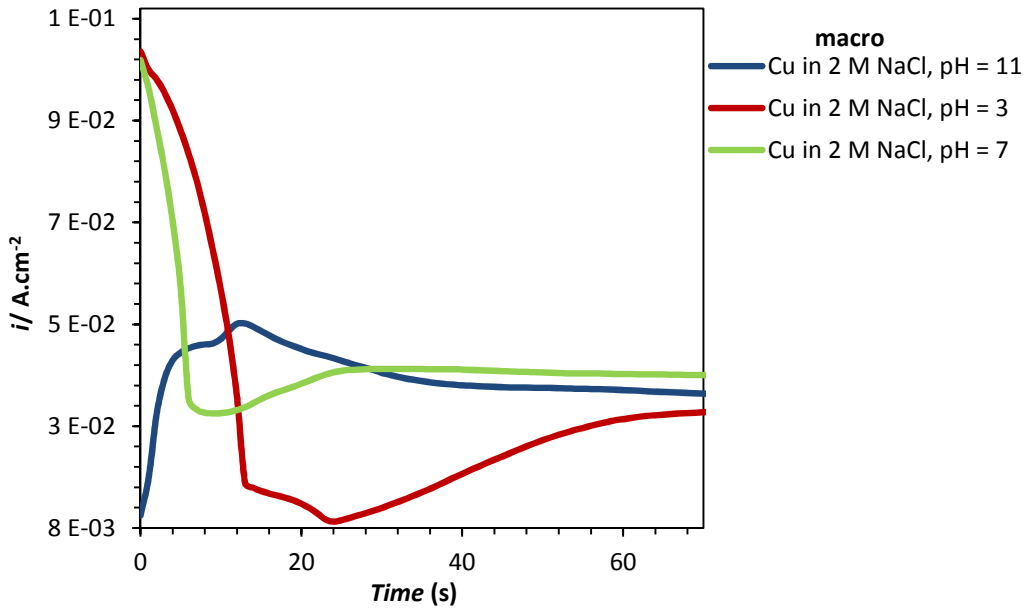

(b)

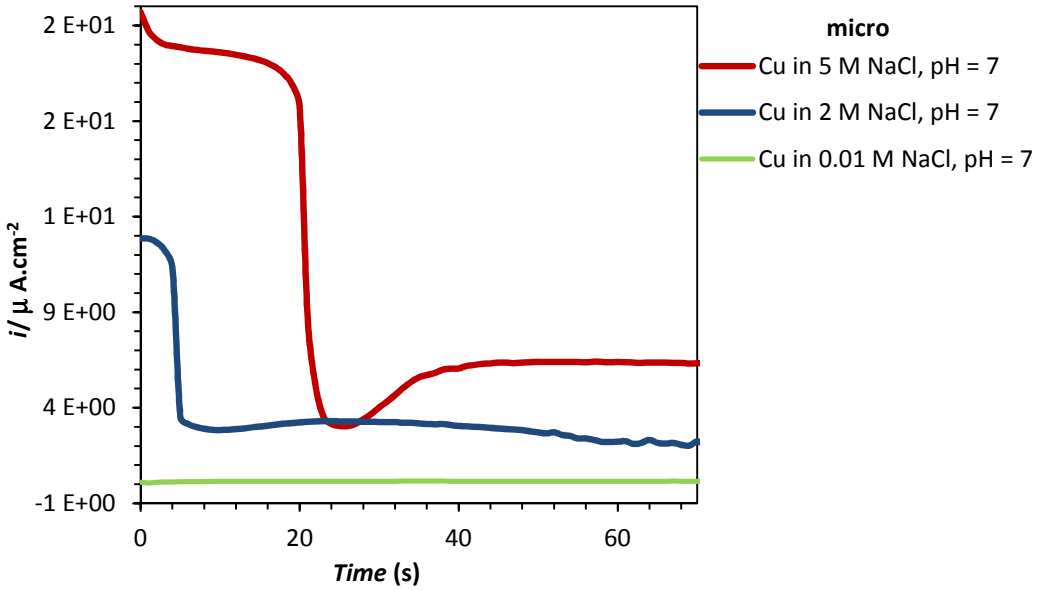

(c)

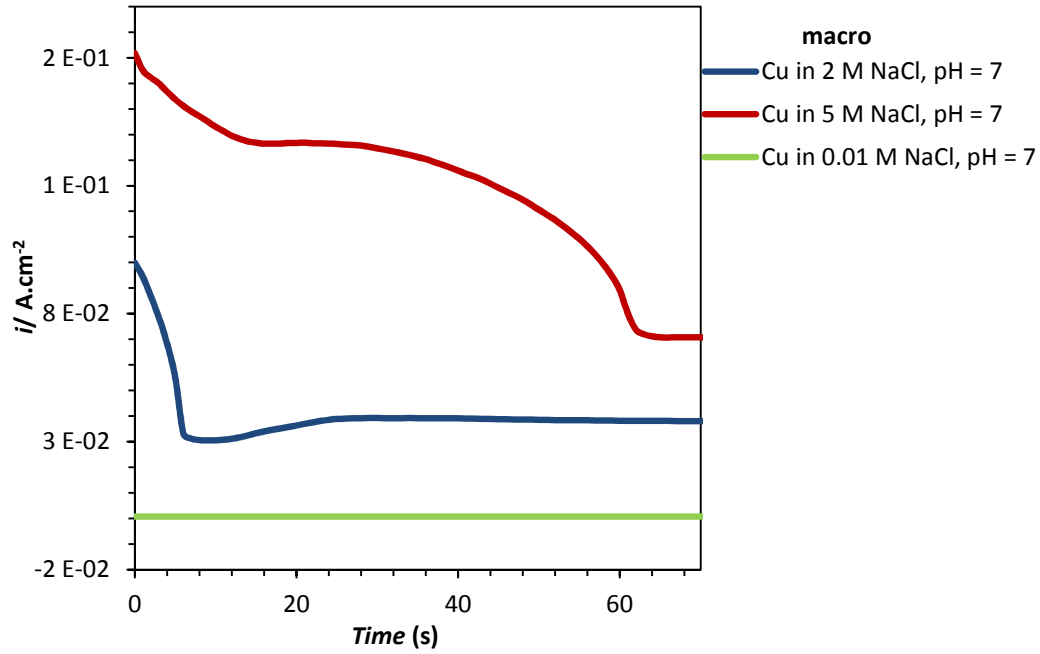

(d)

Figure 5.3. *Potentiostatic polarization curves of pure copper for various (a, b) pH values and (c, d) NaCl concentrations at both micro and macro scales. The tip diameter of the used microcapillary is ~100 µm.*

5.3.2. Central composite design

Two main questions remain. Which factor is more significant in each system? What is the correlation between these two factors? To answer these questions, an experiment was designed using the central composite design method in order to create a clear surface map of the $E_{corr(macro)}$, $E_{pit(micro)}$ and $i_{pass(micro/macro)}$ variations versus pH and sodium chloride concentration. The significance of each variable was investigated. This central composite design consists of 12 measurements for each response ($E_{pit(micro)}$, $E_{corr(macro)}$ and $i_{pass(micro/macro)}$). Table 5.1 shows the levels of the coded and actual experimental variables that were tested, and the corresponding response of each experiment.

Table 5.1. *Design matrix and relative E_{pit}, i_{pass} and E_{corr} values in macro and micro systems in the central composite design for two factors: NaCl concentration (molar) and pH. The letter "a" in the experiment column indicates the replicate measurements.*

Experiment	**F_1: [NaCl] (M)**	**F_2: pH**	**$E_{pit(micro)}$ (V)**	**$E_{corr(macro)}$ (V)**	**$i_{pass(micro)}$ ($\mu A.cm^{-2}$)**	**$i_{pass(macro)}$ ($A.cm^{-2}$)**
1	0	2	0.186	-0.302	26.5	0.0105
2	0	-2	0.167	-0.324	27.15	0.102
3[a]	0	0	0.41	-0.281	13.1	0.099
4	1.414	-1.414	0.374	-0.31	44.35	0.142
5	2	0	-0.063	-0.313	24.7	0.182
6[a]	0	0	0.364	-0.287	12.9	0.0864
7[a]	0	0	0.373	-0.28	12.9	0.0946
8	-1.414	1.414	0.539	-0.247	7.83	0.0314
9	-1.414	-1.414	0.311	-0.239	9	0.0327
10	-2	0	0.781	-0.210	0.102	0.0007
11	1.414	1.414	0.241	-0.332	22.65	0.163
12[a]	0	0	0.396	-0.262	13.25	0.08
Coded value (-2)	*0.01*	*3*	–	–	–	–
Coded value (-1)	*0.59*	*4.1*	–	–	–	–
Coded value (0)	*2*	*7*	–	–	–	–
Coded value (+1)	*3.828*	*9.8*	–	–	–	–
Coded value (+2)	*5*	*11*	–	–	–	–

Figures 5.4a and 5.4c show respectively the response surface plots of the pitting potential and the stabilized passive current of copper versus pH and the NaCl concentration on the micro scale level.

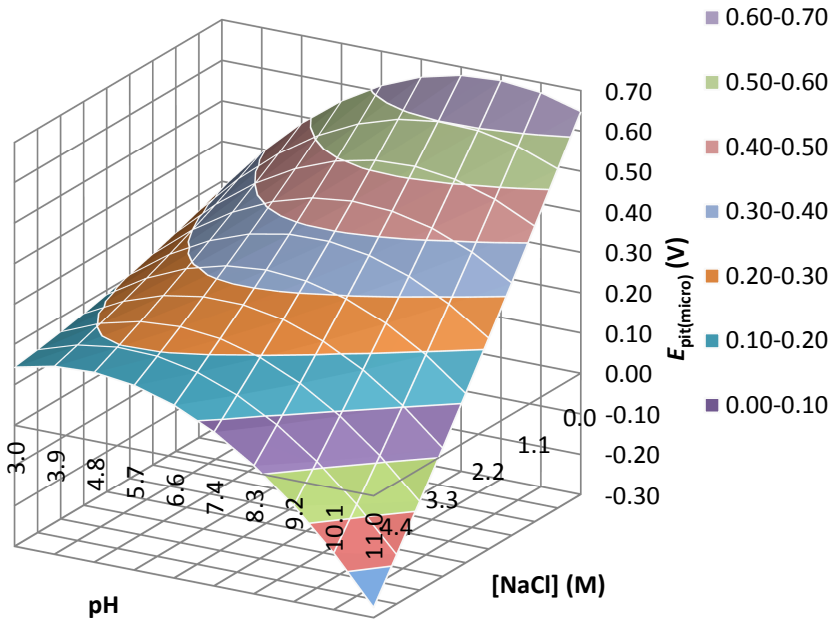

(a)

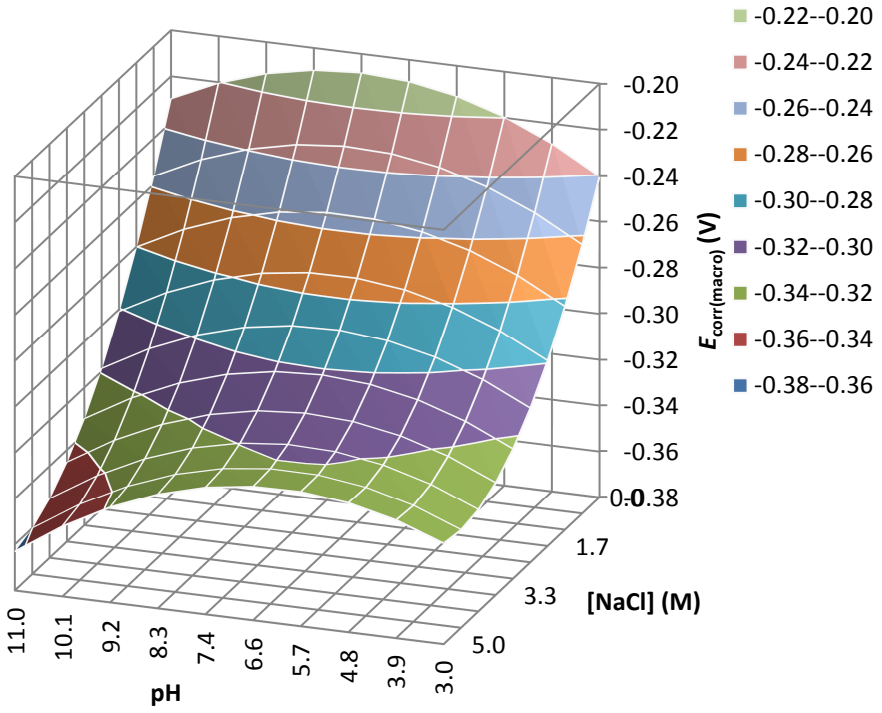

(b)

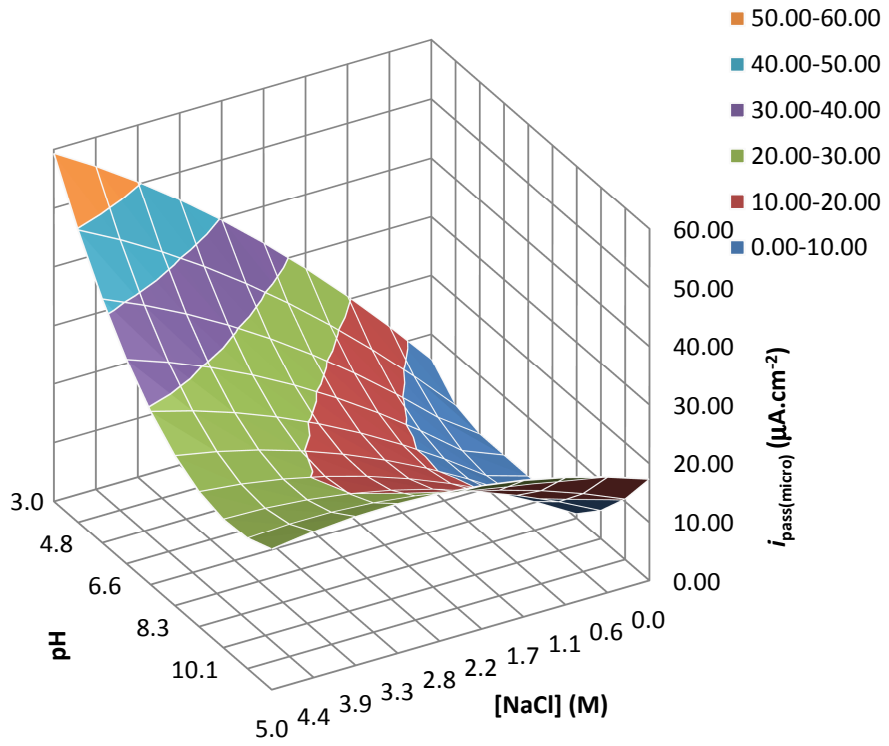

(c)

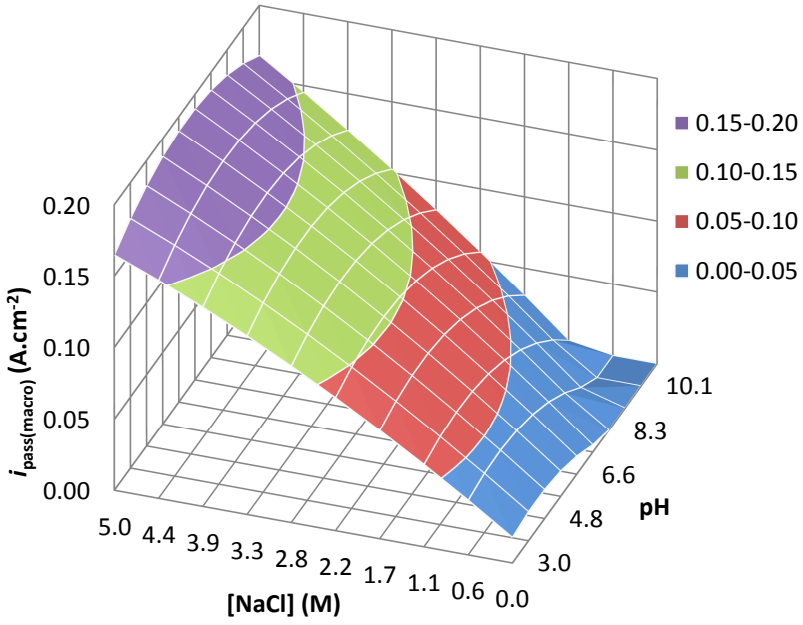

(d)

Figure 5.4. *Response surface plots obtained from the central composite design by plotting pH vs. NaCl concentration for (a) E_{pit} and (b) E_{corr} of copper at the micro and macro scale, and (c) and (d) i_{pass} of copper at the micro and macro scales respectively.*

The pitting potential surface plot (Figure 5.4a) demonstrates that the most corrosive medium for copper is a high NaCl concentration (~5 M) and a highly alkaline pH (~11) where E_{pit} = -0.3 to -0.2 V (vs. Ag/AgCl/KCl). The highest pitting potential, on the other hand, is observed at neutral pH values and low chloride concentrations (E_{pit} = 0.6 to 0.7 V (vs. Ag/AgCl/KCl). Figure 5.4c shows the highest passive current density for acidic pH values (pH = 3) and high chloride concentrations (~5 M). The passive current density increases at low NaCl concentration (<0.5 M) as the pH increases (up to 11).

Figure 5.4b,d shows the variation of E_{corr} and i_{pass}, respectively, against pH and NaCl concentration at the macro scale. The lowest corrosion potential is observed at high chloride concentrations (~5 M) and highly alkaline pH (~11). This is similar to the E_{pit} variation observed at the micro scale. The highest i_{pass}, however, was observed at high chloride concentrations over a wide range of pH values.

The *p*–values obtained from the ANOVA are shown in Table 5.2. In statistical analyses, *p*–values are the most commonly used tool to measure evidence against a hypothesis model. The *p*–value is a probability, with a value ranging from 0 to 1 indicating the possibility of observing a difference between the real value and the estimated value [15]. Factors with lower *p*–value are therefore more significant.

Table 5.2. *p–values for each response.*

coefficient	$E_{pit(micro)}$	$i_{pass(micro)}$	$E_{corr(macro)}$	$i_{pass(macro)}$
b_0	0.647	0.029	0.000	0.905
b_1	0.910	0.003	0.021	0.238
b_2	0.119	0.005	0.017	0.479
b_3	0.894	0.200	0.024	0.632
b_4	0.189	0.002	0.018	0.240
b_5	0.260	0.002	0.496	0.540

Table 5.2 shows that in the case of the micro scale pit initiation of copper, the obtained *p*–values for factors F_1 and F_2 are 0.910 and 0.119, respectively. This confirms a greater influence of pH variation on the pitting potential of copper. The second lowest *p*–value (0.189) was observed for the fifth term (b_4 × pH × pH). At the micro scale, the *p*–values for the passive current are 0.003 and 0.005 for the first and second factors, respectively. This suggests that the influence of the NaCl concentration and pH on the response is approximately equivalent. In this case the lowest *p*–values (0.002) were observed for the interaction between the second factor (b_4 × pH × pH) and the interaction of the first and second factors (b_5 × pH × [NaCl]). The *p*–value for pH itself (0.005) was also significant. On the macro scale, the *p*–values for E_{corr} show a

higher significance for pH (*p*–value: 0.017). Here also the second important term is pH × pH (*p*–value: 0.018) and the third important term is NaCl concentration (*p*–value: 0.021). In the case of $i_{pass(macro)}$ the NaCl concentration shows a high significance (*p*–value: 0.238). It can be concluded that pH has a greater influence on the E_{corr} variations, although the response variation shows a steeper slope on the NaCl axis at the macro scale.

A potential–pH diagram of copper in NaCl solution may be useful to investigate the composition of the corrosion products of copper at different pH values. Figure 5.5 represents the Pourbaix diagram of copper as reported by Alfantazi in 2009 [14]. It demonstrates that the major copper corrosion products in NaCl media from acidic pH to neutral pH depend on the applied potential and are either $CuCl_2^-$ or Cu^{2+}, while for alkaline pH values (~7–14) Cu_2O and CuO represent the majority of the corrosion products. Finally, at pH values higher than 14 and potentials higher than 0 V/SHE, CuO_2^{2-} is the only expected compound of copper corrosion.

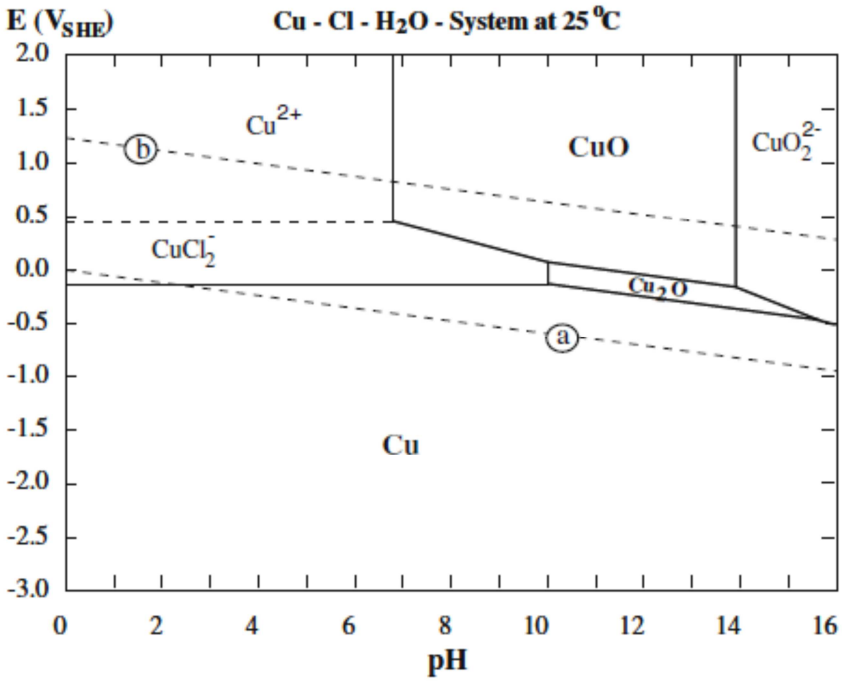

Figure 5.5. *Potential–pH (Pourbaix) diagram of pure copper in the presence of 1 M NaCl solution. The potentials are versus standard hydrogen electrode and the lines a and b indicate the domain of thermodynamic stability of water [14]. (With permission from Elsevier).*

5.3.3. Surface morphology

The surface morphology of the various copper samples after potentiodynamic polarization is shown in Figure 5.6 both for the macro scale (a and b) as for the micro

scale (c). Comparison of the corroded layers between images number 8, 9 and 11 in Figure 5.6 (a and b) reveals that it is mostly chloride concentration which changes the surface morphology of the formed patina. In the almost saturated concentration of 5.0 M, a thick layer of patina covers the surface (Figure 5.6 (a and b), image 5), while in the 0.01 M solution a thin patina layer is formed in parts of the sample (Figure 5.6 (a and b), image 10). Moreover, strangely in the 0.59 M solution, in both acidic and alkaline pH values (Figure 5.6 (a and b), images 8 and 9) the formed patina layers on the copper surface show a different morphology with large grains. In addition, for images 2, 4 and 11 (Figure 5.6b) inflated points under the patina are observed, which is attributed to the formed gas bubbles during the anodic polarization of the surface. In the micro images some differences in the patina morphology are observed. For instance images 5c and 11c show different shapes of patinas compared to the macro images. However, as macro images, here also, the general morphology of the formed patinas under the microcapillary supports the idea that it is chloride concentration which has the more significant role in surface morphology of the corroded copper.

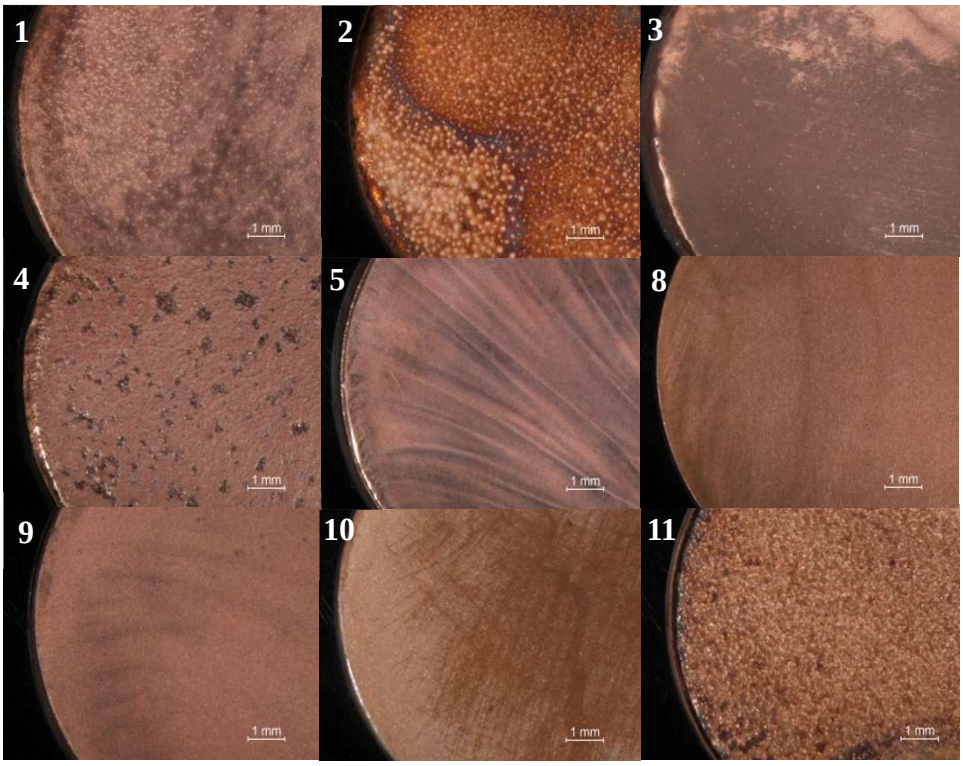

(a)

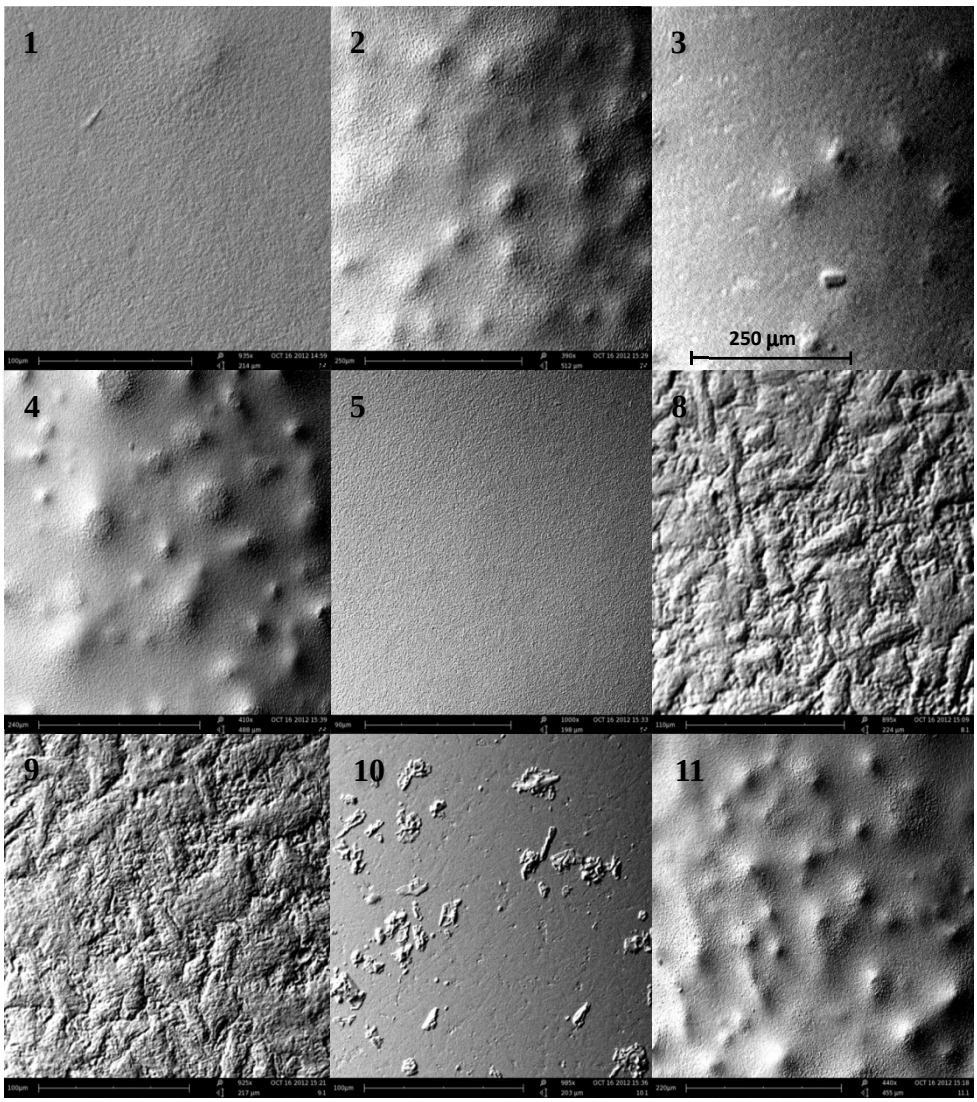

(b)

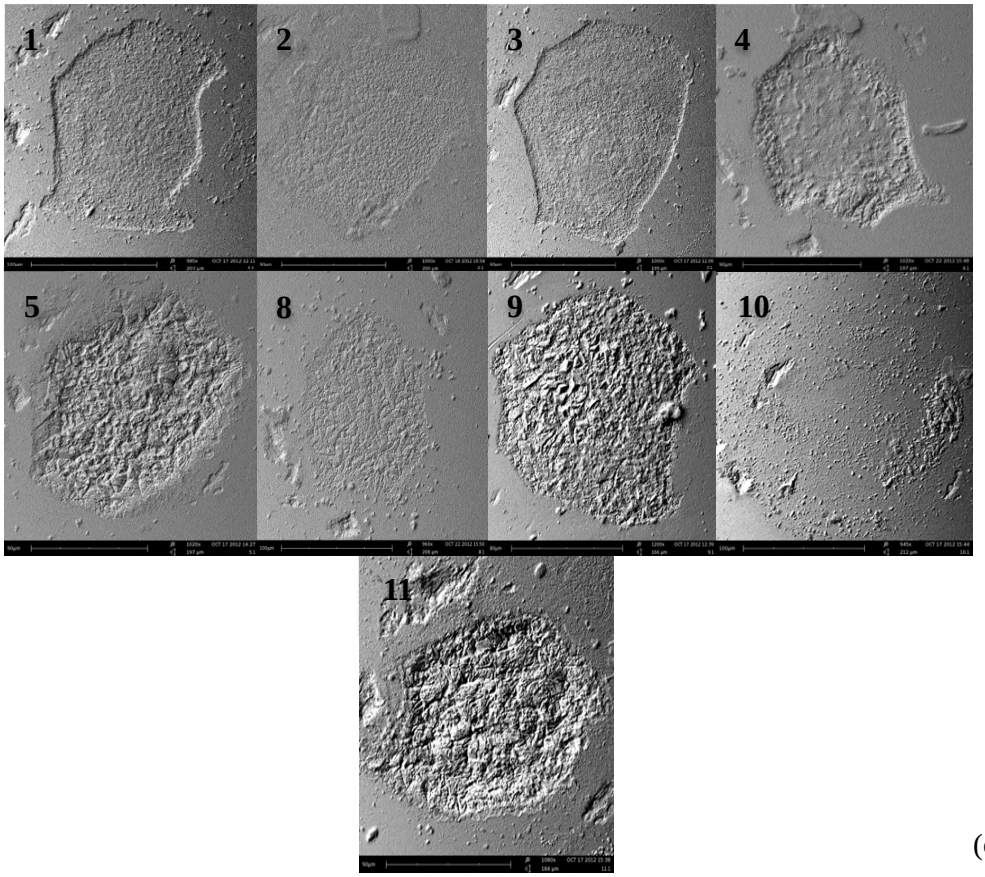

(c)

Figure 5.6. *(a) Optical images of the anodically polarized pure copper in various NaCl solutions (different concentrations and pH values) on a macro scale; (b) related SEM images and (c) SEM images of the corroded copper samples using a microcapillary cell. The numbers indicate the designed experiments mentioned in Table 5.1. Scan rate: macro: 1 and micro 10 mV.s^{-1}. Tip diameter of the used microcapillary: ~100 μm.*

5.4. Conclusions

A capillary–based microdroplet cell and a conventional large scale copper disc electrode were used to study the variation of some corrosion parameters of copper versus the concentration of the electrolyte and pH in sodium chloride solution. The combination of chemometrics and electrochemical data obtained by the micro and macro scale measurements was used to model the corrosion parameters of copper. The influence of two factors (chloride concentration and pH) at the micro and the macro scales was compared. Surface plots were obtained based on the recorded electrochemical data after performing an essential regression by minimum amounts of the measurements required. Using these plots, one can estimate the $E_{corr(macro)}$, $E_{pit(micro)}$ and $i_{pass(micro/macro)}$ of copper for a wide range of pH and NaCl concentration values. The obtained models show that due to the different corrosion environments provided by the micro and the macro scale setups the electrochemical responses of the corrosion of copper have different intensities. Here also higher oxygen concentration under the

microcapillary causes more corrosion of copper compared to the large scale cell. This directly affects the corrosion parameters investigated by the two systems and can be easily observed through the 3D models constructed.

Bibliography

[1] G. Kear, F. C. Walsh, D. B. Barker, K. S. Stokes, Electrochemical corrosion characteristics of copper in filtered and artificial seawater as a function of mass transfer conditions. In EuroCorr. 2000; Institute of Corrosion: Leighton Buzzard, UK, (2000).

[2] J. Mathiyarasu, N. Palaniswamy, V. S. Muralidharan, J. Chem. Sci. 111 (1999) 377–386.

[3] M. Georgiadou, R. Alkire, J. Appl. Electrochem. 28 (1998) 127–134.

[4] D. Wagner, H. Peimemann, H. Siedlarek, S. A. Campbell, N. Campbell, F. C. Walsh, Development in Marine Corrosion; The Royal Society of Chemistry, Cambridge (1998).

[5] F. King, M. J. Quin, C. D. Litke, J. Electroanal. Chem. 385 (1995) 45–55.

[6] F. B. Mansfeld, G. Liu, H. Xiao, C. H. Tsai, B. J. Little, Corros. Sci. 36 (1994) 2063–2095.

[7] R. J. K. Wood, S. A. Fry, J. Fluids. Eng. 112 (1990) 218–224.

[8] C. Deslouis, B. Tribollet, G. Mengoli, M. Musiani, J. Appl. Electrochem. 18 (1988) 374–383.

[9] H. P. Lee, K. Nobe, J. Electrochem. Soc. 133 (1986) 2035–2043.

[10] W. H. Smyrl, J. Electrochem. Soc. 132 (1985) 1555–1562.

[11] G. E. P. Box, W. G. Hunter, J. S. Hunter, Statistics for Experimenters: An Introduction to Design, Data Analysis and Model Building; John Wiley and Sons, New York (1978).

[12] D. D. Stephan, J. Werner, R. P. Yeater, Essential regression and experimental design for chemist and engineers, MS Excel add in software package (1998–2001). Available online: http://www.jowerner.homepage.t-online.de/ERPref.html (last visit on 20.11.2012). .

[13] I. Bulacov, J. Jirkovsky, M. Muller, R. B. Heimann, Surf. Coat. Tech. 2006, 201, 255–264.

[14] A. M. Alfantazi, T. M. Ahmed, D. Tromans, Mater. Design 30 (2009) 2425–2430.

[15] F. Arjmand, A. Adriaens, J. Solid State Electrochem. 16 (2012) 535–543.

English conclusions

Electrochemical methods have proven their ability in solid–state surface analysis and corrosion research. These techniques are usually simple, cheap and fast and provide at the same time large amount of information through only a limited number of experiments.

Recently developed electrochemical techniques allow researchers to miniaturize the measurement area and to discover the properties of localized corrosion.

Due to the large measured current density and the high limiting current, micro scale techniques provide high–resolution electrochemical responses. Current densities in the range from a few femto to pico $A.cm^{-2}$ to hundreds of $A.cm^{-2}$ can be measured.

This work has focused on the corrosion investigation of two grades of stainless steel (304L and 316L) and pure copper in the presence of chloride ions using one of the recently developed microelectrochemical techniques called: “microcapillary electrochemical droplet cell” and conventional large scale disc electrodes.

Chapter 1 of this dissertation describes various applications for microcapillary cells in corrosion research and solid state surface characterization as well as some advantages and technical limitations.

In the second chapter, the history, applications and also the corrosion mechanisms of stainless steel and copper in aqueous environments, and especially in sodium chloride solutions, have been discussed. This chapter also contains a short theoretical discussion of the use of electrochemical techniques such as voltammetric polarization and electrochemical impedance spectroscopy.

In the first experimental part (Chapter 3) we have investigated the effect of miniaturizing the measured surface of 304L stainless steel on the obtained voltammetric response using a homemade microcapillary setup during the voltammetric measurements. This comparison has revealed that microcapillary techniques provide different corrosion cells compared to the conventional disc electrodes and therefore, the electrochemical data measured by these two cells may contain serious differences. In the case of microcapillary technique used in this work, it was found that the small surface area under the tip of the microcapillary is strongly under effect of the surrounding area of the microcapillary tip. We have observed that oxygen, which is known as the dominant factor in the cathodic partial reaction during the corrosion process of steel, can penetrate from the surrounding area of the microcapillary through the silicone gasket. Therefore, the oxygen concentration reaches even higher values and the corrosion of steel occurs with greater intensity

under the microcapillary tip than it does for a large scale disc electrode. Given these results, it is recommended to use the microcapillary technique under controlled (aerated) environments.

Chapter 4 has shown the effect of prior cathodic polarization on the corrosion behavior of stainless steel under different conditions such as static macro and micro scale levels and also dynamic macro scale systems, under two different flow regimes. The results show that fluid flow has a key role in the corrosion behavior of the cathodically polarized steel. In the macro scale part, the dynamic conditions were constructed using a homemade flow cell with a vortex flow regime and a rotating disc electrode with vertical stream lines. The results revealed that the applied flow regime during the cathodic polarization process has a direct effect on the anodic polarization behavior of steel. Under static conditions, more negative cathodic potentials shift the corrosion potential (E_{corr}) of steel towards more positive potentials after cathodically polarizing the steel and simultaneously increase the cathodic current density. Under flow conditions, however, it was observed that depending on the structure of the applied fluid flow the rate of the dissolved oxygen reduction can increase or decrease with greater cathodic polarization and therefor, shift the corrosion potential of steel towards more positive or more negative potentials respectively. Reducing the cathodic current density and shifting the corrosion potential of steel after cathodic polarization towards less noble potentials was observed when a homemade flow cell was used. Opposite results were obtained when the cathodic polarization was applied under static conditions or under the flow regime constructed by a rotating disc electrode. Electrochemical impedance spectroscopy of the polarized samples under both static and flow conditions with two different flow regimes revealed cathodically polarized steel to have lower corrosion resistance under flow conditions, especially for high velocities.

On a static micro scale it was found that, in contrast to macro scale systems, the prior cathodic polarization of steel decreases the corrosion potential due to the decrease in the rate of oxygen reduction process. A modified microcapillary setup also was used in this work and the same series of the measurements was performed under the aerated conditions. Similar to Chapter 3, here also removal of the oxygen from the surrounding area of the tip reduced the total current density and improved the reproducibility of the measurements.

Chapter 5 is a combination of the electrochemical corrosion study of pure copper on micro and macro scale levels with a chemometrics strategy which has been used for experimental design. In this chapter the effects of pH and chloride concentration on the electrochemical corrosion of copper in aqueous NaCl media have been studied at

the micro scale using a microcapillary droplet cell and at the macro scale using a conventional large scale disc electrode.

Using an experimental design strategy, electrochemical response surface models of copper versus pH and NaCl concentration have been constructed with a minimum number of experiments required. Results show that the electrochemical behavior of copper under corrosive media shows significant differences between the micro and macro scale experiments. At the micro scale, the pit initiation of copper occurs at more negative potentials for high NaCl concentrations and alkaline pH values. Also, the micro scale potentiostatic measurements indicate higher stabilized passive currents at high NaCl concentrations and low (acidic) pH values. At the macro scale, the pH has shown to have a greater influence on the corrosion potential. The chloride concentration is the most significant factor in the passive current case while at the micro scale the effect of these two factors on the passive current has been found to be the same. These differences in the corrosion performance of copper in micro and macro scale measurements are directly related to different properties of the micro and macro corrosion cells constructed by the two setups.

Reading this dissertation one can get familiar with the application of electrochemical techniques in corrosion research. Especially, microelectrochemical techniques and their key differences with conventional large scale techniques. Furthermore, the performed research which have been discussed throughout this dissertation opens new views and reveals new challenges for corrosion researchers.

As future research one can consider the flow microcapillary setup for the quantification corrosion study of different metals and alloys hyphenated to different chemical analysis techniques. As it has been discussed in the first chapter, the double channel flow microcapillary setup combined with UV–vis and ICP–MS techniques has been introduced by some research groups. However, this is already a future plan in our group to quantify the outlet stream of the flow microcapillary setup by a voltammetric technique using another electrochemical setup.

Nederlandstalige samenvatting

Elektrochemische methoden worden standaard ingezet voor studies aangaande vastestofchemie en corrosie–onderzoek, gezien ze doorgaans grote hoeveelheden aan informatie leveren via een beperkt aantal metingen. Meer recent ontwikkelde elektrochemische methoden laten toe om de grootte van het analysegebied te reduceren en op die manier eigenschappen van het te analyseren oppervlak te kunnen meten op zeer lokale schaal.

Dit werk beoogt een bijdrage te leveren in dit laatste onderzoeksgebied. Meer specifiek spitst het zich toe op het corrosie–onderzoek van twee typen roestvrij staal (304L en 316L) en zuiver koper in de aanwezigheid van chloride–ionen en dit met behulp van een eigen ontwikkelde microcapillaire elektrochemische cel. In wat volgt wordt een overzicht gegeven van de verschillende aspecten die aan bod komen in het werk.

Hoofdstuk 1 beschrijft de verschillende toepassingen voor microcapillaire cellen in corrosie–onderzoek en vastestofchemie en bespreekt daarnaast de voordelen en technische beperkingen van deze techniek.

In hoofdstuk 2 wordt de geschiedenis, de toepassingen en het corrosiemechanisme in aanwezigheid van chloride-ionen van roestvrij staal en koper besproken. Dit hoofdstuk bevat ook een korte theoretische beschrijving van de standaard elektrochemische technieken, waaronder voltammetrie en impedantiespectroscopie.

Hoofdstuk 3 bespreekt de invloed van de reductie van de grootte van het analyseoppervlak van roestvrij staal op de voltammetrische respons besproken. De resultaten worden vergeleken met conventionele voltammetrie.

In hoofdstuk 4 wordt het effect van voorafgaande kathodische polarisatie op het corrosiegedrag van roestvrij staal bestudeerd onder statische en dynamische condities. Voor de dynamische opstellingen worden twee vloeistofbewegingen bestudeerd, met name een lineaire en een andere veroorzaakt door een roterende schijfelektrode. De metingen worden uitgevoerd met de microcapillaire elektrochemische cel en via een conventionele opstelling en worden vergeleken.

Hoofdstuk 5 bestudeert het corrosiegedrag van zuiver koper op micro– en macroschaal, waarbij voor de uitvoering van de metingen gebruik werd gemaakt van een “experimental design” (chemometrische methode).

Het werk wordt afgesloten met conclusies aangaande het werk en een standpunt wat betreft potentieel toekomstig onderzoek in hetzelfde domein.

Publications and activities

List of publications (ISI web of science)

[1] **F. Arjmand**, A. Adriaens, *Microcapillary electrochemical droplet cell: applications in solid state surface analysis*, in preparation.

[2] **F. Arjmand**, A. Adriaens, *Cathodic polarization of 316L stainless steel under static and dynamic conditions*, submitted to Corros. Sci.

[3] W. Liu, **F. Arjmand**, F. Cao, A. Adriaens, *Quantification of metallic copper and nickel in their binary mixtures by voltammetry of immobilized microparticles*, Int. J. Electrochem. Sci., 8 (2013) 2576–2585. (IF = 3.324, Ranking = 9/26).

[4] **F. Arjmand**, A. Adriaens, *Influence of pH and chloride concentration on the corrosion behavior of unalloyed copper in NaCl solution: a comparative study between the micro and macro scales*, Materials 5 (2012) 2439–2464. (IF = 1.679, Ranking = 85/232).

[5] **F. Arjmand**, A. Adriaens, *Microelectrochemical investigation of the effect of cathodic polarisation on the corrosion resistance of 304L stainless steel in a 1 M NaCl solution*, Int. J. Electrochem. Sci. 7 (2012) 8007–8019. (IF = 3.324, Ranking = 9/26).

[6] **F. Arjmand**, A. Adriaens, *Investigation of 304L stainless steel in a NaCl solution using a microcapillary electrochemical droplet cell: Comparison with conventional electrochemical techniques*, Electrochim. Acta 59 (2012) 222–227. (IF = 3.650, Ranking = 5/26).

[7] **F. Arjmand**, A. Adriaens, *Electrochemical quantification of copper based alloys using voltammetry of microparticles: Optimization of the experimental conditions*, J. Solid State Electrochem. 16 (2012) 535–543. (IF = 2.234, Ranking = 14/27).

[8] **F. Arjmand**, A. Adriaens, *Quantification of tin and lead in binary alloys using voltammetry of immobilized microparticles*, Electroanalysis 23(8) (2011) 1941–1947. (IF = 2.721, Ranking = 12/27).

[9] B. Arjmand, S. Aghayan, P. Goodarzi, S. Razavi, A. Jafarian, B. Larijani, K. Khalooghi, E. Charmchi, **F. Arjmand**, *Knowledge and Attitude of Donor Cardholders Toward Organ and Tissue Donation and Transplantation in an Iranian Tissue Bank: A Case–Control Study*, Transp. Proce. 41(7) (2009) 2715–2717. (IF = 0.994, Ranking = 99/167).

[10] M. Bahram, K. Farhadi and **F. Arjmand**, *Voltammetric determination of dopamine in the presence of ascorbic and uric acids using partial least squares*

regression: determination of dopamine in human urine and plasma, Cent. Eur. J. Chem. 7(3) (2009) 524–531. (IF = 1.065, Ranking = 74/140).

[11] M. Bahram, K. Farhadi, A. Afkhami, D. Shokatynia and **F. Arjmand**, *Simultaneous kinetic spectrophotometric determination of Cu(II), Co(II) and Ni(II) using partial least squares (PLS) regression*, Cent. Eur. J. Chem. 7(3) (2009) 375–381. (IF = 1.065, Ranking = 74/140).

[12] B. Arjmand, S.H. Aghayan, P. Goodarzi, M. Farzanehkhah, S.M. Mortazavi, M.H. Niknam, A. Jafarian, **F. Arjmand**, S.J. Far, *Seroprevalence of human T lymphtropic virus (HTLV) among tissue donors in Iranian tissue bank*, Cell and Tissue Banking 10(3) (2009) 247–252.

List of attended conferences

1. **F. Arjmand**, A. Adriaens, *Cathodic polarization of 316L stainless steel under static and dynamic conditions*, 18th meeting of the Portuguese electrochemical society, 25–27 March 2013. Porto, Portugal.
2. **F. Arjmand**, A. Adriaens, *Influence of pH and chloride concentration on the corrosion behavior of unalloyed copper in NaCl solution: a comparative study between micro and macro systems*, 53rd Corrosion Science Symposium, 6–7 September 2012. National Physical Laboratory, Teddington, UK.
3. **F. Arjmand**, A. Adriaens, *Investigation of the influence of pH and chloride concentration on the pit initiation of unalloyed copper in a NaCl solution using a microcapillary electrochemical droplet cell*, Chemistry Conference for Young Scientists (ChemCYS), 1–2 March 2012, Blankenberge, Belgium.
4. **F. Arjmand**, A. Adriaens, *Microelectrochemical synthesis of 304L stainless steel nanoparticles and their effect on the corrosion resistance of this alloy*, Chemistry Conference for Young Scientists (ChemCYS), 1–2 March 2012, Blankenberge, Belgium.
5. **F. Arjmand**, A. Adriaens, *Investigation of 304L stainless steel in a NaCl solution using a microcapillary electrochemical droplet cell: Comparison with conventional electrochemical techniques*, Chemistry Conference for Young Scientists (ChemCYS), 1–2 March 2012, Blankenberge, Belgium.